

Stretchable Magnetoelectronics

von der Fakultät für Naturwissenschaften der Technischen Universität Chemnitz
genehmigte Dissertation zur Erlangung des akademischen Grades

doctor rerum naturalium

(Dr. rer. nat.)

Vorgelegt von Dipl.-Phys. Michael Melzer

geboren am 08. Mai 1983 in Berlin

eingereicht am 05. Juni. 2015

Gutachter: Prof. Dr. Oliver G. Schmidt

Prof. Dr. Siegfried Bauer

Tag der Verteidigung: 19. November 2015



Stretchable Magnetoelectronics

Chemnitz University of Technology, 2015

Faculty of Natural Sciences

Dissertation on 124 pages

Keywords: stretchable electronics, magnetoelectronics, giant magnetoresistance, magnetic sensorics, soft matter, thin films, magnetic materials, magnetic nanomembranes, strained nanomembranes, electronic skin

Abstract:

In this work, stretchable magnetic sensorics is successfully established by combining metallic thin films revealing a giant magnetoresistance effect with elastomeric materials. Stretchability of the magnetic nanomembranes is achieved by specific morphologic features (*e.g.* wrinkles), which accommodate the applied tensile deformation while maintaining the electrical and magnetic integrity of the sensor device. The entire development, from the demonstration of the world-wide first elastically stretchable magnetic sensor to the realization of a technology platform for robust, ready-to-use elastic magnetoelectronics with fully strain invariant properties, is described. The prepared soft giant magnetoresistive devices exhibit the same sensing performance as on conventional rigid supports, but can be stretched uniaxially or biaxially reaching strains of up to 270% and endure over 1,000 stretching cycles without fatigue. The comprehensive magnetolectrical characterization upon tensile deformation is correlated with in-depth structural investigations of the sensor morphology transitions during stretching.

With their unique mechanical properties, the elastic magnetoresistive sensor elements readily conform to ubiquitous objects of arbitrary shapes including the human skin. This feature leads electronic skin systems beyond imitating the characteristics of its natural archetype and extends their cognition to static and dynamic magnetic fields that by no means can be perceived by human beings naturally. Various application fields of stretchable magnetoelectronics are proposed and realized throughout this work. The developed sensor platform can equip soft electronic systems with navigation, orientation, motion tracking and touchless control capabilities. A variety of novel technologies, like smart textiles, soft robotics and actuators, active medical implants and soft consumer electronics will benefit from these new magnetic functionalities.

Outline

List of abbreviations.....	7
1. INTRODUCTION	
1.1 Motivation and scope of this work	8
1.1.1 A brief review on stretchable electronics	8
1.1.2 Stretchable magnetic sensorics	10
1.2 Technological approach	11
1.3 State-of-the-art	12
2. THEORETICAL BACKGROUND	
2.1 Magnetic coupling phenomena in layered structures	14
2.1.1 Magnetic interlayer exchange coupling	14
2.1.2 Exchange bias	15
2.1.3 Orange peel coupling	16
2.2 Giant magnetoresistance	17
2.2.1 Electronic transport through ferromagnets	17
2.2.2 The GMR effect	19
2.2.3 GMR multilayers	20
2.2.4 Spin valves	21
2.3 Theory of elasticity	22
2.3.1 Elastomeric materials	22
2.3.2 Stress and strain	23
2.3.3 Rubber elasticity	25
2.3.4 The Poisson effect	26
2.3.5 Viscoelasticity	27
2.3.6 Bending strain in a stiff film on a flexible support	27
2.4 Approaches to stretchable electronic systems	28
2.4.1 Microcrack formation	28
2.4.2 Meanders and compliant patterns	29
2.4.3 Surface wrinkling	30
2.4.4 Rigid islands	32
3. METHODS & MATERIALS	
3.1 Sample fabrication	34
3.1.1 Polydimethylsiloxane (PDMS)	34
3.1.2 PDMS film preparation	35
3.1.3 Lithographic structuring on the PDMS surface.	36
3.1.4 Magnetic thin film deposition	38
3.1.5 GMR layer stacks	40
3.1.6 Mechanically induced pre-strain	43
3.1.7 Methods and materials for the direct transfer of GMR sensors	45
3.1.8 Materials used for imperceptible GMR sensors	47
3.2 Characterization	48
3.2.1 GMR characterization setup with <i>in situ</i> stretching capability	48
3.2.2 Sample mounting	50

3.2.3 Electrical contacting of stretchable sensor devices	51
3.2.4 Customized demonstrator electronics	52
3.2.5 Microscopic investigation techniques	53
4. RESULTS & DISCUSSION	
4.1 GMR multilayer structures on PDMS	54
4.1.1 Pre-characterization	54
4.1.2 Thermally induced wrinkling	55
4.1.3 Self-healing effect	57
4.1.4 Demonstrator: Magnetic detection on a curved surface	60
4.1.5 Sensitivity enhancement	61
4.1.6 GMR sensors in circumferential geometry	64
4.1.7 Stretchability test	67
4.2 Stretchable spin valves	69
4.2.1 Random wrinkles and periodic fracture	70
4.2.2 GMR characterization	73
4.2.3 Stretching of spin valves	74
4.2.4 Microcrack formation mechanism	76
4.3 Direct transfer printing of GMR sensorics	81
4.3.1 The direct transfer printing process	82
4.3.2 Direct transfer of GMR microsensor arrays	84
4.3.3 Direct transfer of compliant meander shaped GMR sensors	86
4.4 Imperceptible magnetoelectronics	89
4.4.1 GMR multilayers on ultra-thin PET membranes	89
4.4.2 Imperceptible GMR sensor skin	92
4.4.3 Demonstrator: Fingertip magnetic proximity sensor	93
4.4.4 Ultra-stretchable GMR sensors	94
4.4.5 Biaxial stretchability	99
4.4.6 Demonstrator: Dynamic detection of diaphragm inflation	101
5. CONCLUSIONS & OUTLOOK	
5.1 Achievements	102
5.2 Outlook	104
5.2.1 Further development steps	104
5.2.2 Prospective applications.	105
5.3 Technological impact: flexible Bi Hall sensorics	106
5.3.1 Application potential	106
5.3.2 Thin and flexible Hall probes	107
5.3.3 Continuative works and improvements	108
5.4 Activities on technology transfer and public relations	108
Appendix	
References.....	110
Selbständigkeitserklärung.....	119
Acknowledgements.....	120
Curriculum Vitae.....	121
Scientific publications, contributions, patents, grants & prizes.....	122

List of abbreviations

ADC	analog-to-digital converter	LED	light emitting diode
AFCM	antiferromagnetic coupling maximum	MACS	magnetic-activated cell sorting
AFM	atomic force microscopy	MCU	microcontroller unit
AMB	active magnetic bearing	MOKE	magneto-optic Kerr effect (characterization)
BMBF	German Federal Ministry of Education and Research	NM	non-magnet
CIP	current-in-plane	NMP	neutral mechanical plane
CMOS	complementary metal-oxide-semiconductor (technology)	PAA	poly(acrylic acid)
[Co/Cu]₅₀^{1st}	Co/Cu GMR multilayer in the 1 st AFCM	PC	personal computer
[Co/Cu]₃₀^{2nd}	Co/Cu GMR multilayer in the 2 nd AFCM	PDMS	poly(dimethylsiloxane)
CPP	current-perpendicular-to-plane	PEEK	poly(ether ether ketone)
DC	direct current	PET	poly(ethylene terephthalate)
DEA	dielectric elastomer actuator	PU	Polyurethane
DFG	German Research Foundation	Py	permalloy (Ni ₈₁ Fe ₁₉)
DI	deionized (water)	[Py/Cu]₅₀^{1st}	Py/Cu GMR multilayer in the 1 st AFCM
DoS	density of states	[Py/Cu]₃₀^{2nd}	Py/Cu GMR multilayer in the 2 nd AFCM
EB	exchange bias	RF	radio frequency
EDTA	ethylenediaminetetraacetic acid	RKKY	Ruderman-Kittel-Kasuya-Yosida
ERC	European Research Council	SEM	scanning electron microscopy
FEM	finite element method	SiOx	oxidized silicon wafer substrate
FIB	focused ion beam	SV	spin valve
FM	ferromagnet	TU	University of Technology (Dresden)
FPC	flexible printed circuit	TMR	tunnel magnetoresistance
GMR	giant magnetoresistance	USB	universal serial bus
IFW	Institute for Solid State and Materials Research (Dresden)	VHB	VHB™ 4905 (very high bond) adhesive tape from 3M™

1. INTRODUCTION

1.1 Motivation and scope of this work

Electronics of tomorrow will be compliant and will form a seamless link between soft or even living materials and the digital world. For this purpose, electronic systems have to reversibly accommodate tensile strains far beyond the intrinsic ductility of the active electronic materials they are made of. The development of *stretchable electronics*¹⁻³ is at the forefront of multidisciplinary research efforts, bridging physics, engineering and materials science. Magnetic functionalities can provide features to this novel electronics that are not available by other means. While *flexible* magnetoresistive sensorics has been demonstrated already^{4,5}, the thesis in hand is focused on the development of *stretchable* forms of magnetoelectronics^{6,7}, which was not considered, yet. Before the benefits and target properties of soft magnetoelectronics are introduced, a brief review on general stretchable electronics will be given.

1.1.1 A brief review on stretchable electronics

Succeeding the development of flexible electronic systems⁸, stretchable electronics⁹⁻¹¹ became one of the most vital technological research fields of the latest years, aiming to revolutionize common electronic systems towards being arbitrarily re-shapeable on demand after their fabrication, particularly on large areas. In this respect, stretchable devices are able to accommodate tensile strains much larger than 10%, without sacrificing their performance. Organic electronic materials have been extensively used to create stretchable systems with various functionalities¹²⁻¹⁴ even featuring active matrix addressing capabilities^{15,16}. Compliant designs of inorganic semiconductor^{9,17,18} and metal-based¹⁹⁻²² electronics, however, combine the advantages of being soft with the high speed and low power consumption capabilities of conventional semiconductor-based electronics²³.

Pioneering work in this respect was conducted by S. Wagner, S.P. Lacour *et al.* with the discovery that wrinkled metal thin films²⁴ can be stretched by several tens of percent without losing their conductive properties²⁵⁻²⁸. Since then, many works concentrated on the design and fabrication of highly stretchable metallic interconnects^{10,21,29-32} to wire rigid functional elements forming compliant electronic mesh circuits^{15,20,33}. The demonstration by the group of J.A. Rogers, that also silicon nanomembranes³⁴ and other layered materials can be wrinkled to withstand large tensile deformations^{35,36}, rendered functional electronic components and entire logic circuits to become stretchable⁹. A large variety of compliant organic and inorganic electronic elements with various functions have been realized in the last years, which are summarized in **figure 1.1**. These devices include light emitting diodes (LEDs)^{37,38}, heaters¹⁶, actuators³⁹ and supercapacitors⁴⁰. Stretchable sensoric devices can detect mechanical^{22,41,42}, optical⁴³, thermal^{44,45} or bioelectric^{46,47} stimuli. The power supply of prospective soft electronic systems may be assured by incorporated stretchable solar cells^{13,48}, energy harvesters^{49,50} or batteries^{51,52}. Wireless powering and data transfer using stretchable

antenna designs have also been shown^{19,53}. Recent developments aim to add further useful features beyond stretchability: Transient electronics⁵⁴ is able to completely dissolve upon fulfilling its task after a defined period of time and imperceptible forms of electronic systems^{16,45,55} are haptically not perceived if worn on skin.

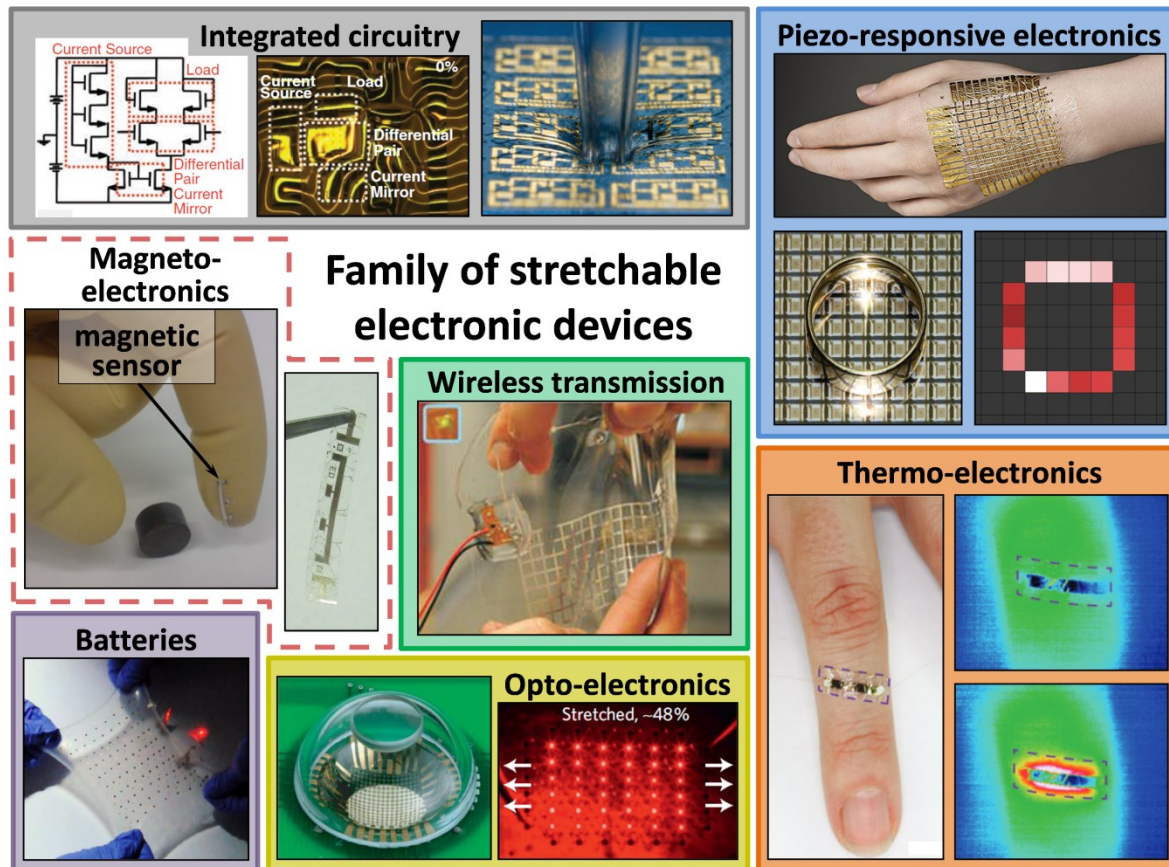


Figure 1.1 | Overview of available functionalities in stretchable electronic devices: Various capabilities have been demonstrated already. Stretchable magnetoelectronics, which is introduced in this work, adds magnetic functionalities and is also included as a new member in this family. Figure compiled from [1,6,9,16,18,19,43,52].

Stretchable electronics is envisioned to enable exciting applications (**figure 1.2**) that lie beyond the reach of current technologies². One of the main developments in this respect is the emerging field of *electronic skins* (e-skins)^{26,53,56}, which are conformably situated on biological tissue readily following all its natural motions and distortions. Ideally, e-skins do not restrict the natural mobility and function of the tissue they are attached to and are even imperceptible by the recipient^{16,45}. The intimate contact with the epidermal surface throughout its complex shape is of great advantage for sensorics in particular^{53,57,58}. Inspired by nature's archetype, electronic skins are already able to perceive temperature changes^{44,59}, mimic the sensation of touch^{41,60,61}, monitor physiological conditions^{53,58,62} and even release drug doses on demand for therapy⁶³. Approaches that enable self-healing⁶⁴ will lead to durable and multifunctional artificial skin. In addition to being wearable, e-skins can also be operated *in vivo* as bio-integrated electronics^{65,66} enabling highly functional and compliant diagnostic or therapeutic implants⁴⁷ as well as advanced surgical tools⁶⁷.

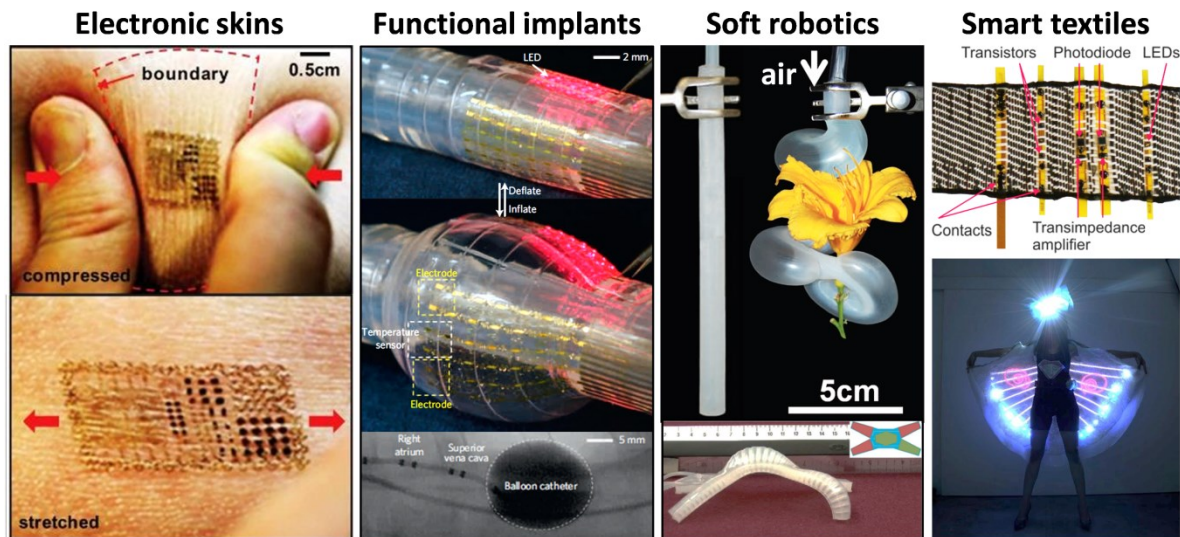


Figure 1.2 | Application fields of stretchable electronics: Overview of applications for soft electronics with prospective potential for stretchable magnetic sensorics. Figure compiled from [47,53,68-70].

Another novel and highly innovative field of prospective applications for stretchable electronics is *soft robotics*^{69,71} and particularly *elastomeric actuators*^{39,72}. This novel actuator technology allows for a lightweight⁷³, indestructible⁷⁴ and adaptive⁶⁸ design of robotics that may even feature cloaking capabilities⁷⁵. Their large actuation strains^{39,76} and rapid motion^{77,78} call for an extraordinary compliant form of electronics to be integrated into this kind of electromechanical transducers. Magnetic features have recently been introduced into soft robots to enable modular design concepts for an adaptive assembly of specific functionalities on demand⁷⁹. Stretchability of functional electronic elements is also expected to have high potential for wearable devices^{50,61} and smart textiles⁸⁰.

1.1.2 Stretchable magnetic sensorics

Despite the manifold functionalities that are available for stretchable electronic systems, magnetic aspects have not been addressed so far. The aim of the present work is to add a new member to the family of stretchable electronic devices - the *stretchable magnetic field sensor* (figure 1.1). The development of a technology platform for the preparation of magnetic sensing elements that are elastic and ideally do not alter either electrical properties or magnetoelectric response upon severe and repeated tensile deformations (*strain invariance*) is in the main focus of this work. Further features, that are highly beneficial for their application potential and should enable a rapid innovation process, are to be taken into account during the technological development: (i) The sensing capabilities of the proposed stretchable elements should cover a broad range of magnetic field strengths in order to address prospective application areas ranging from biomedical sensorics to soft motion and displacement gauges. (ii) The preparation processes has to be compatible with current fabrication strategies of already available stretchable electronic platforms^{1,2}. This is also intended to provide a solid technological base for the successive steps towards commercially suitable devices, especially by the incorporation of compliant electronic circuits⁹, e.g. for sensor signal processing⁵⁵, multiplexing¹⁶ or wireless powering and readout^{52,53} or the realization of other soft spintronic components^{81,82}.

The integration of magnetic sensorics into existing stretchable electronics platforms paves the way to realize smart and soft devices with the ability to sense and respond to a magnetic field. With a broad range sensitivity and compliant design of stretchable magnetoelectronics, a variety of application fields could be envisioned, as it would equip these novel soft systems with navigation, orientation or tracking as well as touchless control and triggering capabilities. Stretchable magnetic sensors can, for instance, lead the e-skin concept beyond imitating the features of human physiology and extend its cognition to magnetic fields, which otherwise are not accessible by humans naturally. This enables a *sixth sense of magnetoception*^{83,84} for artificial skins systems.

Since the acquisition of motion and displacement has developed to be the main duty of magnetic sensorics in conventional machinery, a stretchable counterpart can adopt these functions into soft systems. Hence, as electronic skin, magnetic sensing elements would be ideally suited for touchless human-machine interaction, by means of accurate motion tracking in an artificial magnetic environment⁷. In the field of bio-integrated electronics and functional implants, magnetic sensing capabilities could include real time monitoring of muscles, joints or valves of the heart to diagnose early stages of dysfunctions. The displacement sensing capabilities can also play a key role for the recording and accurate control of actuation in soft robotic systems. As for their rigid counterparts, keeping track of the current position of all its movable parts is an essential requirement for highly functional robots with multi-tasking abilities. This is even more vital to soft robots, as the displacement of actuating components is strongly dependent on the mechanical load on these parts. Control strategies relying on the feedback from magnetic motion tracking sensorics can provide a comprehensive, highly integrative and cost effective solution to this issue compared to *e.g.* optical approaches.

Foreseeable applications of highly sensitive and re-shapeable magnetoelectronics also include the in-flow detection of magnetic particles or magnetically labeled analytes^{85,86}, in advanced fluidics⁸⁷ and lab-on-a-chip⁸⁸ platforms, which may boost the health monitoring, point-of-care diagnostics and environmental sensing capabilities of these systems. Furthermore, stretchable forms of consumer electronics⁸⁹ and smart textiles⁸⁰ will benefit from magnetic functionalities offered by compliant magnetoelectronics.

1.2 Technological approach

Depending on the desired properties (*i.e.* sensitivity, magnetic field range, sensitive direction, temperature behavior *etc.*), there are several technologies available for the realization of magnetic sensing devices⁹⁰. These include for example Hall sensors⁹¹, anisotropic magnetoresistance elements⁹², magnetic tunnel junctions⁹³ and fluxgate magnetometers⁹⁴. Magnetic thin films revealing a *giant magnetoresistance* (GMR) effect are able to vary their electrical resistance by several tens of percent upon application of an external magnetic field⁹⁵. The utilization of GMR-based sensorics, for example in magnetic read heads⁹⁶ boosted the capacity and performance of magnetic data storage systems. The

discovery of the GMR effect was honored with the 2007 Nobel Prize in Physics to Albert Fert and Peter Grünberg⁹⁷. Such giant magnetoresistive thin film structures are chosen as the magnetic sensorics technology suitable for the development of stretchable magnetoelectronics in this work. A description of the physical background of the GMR effect in layered magnetic structures and the fundamental interactions it is based on are given in the subchapters 2.1 and 2.2.

Currently, GMR sensor devices are fabricated on rigid inorganic substrates like oxidized silicon (SiOx) wafers or glass. Although there is some activity toward straining of GMR structures grown on this kind of substrates by means of bending to study their magnetoelastic behavior^{98,99}, the maximal achievable deformation of a few % is far too low for any applications within the concept of stretchable electronics. In order to be able to elastically stretch GMR sensor elements to much higher levels of deformation, the magnetic nanomembranes should be situated on an elastomeric substrate. The smart combination of thin metal films and soft polymeric membranes, as proposed in this work, allows creating the technology platform for stretchable GMR based sensorics. The accommodation of high strains in thin films of intrinsically stiff materials is facilitated by morphologic features¹⁰⁰, e.g. wrinkles¹⁰¹, which are to be introduced into the system. They are able to transfer large tensile deformations of the substrate into minimal strains in the functional film^{25,102}. A review of technological strategies that lead to high stretchabilities of thin film electronic structures is given in subchapter 2.4.

1.3 State-of-the-art

The deposition of GMR films, including multilayers¹⁰³ and later also more advanced exchange biased sandwich stacks¹⁰⁴ onto *flexible* substrates was first demonstrated in 1992 by S.S.P. Parkin *et al.*. The motivation of this pioneering work at the IBM research center was mainly driven by the need for lightweight magnetoresistive read heads with good insulating barriers, which was the main driving force for the development of GMR-based sensorics in the early 90's. The magnetoresistive performance of extended GMR layers deposited on flexible foils, including polyimide, polyethylene terephthalate, polyetherimide and regular transparency, was found to be comparable to stacks on rigid SiOx wafers. However, the impact of mechanical deformations like bending on the GMR performance of these *flexible* sensors was not investigated.

Deformations of GMR sensoric structures were originally applied on conventional SiOx wafer or glass supports to study effects of inverse magnetostriction on the magnetoelectric characteristics⁹⁸ and eventually use those for highly sensitive strain gauges^{99,105}. Although the supports used in these studies are considered rigid, they allow for a small amount of bending deformation, which is translated to the functional magnetic layers on the outer surface as a tensile deformation (bending strain) of the order of about 0.1%. Later, similar studies were performed using plastic polyimide substrates¹⁰⁶, which allowed for magnetoelectric measurements at tensile strains of up to 0.75% directly applied by stretching¹⁰⁷.

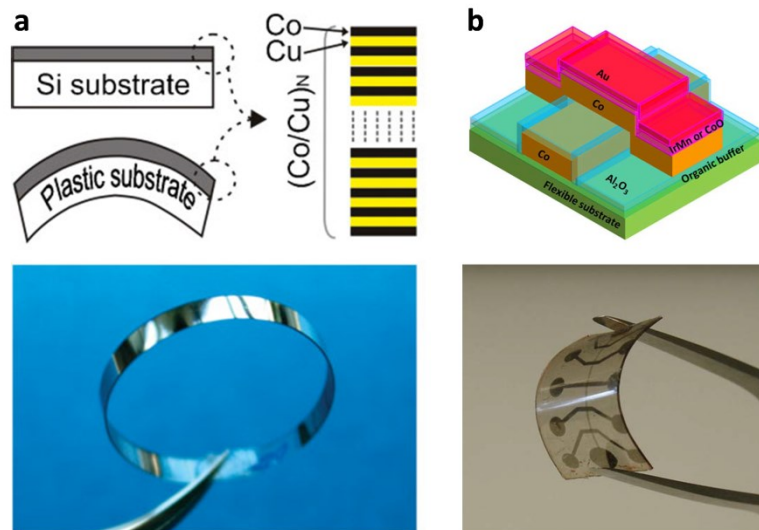


Figure 1.3 | Flexible magnetoelectronics: Magnetic sensoric systems on bendable polymeric foils. **(a)** GMR multilayers and **(b)** magnetic tunnel junctions. Figure adopted from [4,5].

Higher levels of deformation were obtained by Y.F. Chen *et al.*, who deposited extended GMR films on buffer coated polyester transparency, as shown in **figure 1.3a**⁴. No performance degradation was observed in the magnetoresistive elements after 1,000 bending cycles to a radius of about 22 mm. Furthermore, tensile testing of the flat GMR film up to above 2% strain revealed a mechanism for a mechanical fine tuning of the magnetoelectric properties. However, since the deposition was done on a flexible polymer sheet, rather than on an elastic rubber substrate, these tensile deformations were of a strongly plastic nature and did not allow for repeated stretching.

Even high-performance magnetic tunnel junctions were successfully prepared on flexible polymeric supports by C. Barraud *et al.*⁵, which is highly challenging due to the necessary incorporation of smooth tunnel barriers in the low nanometer thickness regime into the device structure (figure 1.3b). Although being slightly differed from the reference devices on rigid SiOx wafer, the magnetoelectric response in the flat state was unaffected by bending the sensors to a radius of 15 mm and back.

The available literature shows that magnetoresistive sensorics on flexible foils was established by 2010, revealing operation down to bending radii in the low centimeter range. Previous studies of magnetic thin films on elastomeric substrates are rarely found^{108,109}, and they neither include magnetoelectric structures nor any investigation of macroscopic deformation. However, the mentioned works created a solid background for this PhD thesis, where the world-wide first *elastically stretchable* GMR sensorics, that is able to accommodate also large tensile deformations, is demonstrated.

2. THEORETICAL BACKGROUND

This chapter is dedicated to a brief introduction of the most relevant physical phenomena and technological concepts that form the fundamental basis of the present work. As the development of stretchable magnetoelectronics combines aspects of magnetism and magnetic materials with soft matter physics, both fields will be covered. This includes a general explanation of the giant magnetoresistance effect, together with a review of the fundamental physical interactions it originates from. The different types of GMR systems that are exploited throughout this work are defined as well. Subsequently, an introduction to rubber materials and the theoretical basics of elasticity are given. The chapter closes with the presentation of different established concepts for the achievement of stretchable architectures of functional electronic components or systems based on *thin films*.

2.1 Magnetic coupling phenomena in layered structures

The giant magnetoresistance was first observed in magnetic structures fabricated by thin-film technology¹¹⁰. Magnetic shape anisotropy¹¹¹ causes the magnetic moments of a ferromagnetic body (e.g. Fe or Co), in the absence of external magnetic fields, to align preferentially along its longest axis. Hence, in an extended magnetic layer, the moments rest in an in-plane direction, if contributions from other magnetic anisotropies are negligible. However, several magnetic coupling phenomena, which are observed if thin magnetic layers are brought into close proximity to each other, strongly influence their equilibrium magnetic configuration. These couplings play a key role for the occurrence of the GMR effect in metallic thin film architectures and their understanding and control offers a convenient way to influence and tune the magnetoelectric response characteristics of GMR based sensor devices.

2.1.1 Magnetic interlayer exchange coupling

The *interlayer exchange coupling* occurs if two ferromagnetic (FM) layers are separated by a thin nonmagnetic (NM) spacer¹¹². It forces the two in-plane magnetizations to adopt a certain orientation relative to each other. This coupling is described in the frame of the *Ruderman-Kittel-Kasuya-Yosida*- (RKKY-) formalism¹¹³, which accounts for an interaction between the nuclear magnetic moments and inner electron spins of two individual metal atoms mediated by the conduction electrons. This specific interaction exhibits a damped oscillatory behavior over the distance d of the considered atoms, as indicated in **figure 2.1**. The general form of the coupling strength J_{RKKY} is typically described as¹¹⁴:

$$J_{\text{RKKY}}(d) \sim \frac{\cos(2k_{\text{F}} \cdot d)}{d^3} \quad (2.1)$$

where k_{F} is the radius of the conduction electron Fermi surface. Therefore, in an FM/NM/FM sandwich-structure, the magnitude and sign of the coupling strength between the FM layers is strongly dependent on the thickness of the NM spacer layer⁹⁵. For very small separations, there is a large

negative coupling (point a in figure 2.1), which results in an antiparallel alignment of the respective magnetizations. Due to the analogy to the antiparallel spin order in antiferromagnetic materials, this situation is referred to as the *first antiferromagnetic coupling maximum* (AFCM). As the separation increases, the coupling becomes positive (point b), *i.e.* the layers will be magnetized parallel to each other. For further increase of the spacing, the interaction drives the sandwich into a *second antiferromagnetic coupling maximum* (point d), with exhibits a smaller coupling strength than in the first one, and so on. Since the coupling sign and magnitude of the interlayer exchange coupling rapidly changes over very short distances, the film quality and individual layer thicknesses have to be well-defined in GMR multilayer films.

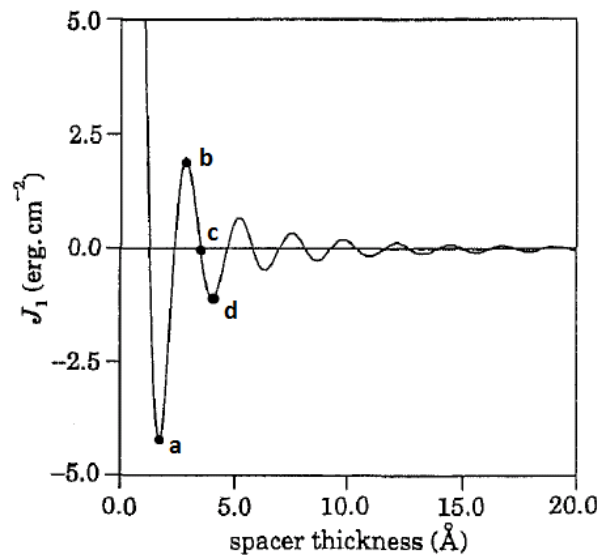


Figure 2.1 | RKKY interaction: Coupling strength J_1 in dependence of the interatomic distance. Figure adopted from [115].

2.1.2 Exchange bias

Another relevant coupling phenomenon is the *exchange bias interaction* (EB)¹¹⁶, which is particularly important for spin valve devices, which are introduced in section 2.2.4. This type of interaction occurs at the interface between a ferromagnetic and an antiferromagnetic layer. The effect is based on the aforementioned exchange coupling between the two, which fixes the interfacial spins of the ferromagnet due to a strong interaction to the adjacent antiferromagnet. The microscopic origin of this interaction can be described relying on different models, which are adapted to specific material classes¹¹⁷⁻¹¹⁹. For instance, the Mauri model describes the magnetization reversal in an exchange biased ferromagnetic layer that requires additional energy for creating a domain wall in the hard antiferromagnetic film¹¹⁸. Therefore, the entire ferromagnetic film gets effectively 'pinned' along a certain direction, which results in a shift of its magnetization curve, as indicated by exemplary magneto-optic Kerr effect (MOKE) characterizations in **figure 2.2**. The main feature of exchange bias is that it influences the magnetization not only along a certain axis, but in a specific direction; hence, it resembles itself as a unidirectional anisotropy.

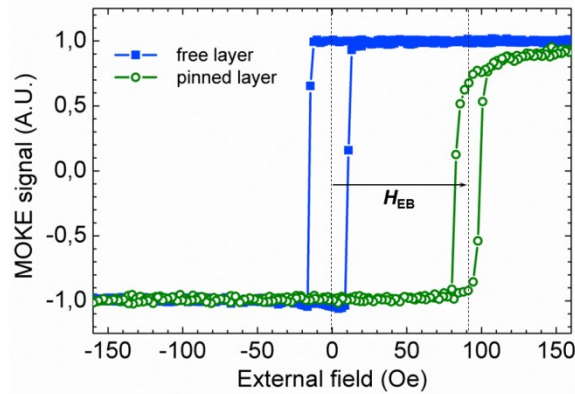


Figure 2.2 | Exchange bias: Hysteresis loop measurements of a free layer of $\text{Co}_{80}\text{Fe}_{20}$ (blue) compared with one that is exchange biased by IrMn in the applied field direction (green), resulting in an exchange bias field H_{EB} of 91 Oe. Data measured by Tobias Kosub (IFW Dresden).

2.1.3 Orange peel coupling

For the occurrence of the GMR effect in layered magnetic structures, usually a strong antiferromagnetic coupling between the FM layers is beneficial. However, there are other coupling mechanisms between these layers that always result in a parallel alignment of magnetizations and should therefore be avoided. The so-called *orange-peel coupling* can occur in a FM/NM/FM thin film sandwich if its interfaces exhibit a certain roughness.

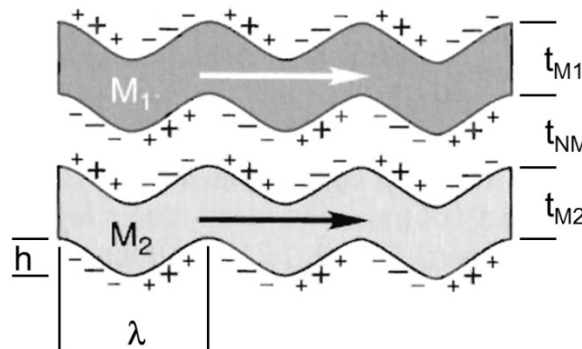


Figure 2.3 | Orange-peel coupling: Two separated ferromagnetic layers of Magnetization M_1 and M_2 with conformal roughness. The roughness amplitude h (not drawn to scale), the topographical wavelength of the correlated interfaces λ and the thickness of the NM spacer layer t_{NM} strongly influence the coupling strength. Figure adopted from [115].

As shown in **figure 2.3**, the in-plane magnetization develops components perpendicular to the local interface orientation, thereby generating magnetic dipoles at the protrusions. If the interfaces of both magnetic layers are topographically correlated, the resultant locally confined stray fields evolving outside and through the spacer layer finally drive them into a ferromagnetic (parallel) configuration¹²⁰. Hence, this effect occurs by magnetostatic interaction between FM layers with

conformal interface roughness. Due to this coupling effect, the surface roughness of the substrate and the quality of the deposited layers play an important role for the fabrication of GMR structures. As a rule of thumb, the substrate should be as smooth as possible in the sub-nanometer range to obtain considerable GMR effect strengths.

2.2 Giant magnetoresistance

In order to understand the occurrence of the GMR effect, besides the magnetic coupling phenomena described above, one has to consider peculiarities in the electronic transport through magnetic materials. After a description of the physical origin of the GMR effect on the model of a simple magnetic sandwich structure, the different types of GMR thin films used in this work are introduced.

2.2.1 Electronic transport through ferromagnets

A directed flow of charge carriers is considered as an electrical current. Since the (magneto-)electrical elements described in this work are metal based, only electrons will be taken into account as charge carriers, here. Usually an electrical current in nonmagnetic metals consists in equal parts of spin-up and spin-down electrons. In general, the electrical resistivity of a material is caused by the scattering of charge carriers, mainly on phonons and lattice defects. These types of scattering are experienced similarly by both species of electrons. However, magnetism strongly influences the electronic transport properties through condensed matter. For ferromagnetic materials the scattering of charge carriers does depend on their spin state. This *spin dependent scattering* can be explained by means of the simplified illustration of the exchange split $3d$ band of a ferromagnetic element, shown in **figure 2.4a**.

The splitting of the band and the resultant unbalanced quantities of up-spins and down-spins, discriminates them into majority and minority electrons, which grants the material its characteristic magnetic moment. The density of states (DoS) at the Fermi energy E_F also differs for both electronic species. Hence, there is a difference in available (unoccupied) states at the Fermi level for spin-up and spin-down electrons. If an electrical current, with an equal number of both species of electrons, is about to enter a ferromagnetic material with a homogeneous magnetization, less states can be occupied by majority electrons compared to minority ones. When spin flipping is neglected, each species of electrons can only occupy a free state in the respective part of the split band, even after a scattering event. Since fewer states are available, that majority electrons can be scattered to in the situation shown in figure 2.4a, the scattering probability is lower for these electrons compared to minority ones. In fact, the electron scattering probability is proportional to the DoS at the Fermi level¹²¹. This means that majority electrons will experience a lower resistivity than minority ones, which makes the electronic transport in a ferromagnet spin dependent.

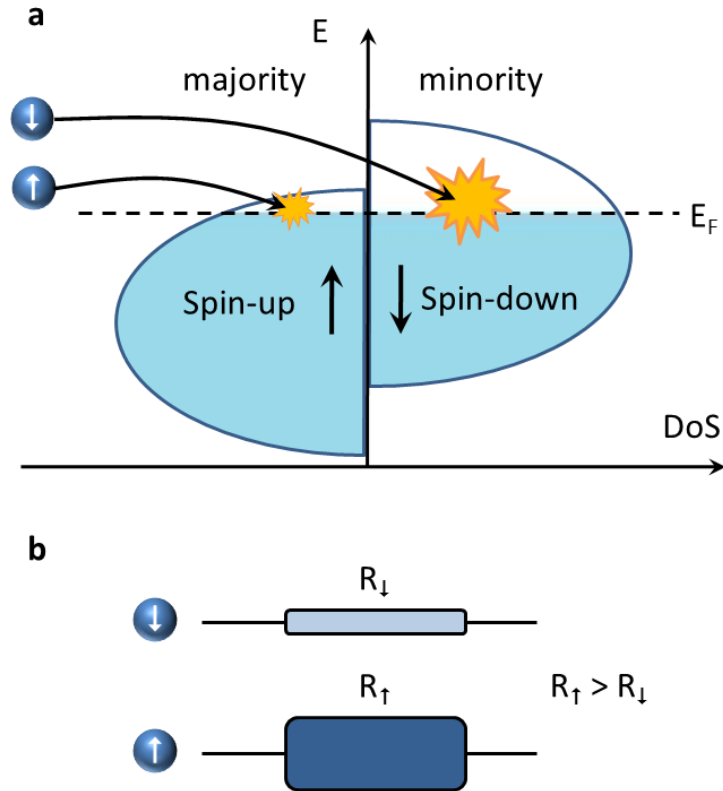


Figure 2.4 | Electronic transport through ferromagnetic matter: (a) Different scattering potential for majority and minority electrons in the exchange split d band due to different amount of unoccupied states at the Fermi-edge (spin dependent scattering). (b) Resulting resistance configuration in the two-current-model.

The described effect can be regarded in a simplified way as a *two-current-model*, which was suggested by N.F. Mott in 1936, by treating the flow of the two electron species as two individual currents¹²¹ (figure 2.4b). This way, for a given piece of ferromagnetic material, there are two different resistances for the spin-up and spin-down currents, respectively. As a result, the current through a ferromagnet becomes *spin polarized* (i.e. it does no longer consist in equal parts of spin-up and spin-down electrons). The degree of spin polarization P is defined by:

$$P = \frac{(n_{\uparrow} - n_{\downarrow})}{(n_{\uparrow} + n_{\downarrow})} \quad (2.2)$$

where n_{\uparrow} and n_{\downarrow} are the number of electrons at the Fermi energy with spin-up and spin-down, respectively. However, it has to be taken into account that the two-current-model relies on strong physical assumptions. As already mentioned, it disregards spin flipping of the conduction electrons, which tends to happen during scattering events, especially with magnons or in systems with a high spin-orbit-coupling. Only in this simplified picture, the two currents can be regarded as independent. Furthermore it assumes a homogeneous magnetization of the entire ferromagnet without the presence of magnetic domains or domain walls.

2.2.2 The GMR effect

Expanding the concept of spin dependent scattering to an FM/NM/FM sandwich structure, the electronic transport properties depend on the magnetic configuration in the FM layers¹¹⁰, as visualized in **figure 2.5a,b**. If we consider the case of antiferromagnetic exchange coupling between the outer FM layers, the spin-up and spin-down electrons exhibit higher numbers of scattering events in different sections of the structure, respectively. One species is subjected to stronger scattering in the first FM layer, the other one in the second FM layer, due to the antiparallel magnetization (figure 2.5a). Regarding this situation in the two-current model, the two electron species experience a different resistance configuration, as illustrated in figure 2.5c. For the non-magnetic spacer, a highly conductive metal is chosen and its regular (*i.e.* spin independent) scattering is not included in this picture.

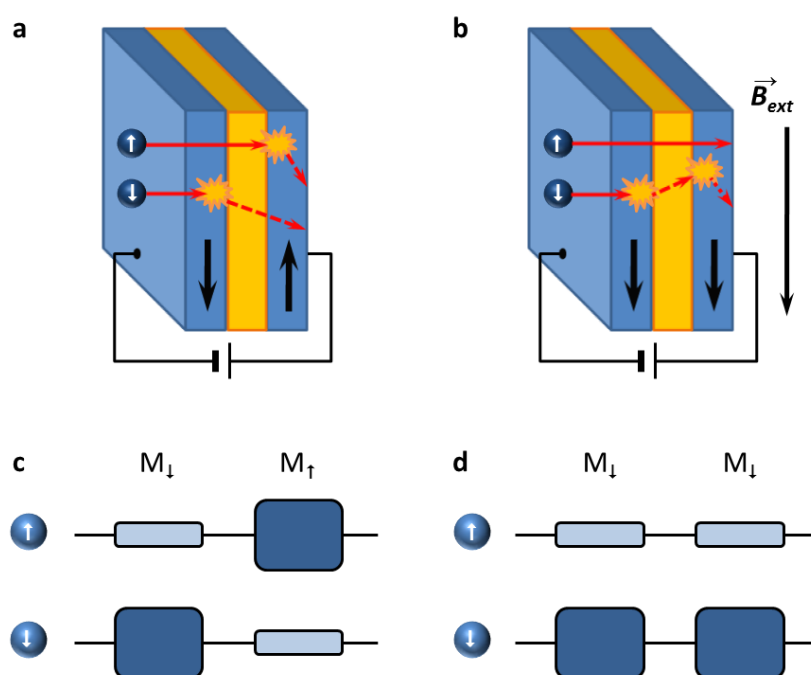


Figure 2.5 | Electronic transport through an FM/NM/FM sandwich structure: Spin dependent scattering events of spin-up and spin-down conduction electrons for antiparallel (**a**) and parallel (**b**) magnetization. (**c,d**) corresponding resistance configuration in the two-current-model. The total resistance of the left case is higher compared to the configuration on the right ($R_{\downarrow\uparrow} > R_{\downarrow\downarrow}$).

With an external magnetic field applied in-plane, the magnetizations can be forced to align parallel, which influences the scattering of both partial currents. As visualized in figure 2.5b, one species is not subjected to spin dependent scattering through the entire sandwich stack, the other one is scattered in both FM layers. The resulting resistance configuration, shown in figure 2.5d, gives a lower net-resistance of the whole layer system compared to the previous case. If the external field is switched off, the antiferromagnetic exchange coupling between the FM layers drives the sandwich structure back to the antiparallel magnetization, which denotes the higher resistive state. Thus, the stack can be

switched between high resistance and low resistance by means of an external magnetic field, which is the basis of giant magnetoresistive devices.

2.2.3 GMR multilayers

The described magnetoresistive effect can be multiplied, if the sandwich structure is enhanced to a stack that consists of several FM and NM metal layers in an alternating order, so that each FM sheet is in antiferromagnetic coupling to its adjacent ones¹¹⁰. Such a layer structure is referred to as *GMR multilayer* and is usually operated, in opposition to the description given above, in a current-in-plane (CIP) mode. The mean free path of the conduction electrons, *i.e.* the average length of ballistic transport between two scattering events, is in the order of 30 to 50 nanometers for typical metal films used in GMR multilayers¹²². Since this is much longer than the separation of the individual layers in the stack, the charge carriers pass many FM/NM interfaces also in case of lateral drift, which permits their spin dependent scattering. A CIP configuration is usually of great advantage for GMR multilayer elements, as a current-perpendicular-to-plane (CPP) device is more difficult to fabricate and has a very low resistance, which makes a relative resistance change difficult to measure.

A GMR multilayer stack composed of cobalt (Co) and copper (Cu) layers as FM and NM metal, respectively, which is fabricated in the 1st AFCM will serve as a model system throughout this study. This well-known system relies on in-plane oriented magnetic moments and exhibits a high GMR ratio with moderate saturation fields. An exemplary GMR curve measured on a structured Co/Cu multilayer specimen is shown in **figure 2.6a**. The GMR ratio is obtained by the change of electrical resistance $R(H)$ relative to the value at magnetic saturation R_{sat}

$$\text{GMR} = \frac{R(H) - R_{\text{sat}}}{R_{\text{sat}}} \quad (2.3)$$

and is usually expressed in percent¹²³. The field dependent sensitivity $S(H)$ of a magnetoresistive element, which is defined as the first derivative of the sample's resistance over the magnetic field divided by the resistance value¹²³:

$$S(H) = \left[\frac{dR(H)}{dH} \right] / R(H) \quad (2.4)$$

is also provided in the graph.

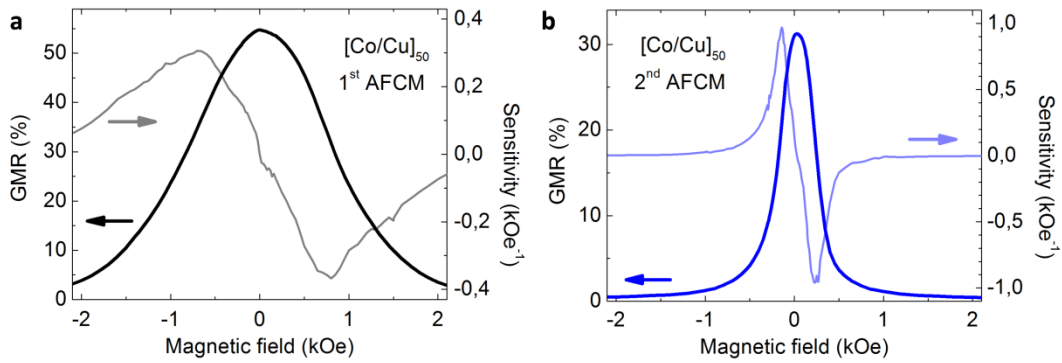


Figure 2.6 | GMR characteristics of Co/Cu multilayers: (a) GMR curve (black) and sensitivity (grey) of 50 double layers coupled in the first antiferromagnetic coupling maximum. (b) GMR curve (dark blue) and sensitivity (light blue) of 50 double layers coupled in the second antiferromagnetic coupling maximum.

The large change of electrical resistance in the presence of in-plane magnetic fields makes these structures ideally suited for magnetic field sensing elements in electronic circuits. However, several applications that will be highlighted throughout this work require the detection of small magnetic fields, *e.g.* the stray field from micro-sized magnetic particles. The sensitivity of GMR multilayers can be enhanced by going from the first to the 2nd AFCM⁹⁵ (*i.e.* from point a to d in figure 2.1), as shown in figure 2.6b for comparison. The weaker coupling strength between the FM layers results in a magnetization alignment at much lower fields. Although the GMR magnitude is reduced in this case and also magnetic saturation occurs at much lower fields, the sensitivity in this regime is increased significantly.

2.2.4 Spin valves

For a further increase in the sensitivity of magnetoelectronic sensing elements, *spin valve* stacks, which exploit the exchange bias coupling between antiferromagnetic and ferromagnetic layers, are used^{117,124}. They consist of a FM/NM/FM sandwich structure, where the magnetization of one of the ferromagnetic layers is pinned by the exchange bias effect from an adjacent antiferromagnetic layer. A respective layer system is schematically shown in **figure 2.7a**. Hence, the so-called magnetic free layer can switch its magnetization independent of the pinned one. Therefore, this GMR system exhibits two magnetoelectric states; antiparallel magnetizations of pinned and free layer: OFF-state (high resistance), parallel magnetizations: ON-state (low resistance), hence the term spin valve.

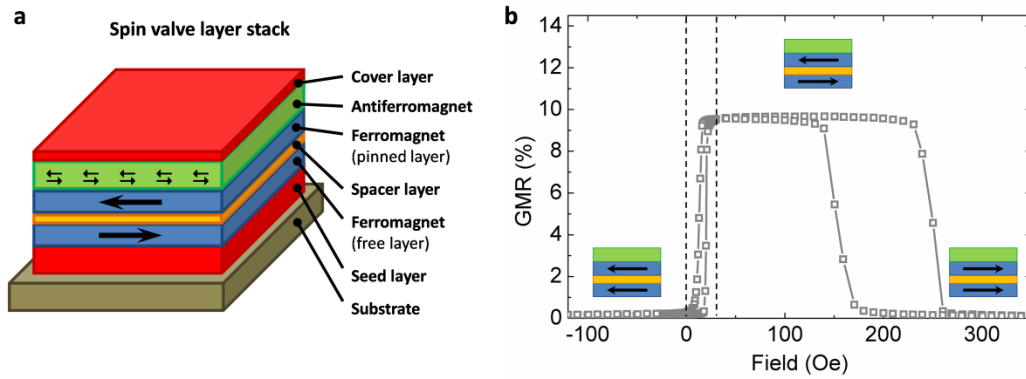


Figure 2.7 | Spin Valve: (a) layer structure of a typical top-pinned in-plane spin valve device. (b) GMR characteristic of a respective spin valve. The insets indicate the magnetic configurations of the two ferromagnetic layers at different fields.

If the free layer consists of a soft magnetic material, the magnetization reversal occurs at very low fields and the spin valve represents a very effective magnetoelectronic switch. Figure 2.7b shows the typical GMR characteristic (full loop) of a top-pinned spin valve device. At low fields, the switching of the free layer causes the steep edge of the GMR curve (minor loop between dashed lines) that acts as the sensor response. If the external field exceeds the exchange bias coupling, also the pinned layer switches and the system returns to a parallel configuration of magnetizations. The GMR curve clearly shows the separated loop of the pinned layer that is shifted along the field axis.

2.3 Theory of elasticity

In the following section, a brief introduction to the elasticity of rubbery materials is given. Starting with a description of an elastomer and the origin of elasticity, the fundamental quantities of stress and strain and their relation are defined in a general form, before they are simplified to the notation, which is used throughout the thesis. Finally, additional concepts with respect to rubber elasticity, that are relevant for the present work, are described.

2.3.1 Elastomeric materials

The term *elastomer* is derived from “elastic polymer” and thus refers to a polymer material, which undergoes mainly elastic deformations. The polymer chains of an elastomer are cross-linked to account for their mechanical stability and yield strength. The cross-linking, in most cases, is achieved by covalent bonds between the individual chains, as schematically illustrated in **figure 2.8**. This requires an irreversible chemical curing process, called vulcanisation, as discovered by Charles Goodyear and Thomas Hancock in the earlier 19th century, which results in an elastic material. These elastomers are referred to as *thermosets* or vulcanisates and represent the largest group of elastic materials¹²⁵. Another type is *thermoplastics*, which are cross-linked in a physical manner (mostly by dispensed crystallites of chain segments) and which can be plastically reshaped upon heating or by exposure to certain solvents¹²⁶.

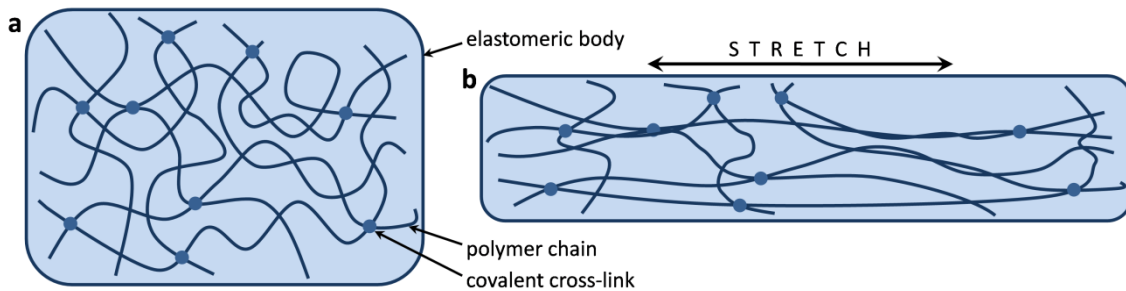


Figure 2.8 | Microstructure of elastomeric materials: The polymeric chains are chemically cross-linked; (a) relaxed state; (b) stretched state.

The cross-linked polymer chains of an elastomer are present in an amorphous state, as illustrated in figure 2.8a. As the material is stretched, the coiled chains extend and rearrange themselves in order to distribute the applied load throughout the macroscopic body. During this rearrangement, the molecular chains align along the axis of the tensile deformation, as shown in figure 2.8b. This involves a decrease in entropy due to the higher order in the system introduced by the preferential orientation of chain segments¹²⁷. Therefore, an entropically driven restoring force develops within the elastomer, which provides the fundamental elastic properties of the material. The cross-links, in this manner, prevent the translation of entire chains relative to each other upon deformation of the macroscopic body. The term elasticity means that after a deformation the material retrieves its original shape when the load is released. In the case of elastomeric materials, these elastic deformations can be very large, *e.g.* up to several hundred percent of tensile strain. Due to the entropic origin of the rubber elasticity, it is temperature dependent. Furthermore, the elastomer needs to be in a state above its *glass transition temperature*¹²⁸ to have enough movable chain segments to maintain its elasticity. However, the elastic deformation of a rubber not only causes polymer chain rearrangements. Particularly at higher strains, a fraction of the deformation energy is also stored as internal energy by changing atomic separations and distortion of bond angles inside the polymer chains. Due to the amorphous nature of elastomers, on a macroscopic scale, they can mechanically be treated as isotropic materials in their relaxed state.

2.3.2 Stress and strain

If a force is applied, every solid body undergoes a certain deformation. Often, the deformation cannot be adequately described by a single scalar, as it may be simultaneously compressed and sheared along different directions. In order to account also for such complex states of distortion in an elastic body, its deformation is expressed in a general notation by the co-called *strain tensor* $\boldsymbol{\varepsilon}$, represented by a 3 x 3 matrix. Also the forces inside the body, corresponding to the respective deformations, can be complex in three dimensions and are therefore represented in a similar form as a second order *stress tensor* $\boldsymbol{\sigma}$. The component σ_{ij} , for example, represents the force per unit area in the *i* direction acting on a plane whose normal is the *j* direction. In this notation, components with $i = j$ denote the normal stresses in the three dimensions of space and $i \neq j$ give the shear components.

Deformations in materials are often described by a linear relationship between stress and strain, similar to the well-known *Hooke's law*, whose analogon for continuous media is expressed by

$$\boldsymbol{\sigma} = -\boldsymbol{c}\boldsymbol{\varepsilon} \quad (2.5)$$

where \boldsymbol{c} is the *stiffness tensor*, which is of the 4th order and thus represented by 81 real components c_{ijkl} . However, due to symmetries of the three tensors, only 21 independent coefficients remain, and since elastomers are generally considered to be isotropic materials, they reduce to only 2 elastic parameters, which are characteristic to a certain rubber material. The bulk modulus K , describing the resistance to uniform compression, *i.e.* changes in volume and the shear modulus G , giving the ratio of shear stress to shear strain if a force is acting laterally.

Since in the present work, mainly *uniaxial deformations* are applied to characterize the performance of stretchable GMR sensors under strain, a one dimensional consideration of the described continuum mechanics can be used for a simplified, yet adequate description of stress and strain. **Figure 2.9** illustrates a uniaxial stretch on the example of a rubber bar with initial dimensions $W_0 \cdot D_0 \cdot L_0$ subjected to a force \vec{F} acting on the cross section along its length. L_0 is the original length of the bar before the force was applied. Upon stretching, the bar extends by ΔL along the axis of the applied force. The current length of the rubber bar under the influence of this normal force is $L = L_0 + \Delta L$. Due to the incompressibility constraint of elastomeric materials, they simultaneously, undergo a contraction along the transverse directions, referred to as the Poisson effect, which will be discussed in section 2.3.4.

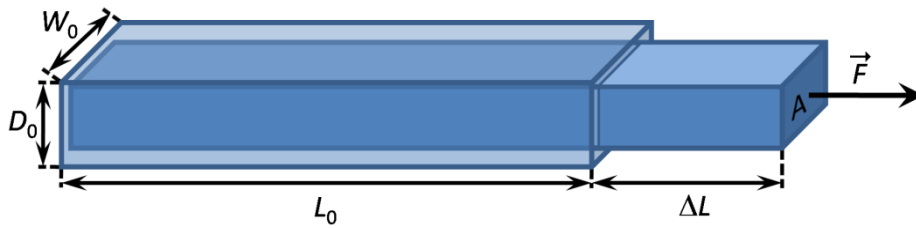


Figure 2.9 | Stretching of a rubber bar: The uniaxial tensile deformation due to a force \vec{F} applied on the face with area A along its length is illustrated.

If the deformation is restricted to such a uniaxial case, which means that only normal forces acting along one direction are taken into account, without any shear, the associated *strain* can indeed be quantified by a scalar ε , representing the ratio of change in length to original length:

$$\varepsilon = \frac{\Delta L}{L_0} = \frac{L - L_0}{L_0} = \frac{L}{L_0} - 1 \quad (2.6)$$

The strain is a dimensionless quantity, which can also be expressed as a percentage. Hence, a strain of $\varepsilon = 1$ or 100%, according to figure 2.9, denotes a deformation with a current length being twice the original length of the bar.

Since all forces considered in this uniaxial case are acting on the same cross-section A along the same direction, also the stress can be reduced to a scalar:

$$\sigma = \frac{F}{A} = \frac{F}{W \cdot D} \quad (2.7)$$

which has the dimension of a pressure and is usually expressed in units of pascal (Pa). W and D are the actual width and thickness of the rubber bar as it expands, respectively.

In a few experiments of this thesis, biaxial instead of uniaxial strain is used for preparation and characterization. The application of biaxial deformation along the lateral dimensions of elastomeric membranes is treated as follows. The total strain is identified by the applied uniaxial strains along two perpendicular directions, *i.e.* a biaxial strain of 10% x 10% denotes a state with $\varepsilon = 0.1$ along the x and y lateral directions, respectively. Alternatively, a scalar value for the *areal strain* ε_A , which corresponds to the ratio of change in area to original area, according to

$$\varepsilon_A = \frac{\Delta A}{A_0} = (\varepsilon_x + 1) \cdot (\varepsilon_y + 1) - 1 = \left(\frac{L_x}{L_{x0}} \cdot \frac{L_y}{L_{y0}} \right) - 1 \quad (2.8)$$

can be assigned. Hence, the biaxial strain of 10% x 10% gives a total areal strain of 21%.

2.3.3 Rubber elasticity

For the simplified case of uniaxial stress applied to an isotropic solid, Hooke's law can be expressed as

$$\sigma = E \cdot \varepsilon \quad (2.9)$$

with the proportionality factor E being the so called *Young's modulus* of the material. Materials with a higher E -value are mechanically stiffer, as more stress must be applied to result in the same amount of strain. However, for elastomers the relation between stress and strain is non-linear, as shown in **figure 2.10**. Here, Polydimethylsiloxane (PDMS, see section 3.1.1) is chosen as an exemplary elastomeric material, as it is mainly used throughout this work. The red line in the graph denotes a linear fit of the low strain region that can be described by Hooke's law, which provides the Young's modulus of the material in this regime. With higher strains, elastomers become softer, as they enter a plateau region in their stress-strain curve, before the slope rises again. This hardening of the material at high strains is associated with the gradual transition from the entropy reducing alignment of polymer chains towards a distortion and expansion of covalent atomic bonds upon stretching. Hence, a fixed Young's modulus is a valid approximation only for small amounts of deformation in elastomeric materials and nonlinear terms have to be taken into account for higher strain intervals. Different theories modelling the co-called *hyperelasticity* of rubber over large strains have been established over the decades, for example, the Mooney-Rivlin model¹²⁹ and the Ogden model¹³⁰.

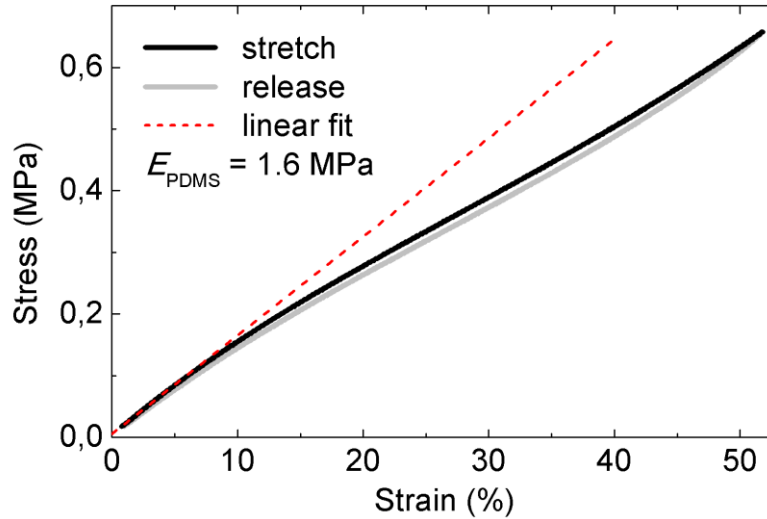


Figure 2.10 | Stress-strain behavior of elastomers: Stress strain curve of cross-linked poly(dimethylsiloxane) for loading (black) and unloading (grey). The dotted red line denotes a linear fit of the low strain region to determine the respective Young's modulus. Measurement performed in collaboration with Dr. K. Schneider and H. Scheibner (both IPF Dresden). Figure taken from [6].

The area below a stress vs. strain curve $\int \sigma d\varepsilon$ denotes the work introduced to the system during the respective deformation. Hence, the area of the hysteresis loop between loading and unloading is the energy dissipated, mainly by heat, during one loading cycle:

$$W_{\text{diss}} = \oint \sigma d\varepsilon \quad (2.10)$$

Different effects in rubber materials (*e.g.* viscoelasticity) may enhance the hysteresis to make up a significant amount of the area below the loading curve.

2.3.4 The Poisson effect

As shown in figure 2.9, upon application of uniaxial strain, a material does not only elongates along the direction of the applied force, but also contracts perpendicular to it, and vice versa. This is effect occurs due to a certain incompressibility of a material, which denotes its resistance to change its total volume during the deformation. A perfectly incompressible material would compress its cross-sectional area to the same extent as the length of the rubber bar increases as it is stretched. The exact amount of the transverse contraction, however, is different for different materials and is quantified by its *Poisson's ratio* ν . For a normal deformation along one direction it is defined as the derivative of transverse strain $\varepsilon_{\text{trans}}$ by the strain ε_{ax} along the axis of the acting force:

$$\nu = - \frac{d\varepsilon_{\text{trans}}}{d\varepsilon_{\text{ax}}} \quad (2.11)$$

Most materials have Poisson ratios between 0 and 0.5, however, also negative values (*i.e.* the transverse dimensions expand with applied tensile strain) are possible for example for foams¹³¹. Additionally, non-isotropic materials often exhibit a non-isotropic Poisson effect.

2.3.5 Viscoelasticity

With the instantaneous deformation of a rubber material upon applied force (or stress), another delayed and also time dependent deformation is often observed in addition. This phenomenon is often referred to as creep and is known for most polymers as well. It originates from an internal mechanical relaxation occurring in the material due to molecular rearrangements of weakly bond or entangled chains or chain segments. Those parts disengage and diffuse from their local environment, driven by the internal directional stress and mediated by the present alignment of adjacent chains in the same direction. Although the cross-linking in rubber materials suppresses a large directed drift of longer chain segments relative to each other, a marginal amount of this viscous behaviour can be found also in elastomers. Especially in soft rubbers, which exhibit a low cross-linking density and a low glass transition temperature, this effect may become significant. The simultaneous occurrence of viscous and elastic behaviour is commonly referred to as the *viscoelasticity* of a material¹³².

This property is reflected in a time dependent stress-strain relation. For example if a viscoelastic ribbon is exposed to a constant load (*i.e.* uniaxial stress), it first expands to a certain length and subsequently maintains a slowly creeping further elongation over time (*i.e.* increasing strain). Upon a quick relaxation, it does not immediately recover its initial length. Instead, the compression also occurs on a longer time scale that can be up to several days. For purely viscoelastic materials, the initial dimensions will be finally retrieved and no plastic deformation occurs. However, other phenomena present in rubber materials, like the Mullins effect¹³³, may lead to a fraction of the deformation that remains irreversible.

2.3.6 Bending strain in a stiff film on a flexible support

If a flexible sheet is bent, its outer surface experiences a tensile strain, while the inner surface is compressed, both along the tangential directions. One plane inside the sheet, known as the *neutral mechanical plane*^{9,134}, remains unstrained, independent of the bending radius R_b . If the sheet is fully homogeneous, this neutral plane is exactly the midsurface, and the tensile and compressive lateral strains grow linearly with the separation outward and inward from that plane, respectively. From a purely geometric consideration, the bending strain ε_b on the outer surface is given by

$$\varepsilon_b = \frac{d}{2R_b} \quad (2.12)$$

with d being the sheet thickness. Hence, the minimum radius before reaching a critical tensile strain on the surface scales linearly with the thickness. However, if a film is present on the outer surface, that is stiffer than the flexible sheet ($E_{\text{film}} > E_{\text{sheet}}$) the NMP shifts toward the film, which reduces its bending

strain. Z. Suo *et al.* suggested a model that computes the bending strain in the stiff film on a flexible support¹³⁴:

$$\varepsilon_b = \left(\frac{d_f + d_s}{2R_b} \right) \frac{(1 + 2\eta + \chi\eta^2)}{(1 + \eta) \cdot (1 + \chi\eta)} \quad (2.13)$$

with $\eta = d_f/d_s$ and $\chi = E_f/E_s$ being the ratios of thicknesses and Young's moduli for the film and sheet, respectively. Since $\chi \ll 1$ for stiff metal films on soft polymeric substrates, the flexible support should be as thin as possible to allow for small bending radii, before reaching a critical strain in the stiff film.

2.4 Approaches to stretchable electronic systems

High speed electronic elements and circuits are made of mainly rigid and brittle materials, like silicon, metals and ceramics, which are not intrinsically stretchable. Metal films, for example, can be stretched by not more than 1% before fracture^{135,136}. In order to produce stretchable versions of functional electronic elements with similar performance, they should at first be prepared on elastic supports and additionally the entire system needs to be able to accommodate tensile strains without stretching the functional materials above their rupture strain. Mediated by the ambitious development of stretchable electronics during the last years^{1,2,11}, different approaches have been suggested to achieve this goal. The ones that are applicable to layered structures are to be reviewed in this section and their advantages and disadvantages, especially in the scope of magnetoelectronic elements, are worked out.

2.4.1 Microcrack formation

If a free standing film or ribbon of a brittle material is subjected to tensile strains, ultimate failure usually occurs as a single crack perpendicular to the applied stress that tears apart the specimen. For thin and smooth films on a compliant substrate, the stress is not ultimately released by the formation of a single rupture gap and thus, several cracks may occur with a certain mean spacing^{137,138}. If the strain is increased further, more and more cracks occur to accommodate the tensile deformation. However, usually the first cracks already separate the brittle films completely, which makes it impossible to use them for functional electronic elements.

S. P. Lacour *et al.* observed, that thin gold films deposited on rubber substrates can exhibit a *microcracked* morphology¹⁰², as shown in **figure 2.11a**. Later it was shown, that this mainly originates from an inherent tensile stress, which depends on several preparation parameters, like film thickness and deposition temperature¹⁰⁰. Although cracked, the metal films were electrically conductive, since the gold ligaments form a percolating network across the surface (figure 2.11b, left). On the one hand, the highly cracked metal surface leads to a high electrical resistivity of thin film wires; on the other hand the percolation was maintained for applied lateral strains beyond 20%¹³⁹, as schematically shown in figure 2.11b. Stretchable metal interconnects that could be elastically stretched over more than

100,000 loading cycles providing a relatively stable electrical connection, were demonstrated using this approach⁵⁹.

The mechanism of microcrack formation on soft supports was further advanced by preparing thin metal films of soft capped elastomeric foams instead of compact rubber substrates¹⁴⁰. In this case, the formation of microcracks is localized above the underlying voids (figure 2.11c) and the areas above the walls remain free of cracks to form a stable percolating network. Surface electrodes could be stretched beyond 100%, which was demonstrated in conformable capacitive pressure sensors prepared using this technique²².

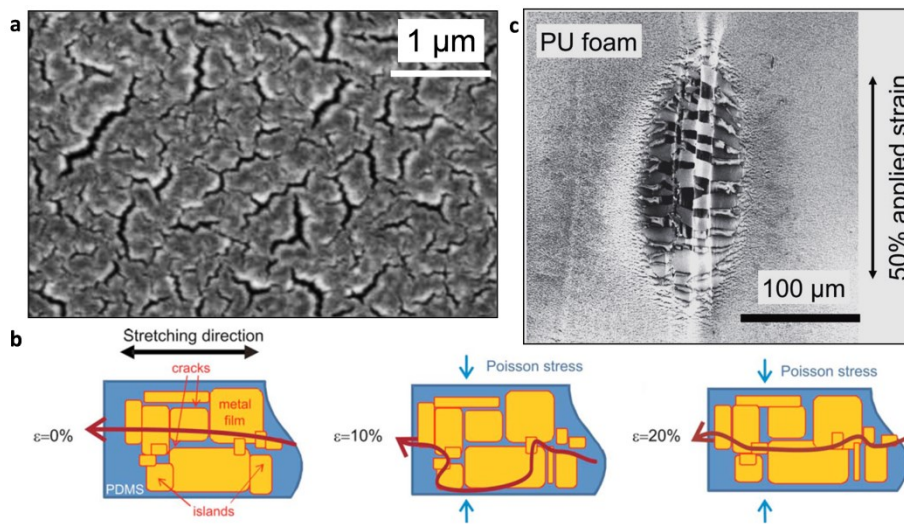


Figure 2.11 | Microcracks in metal films on elastomeric supports: (a) SEM image of a 100 nm thick gold film on rubber with a network of randomly arranged microcracks induced by deposition. (b) Schematic illustration of a respective model based on gold islands on rubber and corresponding conducting percolations paths for different applied strains. (c) SEM image of a 25 nm thick gold film on a surface skin of a polyurethane (PU) foam showing the concentration of cracks above a single cavity under 50% strain. Figure compiled from [26,140,141].

Despite the high stretchability and good long-term performance, the microcrack approach leads to electrodes with varying resistance upon stretching^{140,141}, which is of great disadvantage for magnetoresistive sensor elements. Furthermore the strong morphological transitions associated with the formation of the percolating network are expected to have an influence on the GMR response by means of magnetic shape anisotropy¹¹¹.

2.4.2 Meanders and compliant patterns

Instead of relying on crack formation for the development of percolating networks, it is possible to prepare compliant patterns in films of rigid material on soft substrates using lithographic structuring methods. T. Li *et al.* developed a model for the maximum lateral strains in *meander* ribbons of a stiff material on rubber with stretching, depending on the ratio between amplitude and wavelength¹⁴². Simulations have shown large out-of-plane distortions of the serpentine structure upon stretching, which effectively transforms the tensile deformation of the system mainly to a bending of the rigid

material¹⁴³ (figure 2.12a). In this manner, such a meander structure represents a 2D spring that can facilitate high uniaxial strains. However, due to the large shear stress imposed on the functional layer, a large thickness is beneficial to prevent the structure from breaking at higher strains. The approach of metal meanders was mainly used to fabricate highly conductive stretchable interconnects²⁹ and antennas⁵³. Later, the geometry and preparation of the meanders was further optimized to horseshoe-shapes^{20,30,144} or self-similar^{32,52} designs embedded into microstructured polymer supports, which makes these interconnects able to accommodate up to some hundred percent of tensile deformation. Besides simple meanders, other compliant network patterns have recently been developed (figure 2.12b), which enable biaxial stretching and are optimized also towards their spatial yield^{12,32,58}.

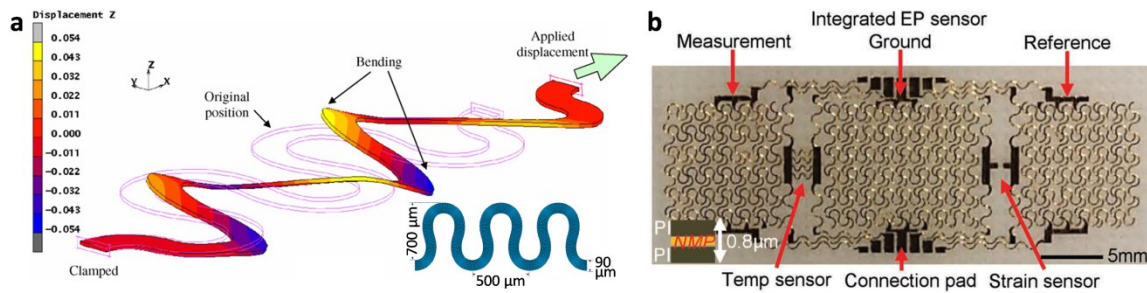


Figure 2.12 | Stretchable meander electrode patterns: (a) Finite elements method (FEM) simulation of the out-of-plane deformation of a 15 μm thick copper meander stretched by 20%. The inset on the lower left is showing the planar geometry of the unstrained meander. (b) Multifunctional epidermal electronic system including an electrophysiological sensor constructed in an array of filamentary serpentine structures. Figure compiled from [30,58].

The use of compliant meander structures for stretchable magnetoelectronics is feasible¹⁴⁵. However, since the total thickness of GMR layer stacks is about 100 nm, demanding preparation procedures would be needed in order to fabricate highly elastic sensor elements relying exclusively on this approach.

2.4.3 Surface wrinkling

A thin film of a stiff material deposited or laminated onto a pre-stretched elastomeric substrate, as illustrated in figure 2.13a, undergoes a morphologic transition by formation of periodic out-of-plane buckles, as the pre-strain is released^{24,146,147}. This phenomenon is called *wrinkling*¹⁰¹ and occurs as soon as a critical compressive strain is exceeded, which depends on the mechanical properties of both materials. Based on nonlinear analyses of the bilayer system, proposed by Z. Y. Huang *et al.*¹⁴⁸, the critical strain ε_c for the formation of wrinkles can be computed by:

$$\varepsilon_c = 0.52 \left[\frac{E_s(1 - \nu_f^2)}{E_f(1 - \nu_s^2)} \right]^{2/3} \quad (2.14)$$

via the Young's modulus E and Poisson's ratio ν of the substrate s and film f materials, respectively. This critical strain provides the energy necessary to form the out-of-plane distortions of the substrate and allow for film bending.

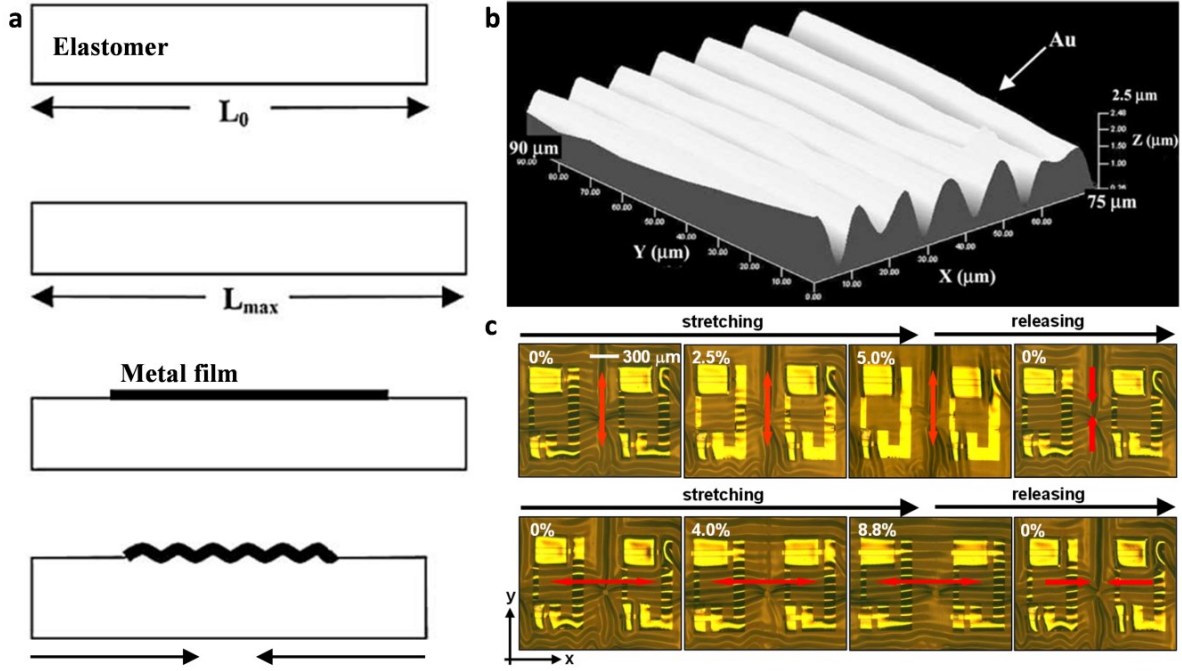


Figure 2.13 | Wrinkle formation in stiff films on soft supports: (a) General fabrication scheme of a wrinkled metal film for stretchable electronics, by deposition onto a pre-stretched elastic support and subsequent release of pre-strain. (b) 3D profile of a wrinkled gold surface after release from 15% uniaxial pre-strain. (c) Biaxially wrinkled Si-based inverters on rubber, stretched and released in y - (top) and x -direction (bottom). Figure compiled from [9,149].

Figure 2.13b shows a 3D profile of a wrinkled gold film after uniaxial compression from 15% pre-strain. The wrinkling of hard skin on soft membranes exhibits a characteristic periodicity that scales with the thickness of the film. N. Bowden *et al.* suggested a model for the determination of the wrinkling period λ^{24} :

$$\lambda = \frac{\pi d}{\sqrt{\varepsilon_c}} = 4.36d \left(\frac{E_f(1 - \nu_s^2)}{E_s(1 - \nu_f^2)} \right)^{1/3} \quad (2.15)$$

with d being the thickness of the stiff film. This calculation holds for films firmly attached to a softer substrate with a thickness much larger than d . It only determines the initial wrinkling period upon reaching the critical strain, as with further shrinkage of the soft support, the wrinkles are compressed accordingly.

The described phenomenon can be exploited for stretchable electronic systems, because a wrinkled nanomembrane can accommodate tensile strains by levelling out its buckles^{25,35}. In the ideal case, the film can be stretched until the original pre-strain is reached (*i.e.* the point where the film is flat again). According to investigations performed by D.-Y. Khang *et al.*, the lateral strains in the folded stiff film upon stretching are dominated by the bending, as long as the wavy pattern remains³⁵. The peak strain can thus be approximated by:

$$\varepsilon_f^{\text{peak}} = 2\varepsilon_c \sqrt{\frac{\varepsilon_{\text{pre}} - \varepsilon_{\text{appl}}}{\varepsilon_c}} - 1 \quad (2.16)$$

with ε_{pre} and $\varepsilon_{\text{appl}}$ being the used pre-strain and currently applied strain on the substrate, respectively. The wrinkling approach is the only one that allows also closed large area membranes to be stretched without cracking. Nevertheless, also other materials, which are not present as a closed film, like carbon nanotubes or other types of nanowires, can exhibit compliant properties using wrinkles⁴¹. Furthermore, it can lead to biaxial stretchability if the elastomeric substrate is pre-stretched in both lateral dimensions³⁶. As shown in figure 2.13c, these features have led to the design of more functional and highly integrated stretchable electronic systems relying on surface wrinkling^{9,13,40,41}.

The surface wrinkling approach is comparatively simple in terms of fabrication and leads to a stretchability of pure metal films in the range of several tens of percent. In the case of buckled magnetic nanomembranes, the local out-of-plane tilting on the sides of the wrinkles may cause an influence on the sensor response due to the resulting local out-of-plane components of in-plane applied magnetic fields.

2.4.4 Rigid islands

This approach relies on distributed functional elements or clusters prepared on arrays of rigid islands, which are attached to an elastic carrier and electrically linked by highly stretchable interconnects^{33,150}, as shown in **figure 2.14a**. These systems resemble a mesh layout with functional nodes and are mostly fabricated using transfer printing techniques¹⁵¹.

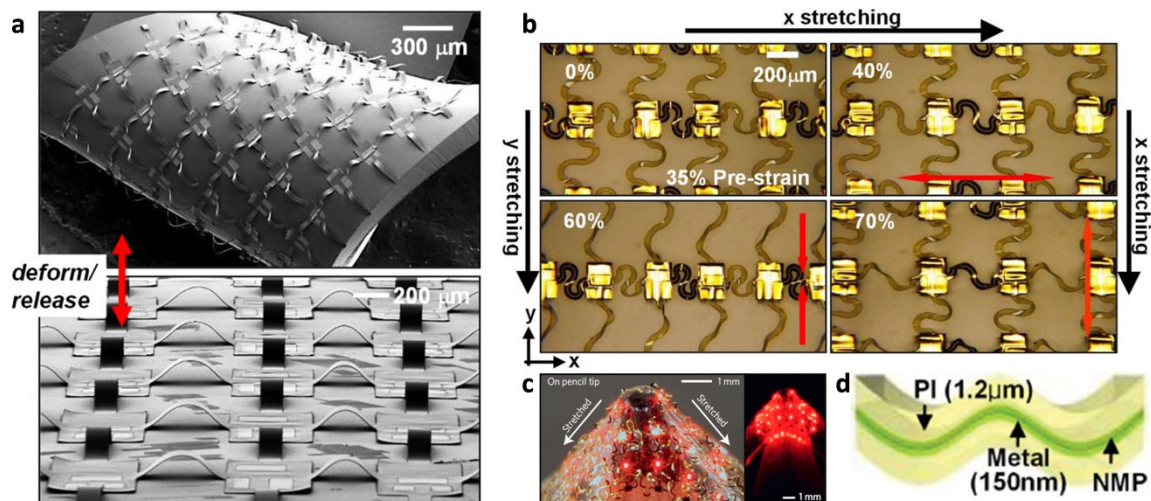


Figure 2.14 | Stiff islands with compliant interconnects for stretchable electronics: (a) Array of stiff islands housing CMOS inverters linked by buckled interconnects on an elastic support, in a twisted (top) and flat (bottom) state. (b) A similar array using more compliant serpentine bridge designs as interconnects stretched in the x- and y direction. (d) 6 x 6 array of μ -LEDs in a mesh design stretched on a pencil tip. (c) Encapsulation of the electronic interconnects between two thin polymer sheets of polyimide (PI) close to the neutral mechanical plane (NMP). Figure compiled from [17,18,152].

Upon stretching, the compliant electrical bridges accommodate the lateral deformation, *e.g.* by means of wrinkling or meander shapes, while the functional islands ideally remain unstrained and just increase their distance to each other (figure 2.14b). Hence, it is possible to directly convert established

electronic architectures, containing also most brittle and materials, to stretchable systems^{1,17,153}, without relying on thin film based electronic components, only. This motivated the fabrication of a variety of highly functional and stretchable systems using this approach ranging from integrated circuitry¹⁵², electronic eye cameras¹⁵⁴, light emitting diodes¹⁸ (figure 2.14c), batteries⁵² as well as on-skin thermal⁴⁴ and implanted physiological sensors⁶⁷. Also, a similar design of reversely compliant electronic mesh structures relying on free standing plastic foil without the use of elastomeric materials has recently been demonstrated¹⁴.

Despite the overwhelming potential in terms of functionality, this approach has the draw back of a low spatial yield, since only micro sized elements are distributed with a large separation. No large area elements are supported using this technique. Furthermore, strain concentration, usually occurring on the hard-to-soft interface at the edges of the rigid islands¹⁵⁵, demand a particular robustness and adhesion of the mesh structures on these locations¹⁵⁶. Therefore, in most cases, the metallic interconnects are encapsulated between two flexible polymer sheets, as shown in figure 2.14d, to increase their yield strength. Hence, reliable device fabrication is usually highly demanding and the stretchability does not exceed 20% in most cases.

Table 2.1 | Approaches to stretchable thin film electronics: The table summarizes the key parameter of the discussed approaches to achieve stretchability in electronic systems. Images adopted from [1,9,29,141].

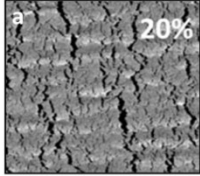
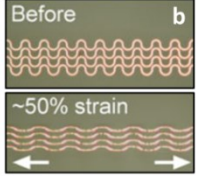
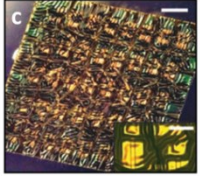
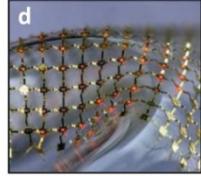
Approach:	Microcracks	Meander patterns	Surface wrinkling	Rigid islands
Example:				
Difficulty:	easy	medium	easy-medium	demanding
Stretchability:	low - medium	medium - high	medium	low - medium
Applications:	interconnects, capacitive sensors	interconnects, medical sensors	surface electrodes, integrated circuits	complex electronic systems
Peculiarity:	resistance changes with stretching	preferential with larger film thickness	large area and extended films	functional elements isolated from strain

Table 2.1 summarizes the technological approaches to stretchable electronics described above, and gives a comparison of the associated key attributes. Beside those mentioned so far, also other approaches to stretchable electronics have been demonstrated, including microfluidic circuits using eutectic metal alloy^{19,157} or devices relying entirely on intrinsically stretchable materials^{37,51}. Despite their impressive capabilities, these technologies are not compatible with metallic thin films and thus not considered for the preparation of stretchable magnetoelectronic devices in this work.

3. METHODS & MATERIALS

3.1 Sample fabrication

The giant magnetoresistive sensor elements presented in this work are prepared by thin film technologies that are well-established for the deposition onto conventional rigid silicon wafers. The choice and preparation of soft substrate materials is a key aspect for a successful realization of stretchable magneto-electronic devices. Furthermore, lithographic patterning processes are utilized to structure the functional nanomembranes into defined sensing elements. All important preparation details and materials that are used for the different sensor designs throughout this thesis are described in this subchapter. Special attention is also given to topographical pre-characterizations of the sample surfaces at different fabrication states, as this has a significant influence on the performance of the prepared GMR elements. These investigations are done by means of atomic force microscopy (AFM).

3.1.1 Polydimethylsiloxane (PDMS)

Stretchable electronic devices usually require stretchable supports they are situated on. Since the amount of material used for the substrate typically makes up more than 99% of the entire electronic element (roughly 50 μm substrate vs. about 100 nm of active material), it mainly determines the mechanical parameters of the final device. The elastic material typically used for stretchable electronics is *Poly(dimethylsiloxane)* PDMS^{1,2,25}, which is well-known also in other fields of material science^{158,159} and widely used in the food, cosmetics and medical industry. **Figure 3.1** shows the chemical structure of the PDMS polymer chain, which can macroscopically behave, depending on the degree of polymerization n , as an oleaginous liquid, a gel or a viscoelastic solid. The covalent bonding angle of about 140° between the backbone atoms gives the polymer chain an intrinsic stretchability¹⁶⁰. However, in order to obtain good elastomeric properties, chemical cross-linking has to be induced, which is usually done by means of a curing agent and often at elevated temperatures.

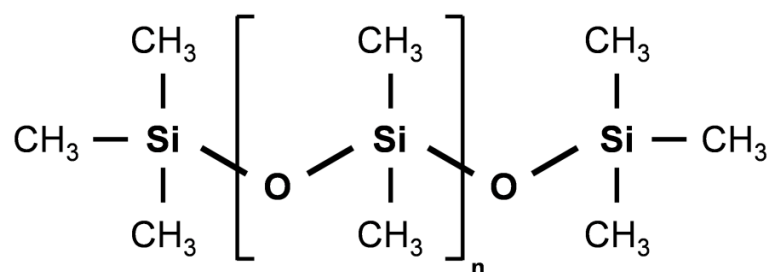


Figure 3.1 | PDMS: Chemical structure of a PDMS polymer chain with its characteristic $[\text{Si-O}]_n$ backbone.

Cured PDMS features good optical transparency and is non-toxic. The combination of organic and inorganic attributes offers several specific properties, which distinguishes this silicone based rubber from other polymeric elastomer materials. The large difference in the electronegativity of 1.7 between the silicon and oxygen provides the backbone a very strong binding energy, which results in a low

flammability and high durability versus temperature as well as UV and oxidizing chemical exposure¹⁶¹. At the same time, the Si-O single covalent bonds allow for a free torsion along the axis of the backbone and in combination with the weak intermolecular van-der-Waals interaction, this imparts a very high chain mobility¹⁶², which is beneficial for the elastic properties even at temperatures as low as -100°C. Furthermore, it drives the non-polar methyl side groups to orient towards the surface (to air), screening the inorganic chains. This results in a very low surface energy (≈ 20 mJ/m²) that accounts for a strong *hydrophobic* character and low adhesion of PDMS¹⁶⁰. Both surface properties can be strongly modified by means of a *plasma treatment*, which breaks up chemical bonds and forms reactive radicals. Especially the exposure to oxygen plasma is known to turn the PDMS surface from hydrophobic to hydrophilic and allows strong irreversible binding to itself or other plasma activated surfaces like glass or oxidized silicon wafers¹⁵⁸. Under ambient conditions (*i.e.* in air at room temperature), however, these surface transitions decay over a time scale of some minutes, as the so-called *hydrophobic recovery* sets in. This is caused by the high chain mobility, which allows untreated methyl groups to rapidly migrate to the surface from the bulk phase just underneath, which recreates a thin non-polar and inert surface layer screening the just activated parts. Plasma treatment is used in this work to adhere magnetic sensor structures to PDMS in a specifically developed direct transfer process¹⁶³.

The stress-strain curve of cured PDMS, as it is used throughout this thesis, for loading and unloading is shown in figure 2.10. As discussed in section 2.3.3, in elastomeric materials, a constant Young's modulus can only be defined for small amounts of deformation. For the low strain region, a value of $E_{\text{PDMS}} = 1,6$ MPa is determined from the stress-strain experiment. Furthermore, the low hysteresis between the loading and unloading curves (<4%) account for the small amount of viscoelasticity present in cured and cross-linked PDMS and highlights its good elastic properties.

3.1.2 PDMS film preparation

The product used here is Sylgard[®] 184 (Dow Corning) and is shipped as a pre-polymer gel and a liquid curing agent. The two parts are thoroughly mixed in a 10:1 ratio and subsequently degassed in a desiccator. At room temperature, the pot life of the prepared PDMS blend (*i.e.* time it needs during the curing process to double its viscosity after mixing) is about two hours. In order to obtain elastomeric films, it is spin coated onto silicon handling wafers. Beforehand, to allow a gentle peeling of the PDMS membrane from the rigid support after sensor fabrication, a thin photoresist film (AZ[®] 5214E, Microchemicals) is spin coated on the wafer for 35 seconds at 4.500 rpm and backed on the hot plate at 90°C for 5 minutes. This film serves as an anti-stick layer for the PDMS film, which yet endures a suitable adhesion to keep it supported during the entire fabrication process. The spin coating of the PDMS itself, if not stated differently, is performed at 2.000 rpm for 35 seconds and subsequent curing in an oven at 90°C for 30 minutes under continuous nitrogen flow.

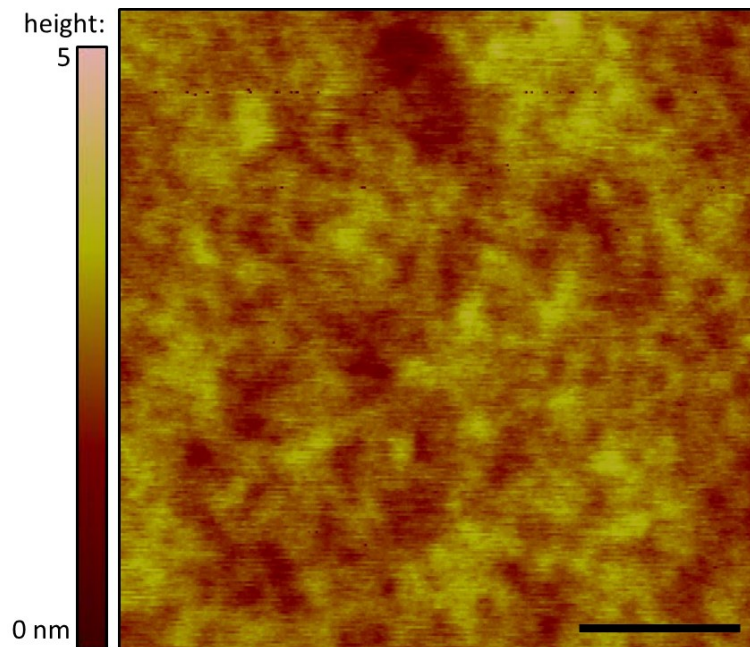


Figure 3.2 | Surface topography of the PDMS substrate film: AFM micrograph of the PDMS film surface after curing. For the shown surface section of $(2 \times 2) \mu\text{m}^2$, the value of the root-mean-square roughness is 0.38 nm (scale bar: 500 nm). AFM measurement was performed in collaboration with Barbara Eichler (IFW Dresden).

This procedure described above results in a smooth elastomeric film of $40 \mu\text{m}$ thickness with the elastic properties shown by the stress–strain curve in figure 2.13. The PDMS film is weakly adhered to the rigid handling wafer due to the anti-stick layer underneath. As described in section 2.1.3, one of the key requirements to the substrate for the growth of GMR layer stacks is the surface roughness being as small as possible to avoid the degradation of the sensor performance by local misalignment of magnetic moments – the effect known as orange peel coupling¹¹⁵. Spin coating is known to lead to very smooth films if the medium is homogeneous. **Figure 3.2** shows an AFM micrograph of the PDMS film surface after curing, which possesses a roughness of only 0.38 nm in the visible area of $2 \times 2 \text{mm}^2$. This value is in the same order as for the oxidized surface of a conventional silicon wafer, which was determined in a similar measurement to be 0.25 nm. This already gives a promising hint towards the qualification of this soft substrate for the preparation of high performance GMR sensor structures.

3.1.3 Lithographic structuring on the PDMS surface.

A photolithographic lift-off patterning procedure is performed on the prepared PDMS surface to structure the GMR films into individual elements of defined size and shape. This renders the fabrication process compatible to current microelectronic structuring procedures. The chosen sensor design for most of the elements fabricated in this work is shown in **figure 3.3a** and represents a sample stripe of $1 \times 16 \text{mm}^2$ size equipped with four contact pads for electrical connection. This structure was mainly chosen for ease of precise characterization of the fabricated elements, as it allows for reliable

four-probe electrical resistance measurements and GMR characterizations, compatible with the used magnetoelectric test equipment described in sections 3.2.1 through 3.2.3. For some of the presented studies, this design was adapted according to figure 3.3b to obtain a more compliant pattern of a serpentine meander, as described in section 2.4.2.

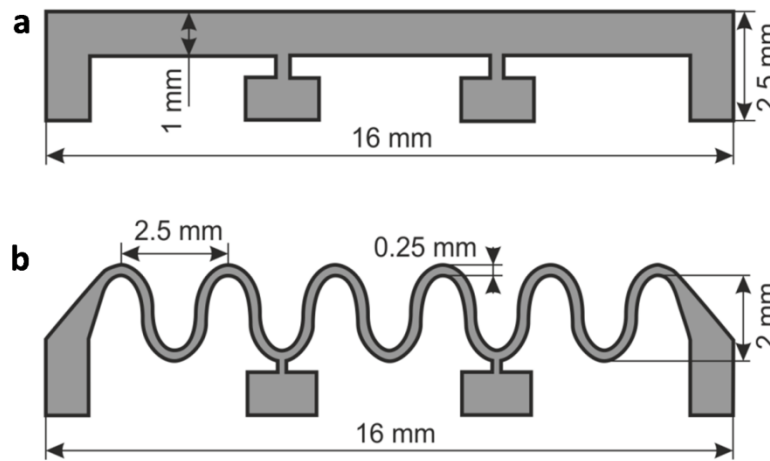


Figure 3.3 | Sensor geometry: Dimensioning of the lithographically defined sensor structures. (a) Stripe pattern, which is commonly used in this work. (b) adapted pattern of a compliant serpentine meander. The lithographic mask of (a) was provided by Dr. Ingolf Mönch (IFW Dresden). Figure assembled from [145].

For lithographic structuring, a layer of photoresist is spin coated onto the PDMS surface. Due to the hydrophobic nature of PDMS, the wetting behavior of the photoresist is poor, which requires several adaptations of the established photolithography process valid for rigid substrates and a very careful handling during this preparation step. The utilization of an oxygen plasma surface treatment, which is usually recommended in the case of bad wettability, results in photoresist material being covalently bonded to the PDMS surface and remaining after development¹⁶⁰. This increases the roughness of the substrate surface in these areas to about 1.8 nm, as shown in **figure 3.4**, which is unfavorable for the deposition of magnetoelectronic layer stacks. Among the available photoresists, the chosen AZ[®] 5214E (Microchemicals) provides the best wettability on PDMS. For spin coating, it is poured onto the rubber film fixed into a well leveled spin coater, until it is spread over the entire sample surface. Spinning starts immediately with a short pre-coating step at 500 rpm for 2 seconds, followed by 3,500 rpm for 30 seconds with acceleration of 6,000 rpm/s. A gentle breeze of dry nitrogen on the film during spinning promotes fast drying. The regular pre-backing on a hot plate results in the formation of many cracks in the photoresist film and is therefore avoided. These cracks induce paths of conductive material in the final sensor structure, which may result in electrical short-cuts. Instead, the spin coated substrate is quickly transferred for 20 minutes into a nitrogen flow oven at 90°C before dewetting sets in. This results in a significant reduction of cracks in the cured photoresist film.

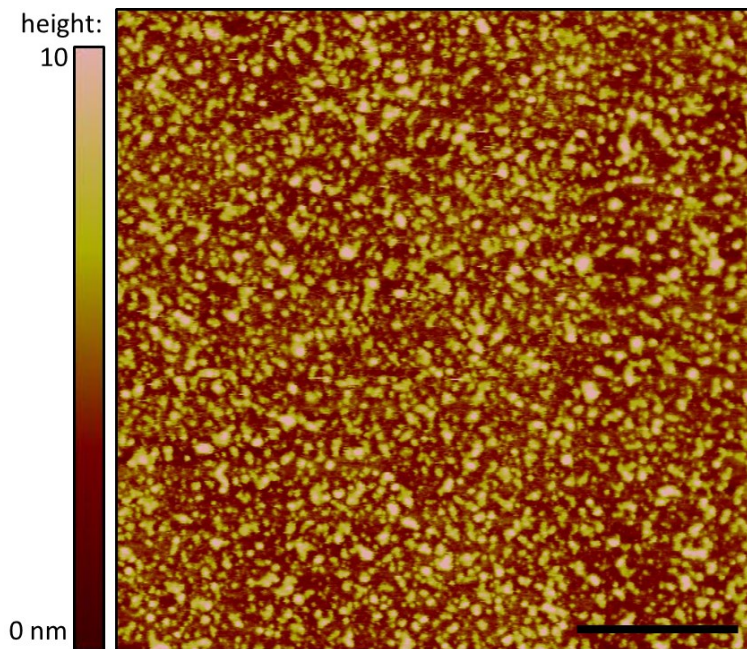


Figure 3.4 | Plasma treated PDMS surface after photoresist development: AFM micrograph of the PDMS film surface, which was subjected to oxygen plasma (30 W for 30 seconds) to enhance its wettability. The image was recorded after the lithographic processing, on an area where the photoresist film was removed by the developer. For the shown surface section of $2 \times 2 \mu\text{m}^2$, the value of the root-mean-square roughness is 1.8 nm. Further developing did not improve the value significantly (scale bar: 500 nm). AFM measurement was performed in collaboration with Barbara Eichler (IFW Dresden).

UV exposure is performed in a mask aligner (MA56, Süss microtech) equipped with a mercury-vapor light source for 13 seconds through a mask containing positive patterns of the sensor layout. The structures are developed in the corresponding AZ 726 developer for 70 seconds, which results a good edge quality. Subsequently, the thus prepared substrates are rinsed in deionized water for at least 10 minutes and dried by means of a nitrogen gun.

3.1.4 Magnetic thin film deposition

The fabrication of functional magnetoelectronic layer systems requires the successive deposition of magnetic and non-magnetic thin films with excellent interface qualities. The standard technique for this purpose is *magnetron sputter deposition*⁹⁵, which relies on the ejection of atomic species from the target material due to a plasma ion bombardment, as schematically shown in **figure 3.5a**. The use of magnetron sputtering techniques allows for deposition at lower process pressures. This results in less contaminations from built in process gas atoms in the growing film. The accurate layer thickness control (sub-Å regime) provided by this method is in particular important to precisely tune the interlayer exchange coupling in GMR multilayer structures, especially at the 2nd AFCM. Careful management of the process parameters can also lead to manipulate built in stresses during deposition.

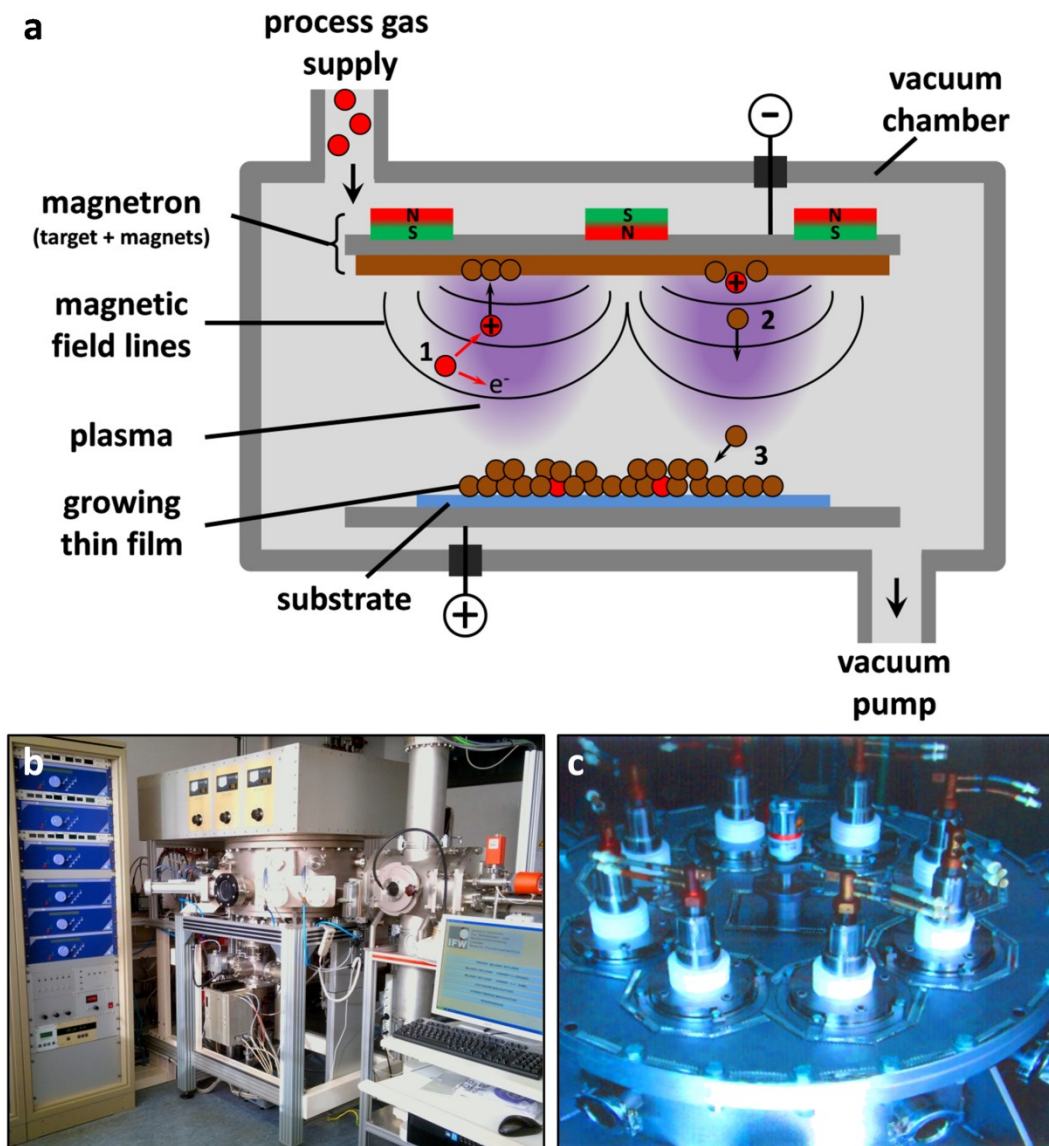


Figure 3.5 | Magnetron sputter deposition: Schematic illustration of DC magnetron sputtering. Step 1: The plasma ionizes process gas atoms, which are accelerated towards the target. Step 2: The ion impact ejects atoms from the target material that drift through the chamber. Step 3: Condensation of sputtered atoms from the gas phase leading to film growth on the substrate. **(b)** Magnetron sputter deposition setup used to prepare GMR stacks in this work. **(c)** Circular configuration of 8 magnetrons mounted on the top of the vacuum chamber. The system is mainly operated and maintained by Irina Fiering and Rainer Kaltfen (both IFW Dresden).

The magnetron sputter system used throughout this work is an in-house design of an 8 target chamber with a load lock, as introduced in figure 3.5b. The base pressure is 1×10^{-7} mbar. The setup is equipped with 3 direct current (DC) and 3 radio frequency (RF) generators that can be assigned to each of the targets. The water cooled magnetrons are arranged in a circular layout (figure 3.5c), which allows the substrate to be easily positioned below each target by means of an internal horizontal transfer carousel. This allows freely choosing the number, order and thickness of the target materials to be deposited on up to eight substrates in a single process. Besides a stationary deposition routine (shutter is opened for a defined period of time while the substrate rests below it), the circular

arrangement allows for an intermittent deposition where the shutter remains opened while the carousel constantly rotates below the glowing plasma discharge for a defined number of rounds with a fixed speed. The latter routine takes advantage of introduced vacuum interfaces, since the slowly growing film surface remains in the process atmosphere for the time of rotation until it passes the open shutter again. During this time, remnant gases adsorb at the surface and act as a surfactant during the sputter process, which leads to smoother film surfaces and thus higher interface qualities in multilayer systems^{164,165}. Furthermore, it results in a more homogeneous film thickness across the substrate area by eliminating the deposition rate variation in the tangential direction of the carousel rotation, which is beneficial for larger sample sizes or arrays. All depositions are performed at room temperature under an Ar atmosphere of 7.5×10^{-4} mbar. The deposition rate is typically in a range of 1-2 Å/s, depending on the material and plasma power. The magnetron sputtered nanomembranes exhibit a polycrystalline microstructure with a pronounced (111) texture and an average lateral grain size of ≈ 20 nm¹⁴⁵.

3.1.5 GMR layer stacks

As described in sections 2.2.3 and 2.2.4, different kinds of magnetic layer stacks can be used to create thin films with giant magnetoresistive properties⁹⁵. In this work, mainly GMR multilayers (**figure 3.6a**) but also spin valve stacks (**figure 3.6b**) are deposited onto the prepared elastomeric films using the procedures described above. In case of GMR multilayers, four different stacks are used, which all have their unique features in their magnetoelectric response, according to the respective magnetic properties and coupling strengths (as described in sections 2.1.1 and 2.2.3)¹⁶⁶. The exact layer sequences are as follows:

Co/Cu multilayer in the first AFCM ($[\text{Co}/\text{Cu}]_{50}^{1\text{st}}$):	Co(1)/[Cu(1.2)/Co(1)] ₅₀
Py/Cu multilayers in the first AFCM ($[\text{Py}/\text{Cu}]_{50}^{1\text{st}}$):	Py(1.9)/[Cu(0.9)/Py(1.9)] ₅₀
Co/Cu multilayers in the second AFCM ($[\text{Co}/\text{Cu}]_{30}^{2\text{nd}}$):	Co(1)/[Cu(2.2)/Co(1)] ₃₀
Py/Cu multilayers in the second AFCM ($[\text{Py}/\text{Cu}]_{30}^{2\text{nd}}$):	Py(1.5)/[Cu(2.3)/Py(1.5)] ₃₀

All thickness values are given in nm and Py denotes the soft magnetic permalloy ($\text{Ni}_{81}\text{Fe}_{19}$). Copper is used as the spacer layer, as its ductile properties provide high mechanical resilience upon deformation^{7,45}. The sputter parameters for all multilayer systems are optimized to result in the maximum GMR response. After deposition, the GMR films on PDMS are smooth with a surface roughness of below 1 nm and no buckles or microcracks are observed^{145,164}. This indicates only low lateral stresses being built into the deposited multilayers during sputtering. A detailed description of the specific features and magnetoelectric characteristics of the four systems prepared on elastomeric supports¹⁶⁶ can be found in the results chapter (section 4.1.5).

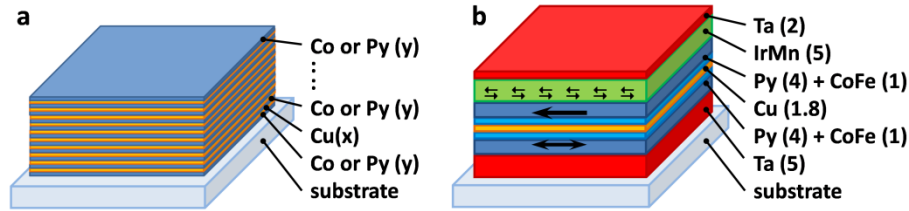


Figure 3.6 | Deposited GMR layer stacks on PDMS: (a) GMR multilayer stack consisting of ferromagnetic and non-magnetic metal layers in an alternating order. Depending on the choice of the ferromagnet and the AFCM (depending on the exact layer thicknesses) four different multilayer systems were realized. 50 and 30 double layers were used for the first and 2nd AFCM, respectively. (b) Layer structure of a symmetrical top-pinned spin valve (thicknesses given in nm). Depositions were mainly performed by Irina Fiering and the spin valve stack was designed and optimized in collaboration with Gungun Lin (both IFW Dresden).

In addition to the GMR multilayers, a spin valve layer stack was employed on similarly prepared PDMS substrates to create stretchable GMR sensors with high sensitivities and to demonstrate the potential of the developed technology for more complex magnetoelectronic systems¹⁶⁷. The unconventional substrate demands a few adaptations in the stack design and preparation process in this case. Since spin valves rely on the exchange bias effect, an antiferromagnetic layer is incorporated in the respective stack. Typically this antiferromagnetic order is induced after the deposition by magnetic field cooling¹¹⁷. This procedure involves heating the entire deposited GMR film to above the Néel temperature of the used antiferromagnet and subsequent cooling back to room temperature in the presence of a homogeneous magnetic field. The applied field sets the direction of the antiparallel spins in the antiferromagnet and thus defines the pinning direction of the adjacent ferromagnetic layer by means of exchange bias. Since the Néel temperature for most antiferromagnetic films is too large for elastomeric substrates, this method cannot be used. In this work, radio frequency (RF) sputtered $\text{Ir}_{19}\text{Mn}_{81}$ thin films, having a Néel temperature of about 670 K at the employed thickness, are used as the antiferromagnetic layer, which are well-known for this purpose^{168,169}. In order to induce the exchange bias without field cooling, two permanent magnets were mounted below the sample holder to provide a static in-plane magnetic field of ≈ 1 kOe on the substrate surface during the whole deposition¹⁶⁷. This field is able to induce the magnetic order in the growing IrMn layer at room temperature, provided that it is deposited directly onto an already existing ferromagnetic layer¹⁶⁸. Therefore, a top-pinned spin valve design, as illustrated in figure 3.6b, was chosen for the preparation onto the soft substrates, where the ferromagnetic sensing layer (free layer) lies underneath the antiferromagnetic film.

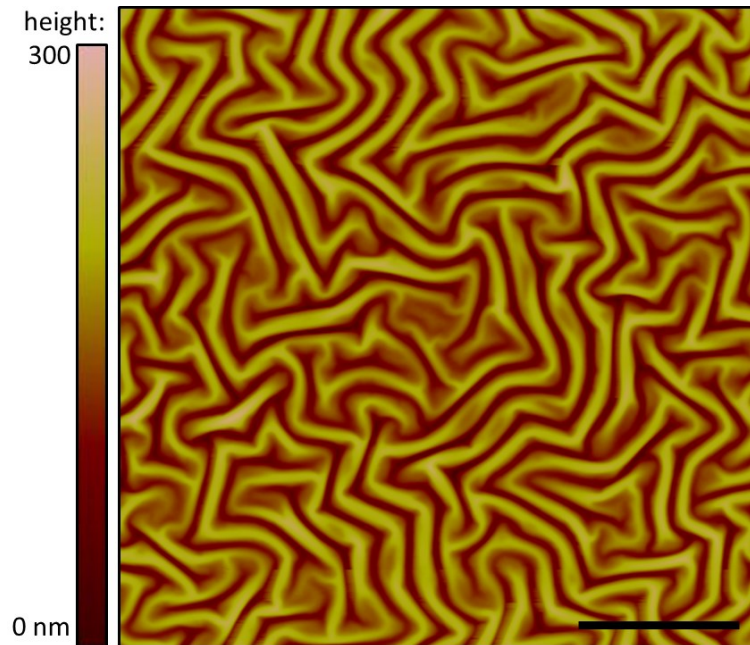


Figure 3.7 | Built-in stress in the Ta seed layer on PDMS: AFM micrograph of the 4 nm Ta film used as seed layer for the spin valves deposited onto the prepared PDMS substrate (scale bar: 5 μm). AFM measurement was performed in collaboration with Barbara Eichler (IFW Dresden). Figure is taken from [167].

The complete layer sequence for the spin valve studied in this work is:

Ta(2)/Ir₁₉Mn₈₁(5)/[Ni₈₁Fe₁₉(4)/Co₉₀Fe₁₀(1)]/Cu(1.8)/[Co₉₀Fe₁₀(1)/Ni₈₁Fe₁₉(4)]/Ta(4).

The 4 nm Ta seed layer grows with a large built-in stress, which is evidenced by an AFM measurement shown in **figure 3.7**. Since the metal is deposited onto a soft PDMS surface, the compressive stress is able to relax by forming an extended *random wrinkle pattern* with a characteristic period of $\lambda_{\text{Ta}} = 800$ nm. From the AFM data the areal expansion of the Ta buffer layer upon deposition was extracted to be 6.6%. Hence, the subsequently deposited layers are grown onto this randomly wrinkled surface. An AFM investigation of the final spin valve morphology is included in the results chapter (figure 4.12a,b) together with a discussion of its influence on the stretchability and magnetoelectronic properties.

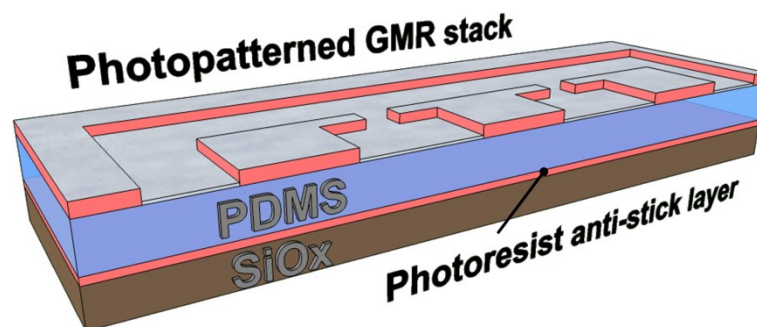


Figure 3.8 | Sample after deposition: A sketch of the pre-final sample structure after the deposition of a GMR nanomembrane onto the lithographically processed PDMS surface. Figure taken from [6].

The sensor samples after the deposition of GMR thin films onto the prepared substrates, as they are illustrated in **figure 3.8**, have to be lifted with acetone in order to finalize the lithographic patterning process. Dipping the specimen into the solvent would result in a strong swelling of the PDMS film causing the thin magnetic nanomembrane on top to crack and be destroyed within a few seconds. Instead, careful rinsing in acetone interrupted by drying with a nitrogen gun is necessary. Several iterations of rinsing and drying are performed in order to completely strip the parts deposited onto the developed photoresist and reveal the final sensor structure. Besides the spin coating of the photoresist onto PDMS this is the most delicate part of the sample preparation. The final preparation steps, *e.g.* the peeling of the PDMS film from the handling wafer to receive the GMR film on free-standing rubber membranes, are described in the respective results sections (4.1.1 and 4.2.1).

3.1.6 Mechanically induced pre-strain

For the fabrication of stretchable GMR elements, the generation of pre-strain in the elastomeric substrates is a key aspect. Besides thermal treatments, the mechanical induction of high strains by stretching is applied. In the case of uniaxial pre-strain, this could be done in a controlled way using a conventional vernier caliper, as shown in **figure 3.9a**. In order to allow also the generation of high biaxial pre-strain, a self-made holding frame was used, in which an elastomeric film could be stretched and fixed by four binder clips (**figure 3.9b**). The holding frame had to be designed in a way, that it completely fits into the available oxygen plasma chamber (Femto VA, Diener) to perform plasma activation of a PDMS film in the pre-stretched state.

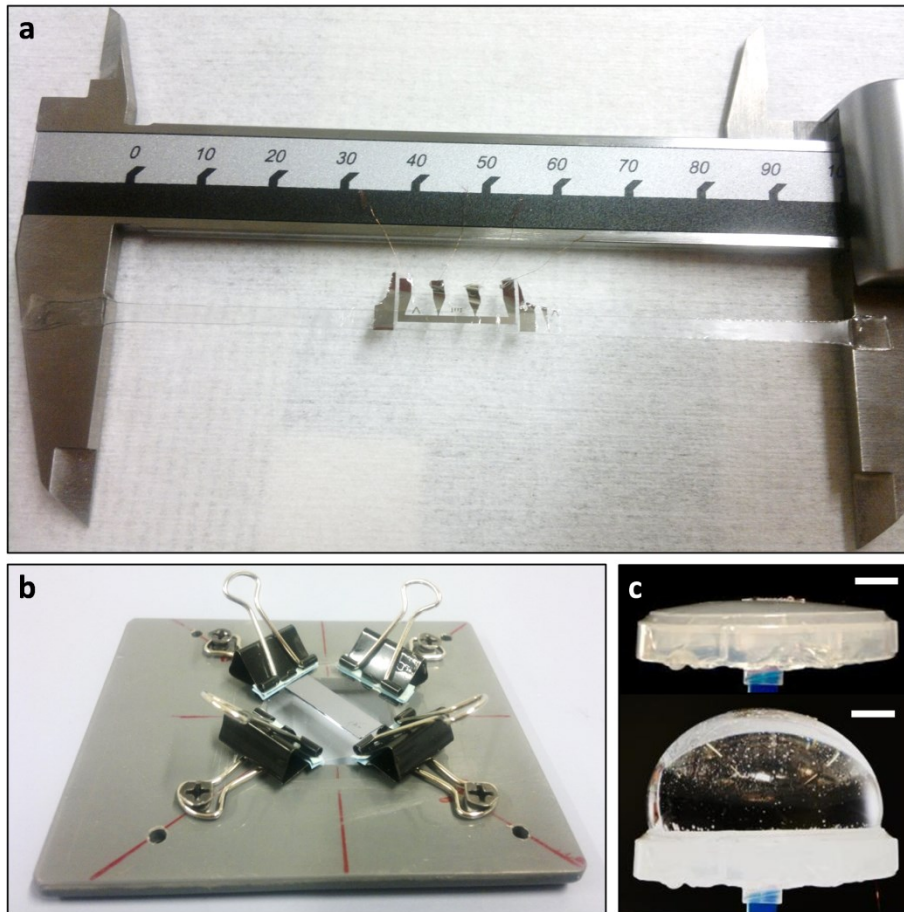


Figure 3.9 | Mechanical pre-strain fixtures: Photographs of uniaxially (a) and biaxially (b) pre-stretched rubber films in their respective fixtures used in this work. The frame and clamps shown in (b) fit into the oxygen plasma chamber for plasma activation of the pre-stretched substrate. (c) Expanding diaphragm apparatus designed for the controlled dynamic application of biaxial pre-strain to a rubber membrane (top: relaxed state, bottom: expanded state, scale bars: 10 mm). The fabrication and photography of the apparatus in (c) was done in collaboration with Daniil and Dmitriy Karanushenko (both IFW Dresden). Figure partially compiled from [7,163].

An alternative approach to generate large biaxial pre-strains relies on a sealed rubber film being inflated as a diaphragm, as shown in figure 3.9c. Therefore, a $50 \times 50 \text{ mm}^2$ piece of VHB™ 4905 F viscoelastic double side adhesive tape (from 3M) is spanned over the circular edge of a plastic tray (55 mm diameter) and sealed to create a waterproof chamber. A fluidic tubing is connected to the back end of the tray to be able to flood the chamber with water through an inlet and expand the stretchable VHB membrane. The injection of water into the supply tubing is done manually using a syringe. This apparatus also allows a controlled dynamic application of biaxial pre-strain to a stretchable sensor mounted on top of the diaphragm. The areal strain applied at this central position of the stretchable membrane is estimated using side-view photographs (shown in figure 4.30d) as follows: From the ratio of lengths of the meridian (along the photographic plane) on the inflated membrane surface l_m and the distance of its two fixed edge points (*i.e.* the diameter of the plastic tray edge) l_d one can retrieve the total strain of the diaphragm along this meridian. Assuming rotational symmetry of tensile

strains in the diaphragm around its axis¹⁸, the respective areal strain at the top point, according to (2.8), is given by $(l_m/l_d)^2 - 1$. This value is associated with the amount of water inside the expanding chamber, which is controlled by the scale on the pumping syringe. The diaphragm apparatus was also integrated into the GMR setup (described in section 3.2.1) to perform *in situ* biaxial deformations for a thorough characterization of the magnetoresistive sensors studied in section 4.4.5.

3.1.7 Methods and materials for the direct transfer of GMR sensors

In this work, besides the direct deposition of GMR films onto elastomeric substrates, other fabrication approaches are applied in order to enhance the compliant properties of magnetoresistive sensor elements. This also involves a specifically developed fabrication process, which is inspired by well-known *transfer printing* techniques¹⁷⁰. Transfer printing has evolved to one of the most promising techniques for the fabrication of stretchable systems^{151,171}. There are a variety of methods united under this notation, however, most of them rely on a micropatterned stamp, usually made of PDMS, that selectively takes up structures of inks, thin films or functional elements weakly bound to a donor substrate and releases them on a receiving surface in a second printing step¹⁵¹. The receiving substrate can be of almost arbitrary kind including flexible, elastic and non-planar membranes. Three of the main modes for transfer printing are demonstrated in **figure 3.10**. Often complex systems are build up on the receiving substrate by successive printing of layers or functional components, which involves a thorough alignment of sequential printing steps to the already printed parts¹⁷².

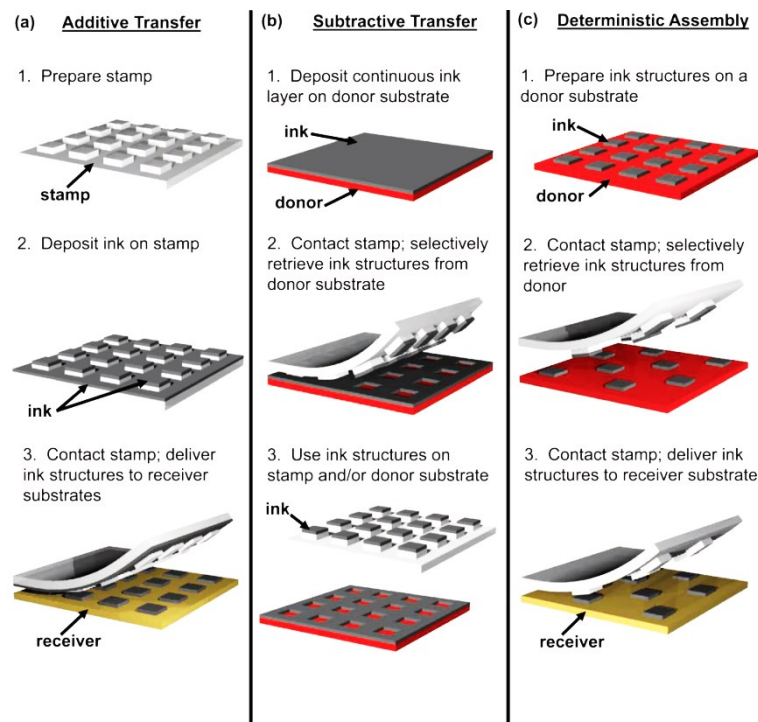


Figure 3.10 | Basic modes for transfer printing: Schematic illustration of (a) additive transfer, (b) subtractive transfer and (c) deterministic transfer. Figure adopted from [151].

The transfer process for magneto-electronic devices developed here represents a significant outcome in the scope of this work. The general description of the procedure is given in the results chapter (section 4.3.1) and only some fabrication details are provided in this section.

The direct transfer is facilitated by a sacrificial layer on the rigid donor substrate, which allows the preparation of advanced GMR sensor systems on its surface. Ca^{2+} metal cross-linked poly(acrylic acid) (PAA) was applied for this purpose¹⁷³. Therefore, PAA of $M_v = 450,000$ g/mol (Sigma–Aldrich Co. LLC) was dissolved to a concentration of 4%(w/v) in deionized (DI) water at 60°C in a shaking incubator for 24 h. The resulting solution was diffusively transparent because of the higher molecular weight fractions of the PAA. These fractions were separated and removed by centrifugation at 3,000 rpm for 2 h in 25 ml tubes. The transparent PAA solution was then spin coated on the surface of Si wafer substrates at 3,500 rpm for 35 seconds, resulting in a film thickness of about 80 nm. After spin coating, the substrate was subjected to cross linking in an aqueous 1 M solution of CaCl_2 (Sigma–Aldrich Co. LLC) with subsequent rinsing in DI water. The prepared substrates were prebaked at 90°C for 5 minutes before the lithographic processing.

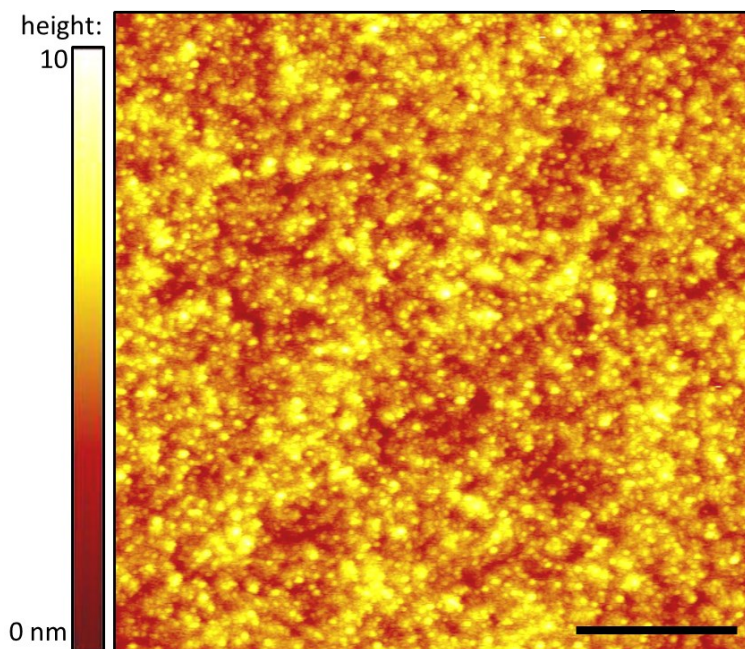


Figure 3.11 | Surface topography of the PAA sacrificial layer: AFM micrograph of the 80 nm Ca^{2+} cross-linked PAA film surface on a silicon wafer, used as sacrificial layer for the transfer of GMR sensor systems. For the shown surface section of $2 \times 2 \mu\text{m}^2$, the value of the root-mean-square roughness is 0.8 nm. (scale bar: 500 nm). PAA films were prepared in collaboration with Daniil Karnaushenko and the AFM measurement was performed in collaboration with Barbara Eichler (both IFW Dresden). Figure is taken from [163].

Figure 3.11 shows an AFM investigation of the bare PAA sacrificial layer surface. Its inert properties and low roughness of only 0.8 nm renders possible the fabrication of micro sized GMR layer systems with multiple lithographic patterning steps. This eliminates the need for certain adaptations necessary on

the delicate PDMS surface, as described in section 3.1.3, and allows using standardized procedures. For the preparation of microsensor arrays, electrode structures were patterned in a second photolithographic step using a mask aligner (MJB4, Karl Suss). Cr(5)/Cu(50) was used as the contacting materials that were deposited by e-beam evaporation (all thicknesses are given in nm).

3.1.8 Materials used for imperceptible GMR sensors

A further substrate that is used for the preparation of compliant GMR sensor elements are ultrathin, 1.4 μm polyethylene terephthalate (PET) membranes. This foil is commodity scale and commercially available (Mylar® 1.4 CW02, Pütz GMBH + Co. Folien KG) and was kindly provided by Martin Kaltenbrunner (Univ. of Tokyo/JKU Linz). It is temporally self-adhered to a reusable, 125 μm thick polymer handling support coated with a thin layer of PDMS. Van-der-Waals adhesion allows for both, device handling during lab-scale fabrication processes and subsequent detachment and transfer of the final element to other substrates and surfaces. The PET foil is fully compatible with the standard lithography and lift-off processes, which allows for accurately patterned individual devices, yet large area low-cost manufacture. The 1.4 μm -PET-foil exhibits a rough surface (29 nm root mean square roughness over the displayed area of 40 x 40 mm^2) as evidenced by an AFM measurement presented in **figure 3.12**. Although such a high roughness tends to significantly suppress the occurrence of the GMR effect especially in multilayers due to magnetostatic orange peel coupling, functional GMR elements facilitating high GMR ratios could be deposited onto this substrate material, as presented in section 4.4.1.

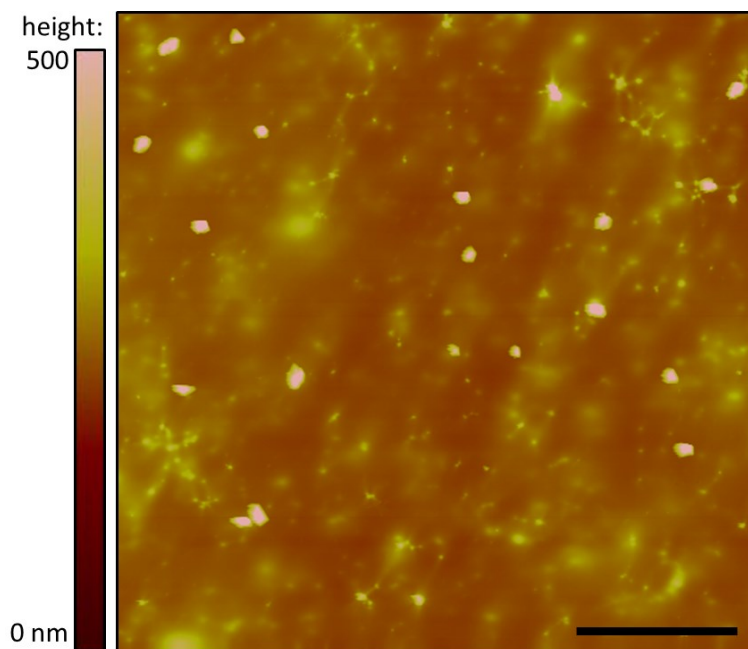


Figure 3.12 | Surface topography of the ultrathin PET foil: (a) AFM image of the PET surface revealing a root mean square roughness of 29 nm throughout the entire scan area of 40 x 40 μm^2 . (scale bar: 10 μm). AFM measurement was performed in collaboration with Barbara Eichler (IFW Dresden). Figure is taken from [7].

Since the stretchability of the PDMS elastomer is limited to about 100%, an alternative rubber material is used for the preparation of highly stretchable GMR sensors. VHB™ 4905 F is a commercially available double sided adhesive tape with a very high stretchability exceeding 1,000%⁷⁶. VHB is an optically transparent, very soft acrylic and exhibits highly viscoelastic properties. In research, it is well-known for the preparation of dielectric elastomer actuators and soft robotics^{39,174}. The product used in this study (section 4.4.4) is a roll of 50 mm width and a thickness of 0.5 mm.

3.2 Characterization

The most important setup for the evaluation of stretchable GMR sensor elements is a stage for magnetolectrical characterization, which features the possibility to also automatically measure samples that are stretched *in situ* on demand in a controlled manner. First, the working principle of the experimental setup is explained and the characterization procedures are defined in this subchapter. A further focus lies in a description of the experiences for a reliable electrical contacting of stretchable sensor devices, as this is a key aspect for their successful characterization. Other experimental methods that are used to obtain relevant information about the microscopic sample structure are also introduced.

3.2.1 GMR characterization setup with *in situ* stretching capability

The magnetolectrical characterization of the prepared sensor elements was conducted in a GMR measurement setup. It performs on-line four-probe resistance measurements on the sample located between the pole shoes of a water cooled electromagnet while sweeping the magnetic field. The setup is fully computer controlled and features a feed-back based control of the magnetic field strength upon sweeping. For a GMR measurement, the field is applied in the sample plane along its stripe geometry starting with the maximum value of a defined field range. The sample resistance is recorded on the control PC for a double sweep back and forth through this range in order to include occurring hysteresis effects of the magnetoresistance. For each resistance measurement, the magnetic field is stabilized by the automated feedback routine using the signal from a reference Hall probe. The obtained data is translated into the characteristic GMR curves using equation 2.3.

In order to evaluate the performance of the stretchable GMR sensors with respect to tensile deformations, a motorized *in situ* stretching module for the existing GMR characterization setup (**figure 3.13a**) was designed and constructed in collaboration with the research technology department of the IFW Dresden. It allows applying defined tensile strains on a sample, which is mounted inside the electromagnet using two clamps. Hence, GMR curves can be recorded while the specimen is in a stretched state. The stretching module also features a measurement of the applied force, which was used as a supervision parameter to exclude that the sample was loosening from or creeping out of the mounting clamps during the experiment. A schematic sketch of the setup with *in situ* stretching

capabilities is displayed in figure 3.13b, including the identifiers of the used commercial periphery electronic modules.

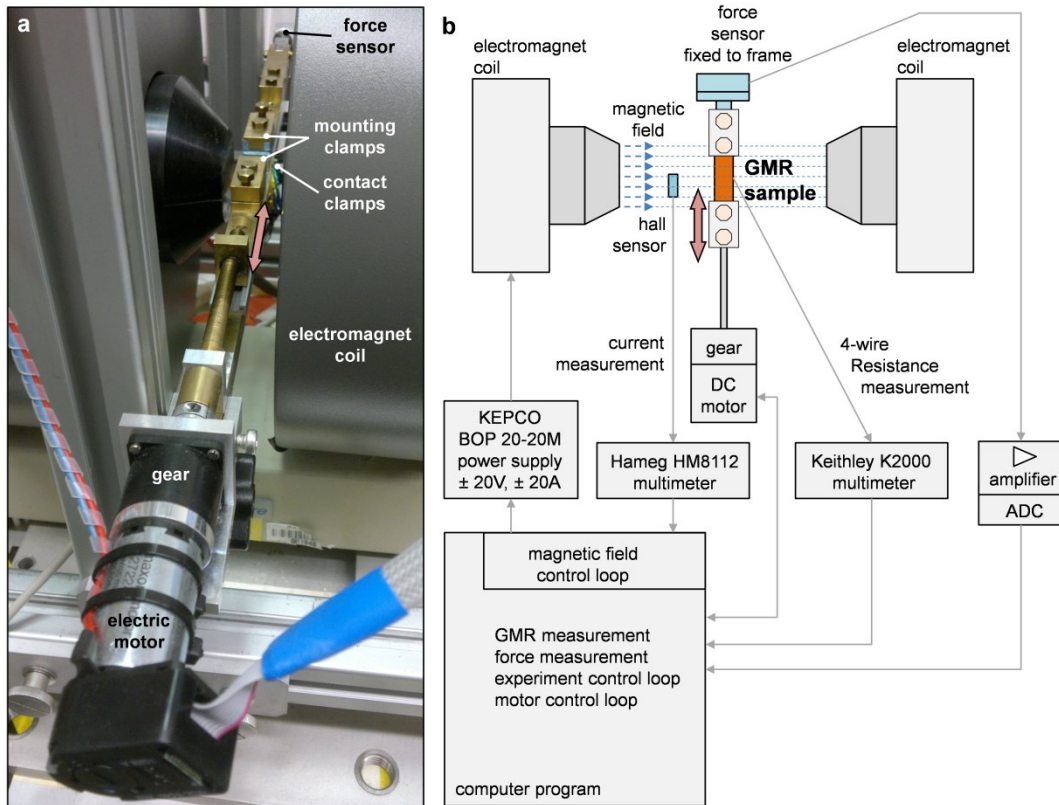


Figure 3.13 | GMR characterization setup with *in situ* stretching capability: (a) The specifically designed *in situ* stretching module mounted inside the electromagnet of the GMR characterization setup. (b) Schematic sketch of the computer controlled setup with periphery electronics (image provided by Torsten Seidemann). The stretching module and control software was designed and constructed in collaboration with the research technology department (IFW Dresden). Figure compiled from [7].

The software of the setup was adapted to implement the electric motor control for automated measurement processes. Two characterization procedures were used in this work. For the first one, the sample is stretched by a defined amount with a rate of $100 \mu\text{m/s}$ before a GMR curve is recorded and stretching proceeds. This alternation is repeated until the electrical contact is lost, which defines the *maximum strain* the sensor can accommodate. In the second procedure, a repeated loading and unloading within a defined strain interval is performed with a rate of $150 \mu\text{m/s}$ and 1 second delay at the reversal points (*cyclic loading*). After a defined number of loading cycles, a GMR curve is recorded at the lowest and highest strain level of the interval, respectively, before cycling proceeds. This procedure should reveal the long-term behavior of the prepared sensors under dynamic mechanical impact. In both cases, initial GMR curves are recorded and a delay time of 30 seconds between stretching and GMR measurement is included to minimize resistance drifts. In the stretching experiments, the magnetic field was applied along the short axis of the patterned sample stripes.

3.2.2 Sample mounting

The mounting of the elastic samples between the clamps of the stretching module is critical for an accurate determination of the sensor deformation. Especially for small applied strains, the establishment of the initial state associated with zero strain is very important. Therefore, a 3 mm x 5 mm x 50 mm bar piece of PDMS (thickness/width/length) is fixed between two mounting clamps and pre-stretched by about 20%. The actual GMR sample is then attached on top of this elastic holding bar (**figure 3.14a**). The PDMS bar was prepared by mold casting onto a clean polished Si wafer, therefore featuring a very smooth surface. This provides a good van-der-Waals adhesion to the sample. This method ensures on the one hand that there is minimal strain on the sample at the initial state and on the other hand that there is no slack as well and the sample is indeed stretched as soon as the separation of the clamps is increased. It was checked that the strain applied to the holding bar is completely transferred to the corrugated GMR multilayer films in this piggyback configuration. High resolution optical microscopic imaging was applied to determine the actual strain on a test sample in a calibration measurement. Figure 3.14b shows the measured strain on the wrinkled GMR film ε versus the strain applied to holding bar $\varepsilon_{\text{appl}}$. The dependence is close to linearity and in good agreement with a slope equal to one, proving the strain being completely transferred to the investigated sample in the measured range of up to 40%.

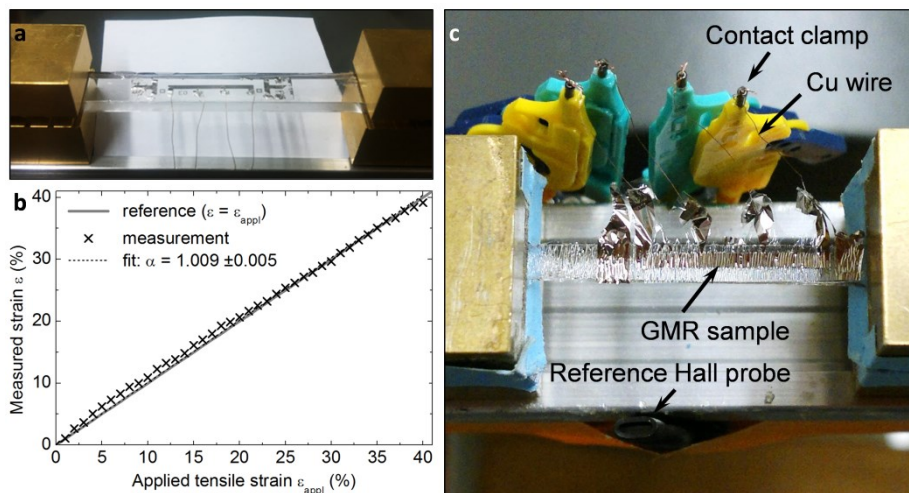


Figure 3.14 | Sample mounting in the linear stretching module: (a) Stretchable GMR sensors mounted and contacted on a pre-stretched PDMS holding bar for defined stretching. (b) Calibration between applied and measured strain in the piggyback configuration shown in (a). The linear fit (dashed line) reveals a slope very close to unity (gray line). (c) Highly stretchable GMR sensor on VHB directly mounted to the clamps of the stretching module. The image also shows the four contact clamps and the reference Hall probe used for the experiments. Figure partially compiled from [167].

For higher strains, the GMR sensors tend to peel away from the holding bar. Samples with higher stretchabilities (*i.e.* those prepared on VHB instead of PDMS) are directly mounted between two holding clamps and their separation was adapted until the slack was removed, as shown in

figure 3.14c. The absolute inaccuracy of the initial zero strain state ($\pm \approx 0.1$ mm for an initial clamp distance of >10 mm) is negligible for applied strains exceeding 100%. In order to characterize sensors under biaxial stretching, the diaphragm apparatus shown in figure 3.9c with a sample attached to the center of the expandable VHB membrane is introduced between the pole shoes of the electromagnet instead of the linear stretching module. Two probe resistance measurements are used in this case. Since the inflation of the diaphragm was controlled manually using a syringe, the automated measurement procedure could not be used for stretching. The tensile strain is controlled by fixed amounts of water being pumped into the chamber, which are calibrated as discussed in section 3.1.6.

3.2.3 Electrical contacting of stretchable sensor devices

The realization of the reliable interface from the soft functional elements to the rigid parts, like power sources or signal processing units, is a very crucial aspect. Especially in the case of high tensile deformations or repeated loadings, the electrical contact points of wires to the contact pads of the stretchable elements tend to fail much earlier than the occurrence of fatigue of the actual device under investigation¹⁶⁷.

The linear stretching module described above uses four test tips, which are able to firmly contact thin wires, as the interface to the Keithley K2000 multimeter for the four-probe resistance characterization, as shown in figure 3.14c. Different approaches for a reliable contacting of the fabricated GMR sensing elements to $100\ \mu\text{m}$ enameled copper conductors were tested during the progress of this work. While for tensile strains below about 10% it was sufficient to use regular silver paste (Acheson Silver DAG 1415) for contacting the specimen to thin copper wires, the contact tend to become more and more unreliable for higher strains. Tin soldered contacts on a PDMS membrane was found to be possible as well, if the top layer of the GMR stack is a solderable material. The reliability versus stretching, however, was only slightly better than for silver paste contacted samples. The rigid bond created by these methods concentrates applied stresses on its edge, leading to the early failure of the contact. The application of acoustic wedge bonding to decrease the size of the bonds was tested but found to be not appropriate on soft substrates. A variety of soft conductive materials was tested to realize an alternative contact bond, including carbon grease³⁹ (MG Chemicals), conductive epoxy adhesive (Epo-Tek H27D, Epoxy Technology) as well as a currently developed polyaniline based conductive rubber¹⁷⁵. Those attempts, however, were even less successful, because the material's conductivity was either too low or the electrical contact too noisy for reliable GMR measurements.

The method that could successfully be applied for the reliable characterization of highly stretchable GMR sensors even far above 100% strain is the one presented in figure 3.14c. The sample structure was slightly adapted by elongated contact pads (4 mm in total) that reach sideways beyond the stretchable support clamped inside the stretching module (*i.e.* the PDMS holding bar or the VHB tape). These free-standing soft yet not expanding contact pads could easily be contacted with copper wires using conventional conductive silver paste. With this method a reliable four-point

characterization of the functional GMR elements even under numerous loading cycles was achieved for the highly stretchable GMR sensors⁷ described in section 4.4.4.

3.2.4 Customized demonstrator electronics

In order to display the sensor signal in an accessible way for demonstration purposes, an electronic circuit was designed and assembled by Daniil Karnaushenko (IFW Dresden) that could translate the sensor signal onto a linear array of LEDs or process it for a data acquisition on a PC. **Figure 3.15a** shows the circuit diagram of one of a total of four channels of the final circuit as well as a photograph of the assembled board (figure 3.15b). The sensor's response to an applied magnetic field is detected by measuring the changes in its resistance by a two-probe measurement. The sensor supply current, produced by a constant current generator circuit implemented directly on the acquisition device, could be set in a range of 1 to 60 mA using a potentiometer. For the GMR sensor devices in this work the supply current is set to 20 mA. The voltage signal from the sensor is enhanced by a three stage cascade amplifying circuit (Amp. 1-3). The amplification and offset can be manually adjusted to fit to the input range of an analog-to-digital converter (ADC) embedded in a microcontroller unit (MCU) C8051F342 of the acquisition device. The acquired data is processed in the MCU and displayed on a linear array of 8 LEDs or sent to a PC via universal serial bus interface (USB2.0) at a rate of 2,000 measured data points per second. This circuit is used for the demonstration of bias-free in-flow detection of magnetic particles (section 4.1.6) and an on-skin magnetic proximity sensor (section 4.4.3).

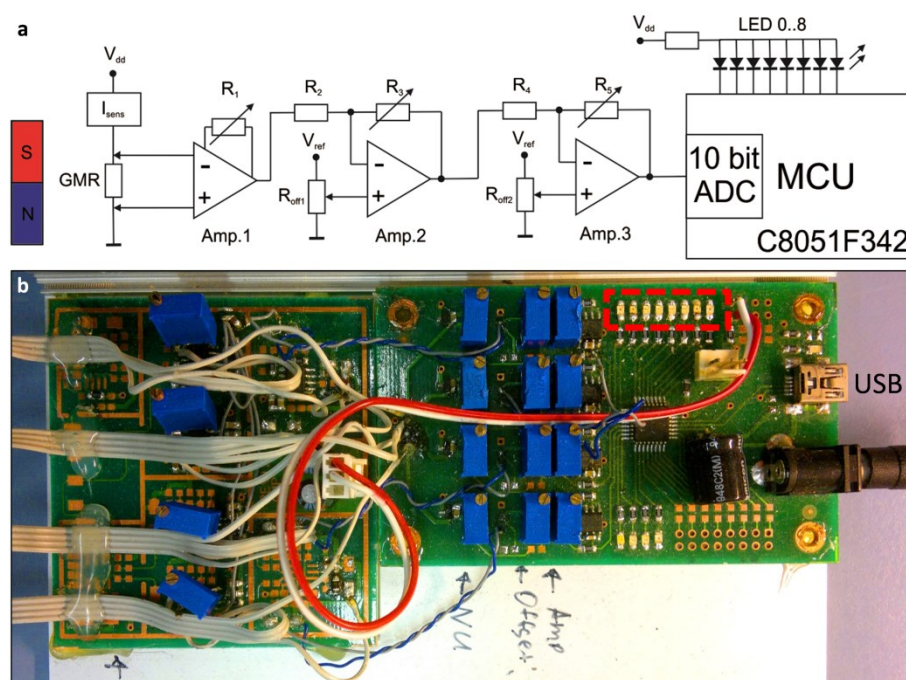


Figure 3.15 | Signal conditioning and amplifying circuit. (a) The circuit diagram of one channel of the self-made acquisition device, connected to a GMR test sample (left), used for demonstration purposes (image provided by Daniil Karnaushenko). (b) Photograph of the entire circuit board, the array of LEDs is highlighted (red dashed frame) and the USB port is labelled. Circuit designed and assembled by Daniil Karnaushenko (IFW Dresden). Figure partially adapted from [7].

3.2.5 Microscopic investigation techniques

Besides regular optical and atomic force microscopy (AFM) other techniques are used throughout this work to obtain relevant microscopic information of the prepared GMR elements. These micrographs reveal structural and morphologic features also during a mechanical deformation of the sensor devices and help to understand their influence on the magnetoelectric responses.

The first method to mention in this respect is confocal microscopy. This type of optical microscope features an extremely narrow focal plane, which is obtained by means of a tiny pinhole aperture in the optical path of the light reflected from the sample. The pinhole cancels light contributions that come from planes on the sample that are not confocal to it. By strongly focusing the incoming light, the detected volume on the specimen can be confined also laterally. In order to get a microscopic picture of the object, 3D scanning is used. The reconstructed data represents a 3D contour replica of the reflective sample surface. The microscope device used in this work is a laser scanning confocal microscope (Keyence VK-X210) featuring a blue laser diode light source ($\lambda_{\text{ex}} = 408 \text{ nm}$). This facilitates a lateral accuracy of $0.2 \mu\text{m}$ and a vertical resolution down to 10 nm . With its touchless 3D imaging capabilities it is a perfect tool for the investigation and measurement of microscopically wrinkled metallic surfaces on soft supports. The one major restriction of this technique is related to a maximum local tilt of the reflective surface, above which the intensity of the light reflected back to the objective is too low for detection. This leads to signal faults at the wrinkle sides if their amplitude to wavelength ratio exceeds a certain value (≈ 0.5 in the case of the smooth metalized surfaces used here).

In some cases it is beneficial to have cross-sectional views of the wrinkled metal films available to reveal buried structural features. For this purpose, focused ion beam (FIB) milling is utilized on an NVision 40 Cross-beam station (Zeiss). It uses a beam of gallium ions, which is electrostatically focused, to locally remove material from a specimen in a high vacuum environment. This can cut trenches with a clean edge of several micrometers depth into almost arbitrary materials. Before cutting, a carbon bar is deposited on the cut edge *in situ* to stabilize the topographic structure of soft materials. The cut edge can be directly investigated by scanning electron microscopy (SEM), under a tilt angle of 54° , which is incorporated in the cross-beam workstation. The tilt corrected images are used as a cross sectional view of the wrinkled magnetoelectronic films in this work to verify layer adhesion or reveal the occurrence and nature of cracks.

4. RESULTS & DISCUSSION

4.1 GMR multilayer structures on PDMS

In order to obtain stretchable magnetoresistive sensors, thin film based GMR layer stacks, which are well-known on conventional substrates, were fabricated on rubber supports. As a first step, the potential of GMR multilayers directly structured and deposited on elastomeric PDMS films will be investigated. The GMR performance and sensitivity are set in relation to similar multilayers on rigid silicon substrates. Several relevant effects and phenomena will be addressed and described, that arise if the magnetic nanomembranes are prepared on *free-standing* PDMS membranes. The potential and versatility of soft magnetic sensor elements for different application fields are demonstrated on a proof-of-concept level. The subchapter closes with the first stretchability tests, and *in situ* GMR characterizations.

4.1.1 Pre-characterization

The preparation of lithographically structured GMR elements on a PDMS film spin coated on a silicon handling wafer equipped with an anti-stick layer is already described in sections 3.1.2 through 3.1.5. To begin with, GMR multilayers of $[\text{Co}/\text{Cu}]_{50}^{1\text{st}}$ investigated as the initial test system. A resultant array of sensor elements is presented in **figure 4.1a**. In order to obtain specimens on free-standing stretchable membranes, the PDMS film was cut and then individual elements were peeled from the rigid silicon wafer, as shown in figure 4.1b. Due to the anti-stick layer underneath, the spin coated PDMS film was gently released upon peeling along the patterned GMR structure without too much expansion. The final samples were free-standing 40 μm thick PDMS rubber membranes coated with photopatterned GMR multilayer structures (figure 4.1c).

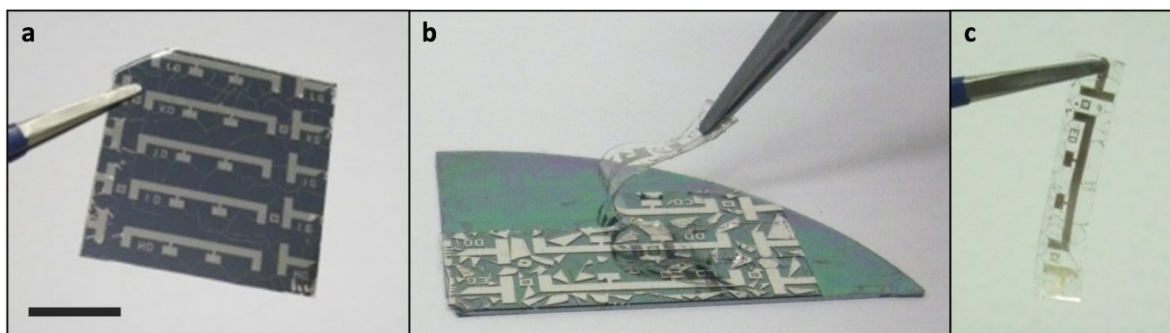


Figure 4.1 | Peeling of GMR multilayers on PDMS from the handling wafer: (a) Array of photopatterned $[\text{Co}/\text{Cu}]_{50}^{1\text{st}}$ multilayers on a PDMS coated silicon wafer (scale bar: 10 mm). (b) Peeling of an individual GMR element from the rigid silicon support by means of the anti-stick layer. (c) Photopatterned $[\text{Co}/\text{Cu}]_{50}^{1\text{st}}$ multilayer element on a free-standing PDMS membrane of 40 μm thickness. Figure taken from [6].

Figure 4.2a shows the GMR ratio measured at room temperature for $[\text{Co}/\text{Cu}]_{50}^{1\text{st}}$ multilayers on different substrates. The GMR curves obtained from samples prepared in the same deposition run on rigid silicon wafer without (SiOx) and with PDMS coating (PDMS/SiOx) are very similar. A

maximum GMR value of more than 50% is obtained on both substrates, which is a typical value for Co/Cu based GMR multilayers¹⁷⁶. Furthermore, the GMR characteristic does not change after the sample is peeled off the silicon wafer (PDMS). Hence, the magnetic sensing capabilities of GMR multilayer elements on free-standing rubber membranes are as good as on conventional rigid silicon substrates⁶. The absolute sensor resistances for the three cases, as given in the caption of figure 4.2, are also found to be very comparable. An explanation for the slightly decreased sensor resistance after peeling will be given in section 4.1.3.

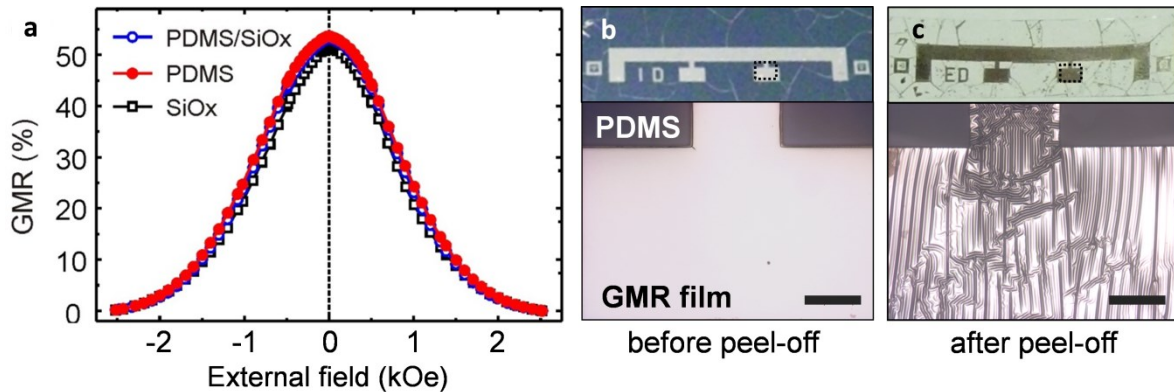


Figure 4.2 | Characterization of GMR multilayers on PDMS: (a) GMR curves of $[\text{Co}/\text{Cu}]_{50}^{\text{st}}$ elements grown on rigid silicon wafer (\blacksquare ; $R_0 = 15.3 \Omega$), PDMS coated silicon wafer (\bullet ; $R_0 = 15.9 \Omega$) and free-standing PDMS membrane (\bullet ; $R_0 = 15.0 \Omega$). Even after the sample is peeled from the SiOx wafer, the GMR performance remains unchanged. (b,c) Photographs (top) of the PDMS/SiOx and PDMS samples, respectively and optical micrographs (bottom) of the sections highlighted by the dashed squares. All scale bars: 200 μm . Figure compiled from [6].

Although the GMR performance of the devices on freestanding PDMS membranes and on PDMS-coated silicon wafers is similar, the morphology of the samples is found to be substantially different. Figure 4.2b,c shows photographs and optical microscopy close-ups of a GMR multilayer on top of the PDMS surface before and after the rubber was released from the rigid substrate. When the rubber film is still attached to the silicon wafer, the metal film is smooth, which indicates low intrinsic stresses during the deposition of the GMR multilayers¹⁰⁰. On the peeled rubber membrane, however, the formation of buckles is observed (bottom of figure 4.2c), which will be explained in detail in the following section.

4.1.2 Thermally induced wrinkling

The observed wrinkling of the GMR layer upon peeling (figure 4.2c) results from the curing of the spin-coated PDMS films at an elevated temperature during its fabrication, as described in chapter 3.1.2. The thermal shrinkage of the cured rubber film upon cooling down is suppressed in the lateral directions by the rigid silicon wafer it is attached to. This suppression is due to a large mismatch of the *thermal expansion coefficients* α of the two materials ($\alpha_{\text{PDMS}} = 9.6 * 10^{-4} \text{ K}^{-1}$ vs. $\alpha_{\text{Si}} = 2.6 * 10^{-6} \text{ K}^{-1}$). As a result, a significant part of the thermal contraction of the rubber is “stored” by means of a compressive lateral stress arising inside the elastic PDMS film. This stress is maintained

during the structuring and sputter deposition of the GMR layers and is not released until the sample is peeled from the rigid supporting wafer. Upon peeling, the rubber laterally contracts which causes wrinkling of the incompressible metal film¹⁴⁷. This feature is referred to as *thermally induced wrinkling*³⁶ throughout this theses. As described in chapter 2.4.3, the formation of wrinkles after metal film deposition onto pre-strained elastic substrates has been exploited previously for compliant electrodes, where stretchability is provided by smoothing out the buckles for lateral strains perpendicular to them²⁷. The thermal contraction along one axis of the PDMS film for the temperature difference of $\Delta T = 70$ K (from 90°C down to room temperature), is about 7%.

Figure 4.3a shows a 3D confocal laser scanning microscopy of a GMR multilayer on a free-standing PDMS membrane. Although the thermally induced pre-strain leads to a laterally isotropic contraction of the rubber film, the wrinkles have a strong preference for a parallel alignment perpendicular to the patterned stripe structure (in figure 4.3a, the sensor stripe lies in the horizontal axis). This is expected, since wrinkles generally tend to align perpendicular to structural defects or the edges of structured films^{24,177}. Furthermore, the specimens are peeled along the stripe structure, which favors the wrinkling perpendicular to it. The aligned wrinkling of the metal film, with the stress being relaxed along the sensor stripe, makes it more stiff in the orthogonal direction¹⁷⁸, which prevents the perpendicular stress relaxation and associated wrinkling in most regions. Instead, a slight bending across the GMR stripe could be observed on the peeled sensor elements.

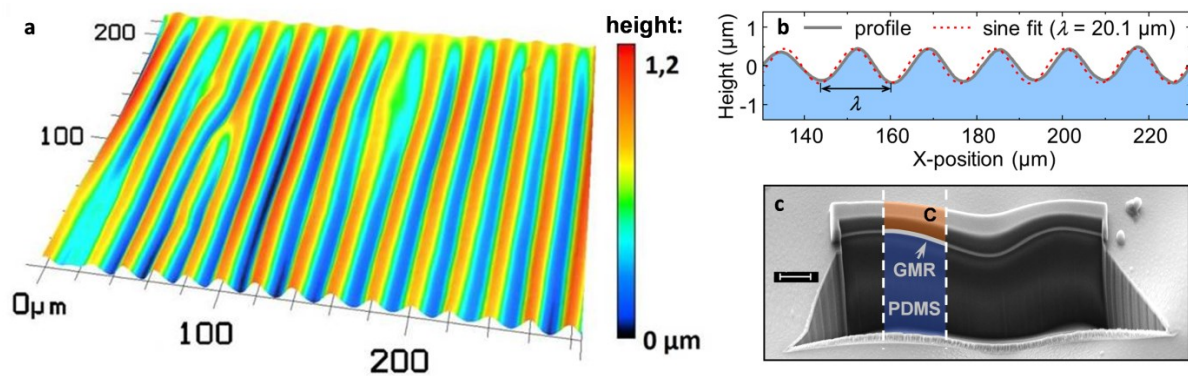


Figure 4.3 | Thermally induced wrinkling on PDMS: Wrinkled topography of GMR multilayer elements prepared on PDMS films after peel-off. **(a)** 3D confocal microscopy image showing the height profile. **(b)** Confocal line scan (gray) and sinusoidal fit (red) providing a mean wrinkle period λ of about 17 μm . **(c)** SEM image of a FIB cut through the sample showing the deposited carbon protective layer for FIB cutting, the $[\text{Co}/\text{Cu}]_{50}^{\text{st}}$ GMR layer and the PDMS substrate (scale bar: 2 μm). FIB milling and SEM investigation was performed in collaboration with Dr. Stefan Baunack (IFW Dresden). Figure partially compiled from [6].

As described in section 2.4.3, wrinkling of hard films on soft membranes exhibits a characteristic wrinkling period, which depends on the mechanical properties of both materials and scales with the film thickness^{24,179}. The height profile of the soft GMR elements reveals a wrinkling period of $\lambda_{\text{exp}} = 20.1$ μm and a mean amplitude of about 0.45 μm (figure 4.3b). A FIB cut of the sample (figure 4.3c) discloses the wavy GMR film (indicated by the gray line) firmly attached to the bulky

rubber (highlighted in blue). This suggests that the contact between the PDMS and the metal film is maintained throughout the wrinkle structure and no delamination occurs. As a result, a theoretical model suggested by Bowden *et al.*²⁴ can be applied to calculate the period of the wrinkles formed for a thin incompressible metal film of thickness d on an elastomeric surface, according to (2.15). The mechanical parameters used for the calculation are as follows: $E_s = 1.6$ MPa, $E_f = 171$ GPa ($E_{Co} \approx 211$ GPa, $E_{Cu} \approx 131$ GPa, weighted by their respective share in the multilayer), $\nu_s = 0.48$, $\nu_f = 0.33$ ($\nu_{Co} = 0.31$, $\nu_{Cu} = 0.35$). The Young's modulus of the PDMS was derived from stress-strain measurements (figure 2.13), while its Poisson's ratio and the data for the metal film are taken from the literature^{24,180}. Considering the total thickness of the GMR multilayer stack ($d = 110$ nm), the calculation predicts a value for the wrinkling period of $\lambda_{theo} \approx 21.7$ μm , which is in good agreement with the experimental value derived from the line scan in figure 4.3b. This critical strain for the occurrence of wrinkling in the investigated system, according to (2.14), is computed to $\varepsilon_c = 0.26\%$.

4.1.3 Self-healing effect

The preparation and particularly the lithographic structuring of GMR multilayer elements directly on the PDMS surface, may result in a cracked metal film, before it is peeled from the handling wafer in some cases. Especially, the photolithographic patterning sometimes causes failure, because the solvents usually used for the lift-off procedure tend to swell the PDMS film, which might tear apart the magnetic nanomembranes on top. **Figure 4.4a** shows GMR curves recorded on a series of prepared stripe elements (left hand inset) prior to the peeling from the rigid handling wafer. The gray dashed line shows the curve of a similar sensor prepared on rigid silicon, which represent the reference GMR characteristic with a magnitude of about 52%. The plotted data demonstrates, that some of the prepared specimens lack performance, which is due to cracks being present in the structure. An optical micrograph of such a cracked specimen is shown in the right hand inset of figure 4.4a. Three cracks running from the top edge of the structure are clearly visible. The damage of the GMR elements is also reflected in the absolute resistance values, which are provided for each specimen in the legend. The elements with poor performance have a much higher resistance compared to the reference sensor prepared on a silicon wafer without PDMS.

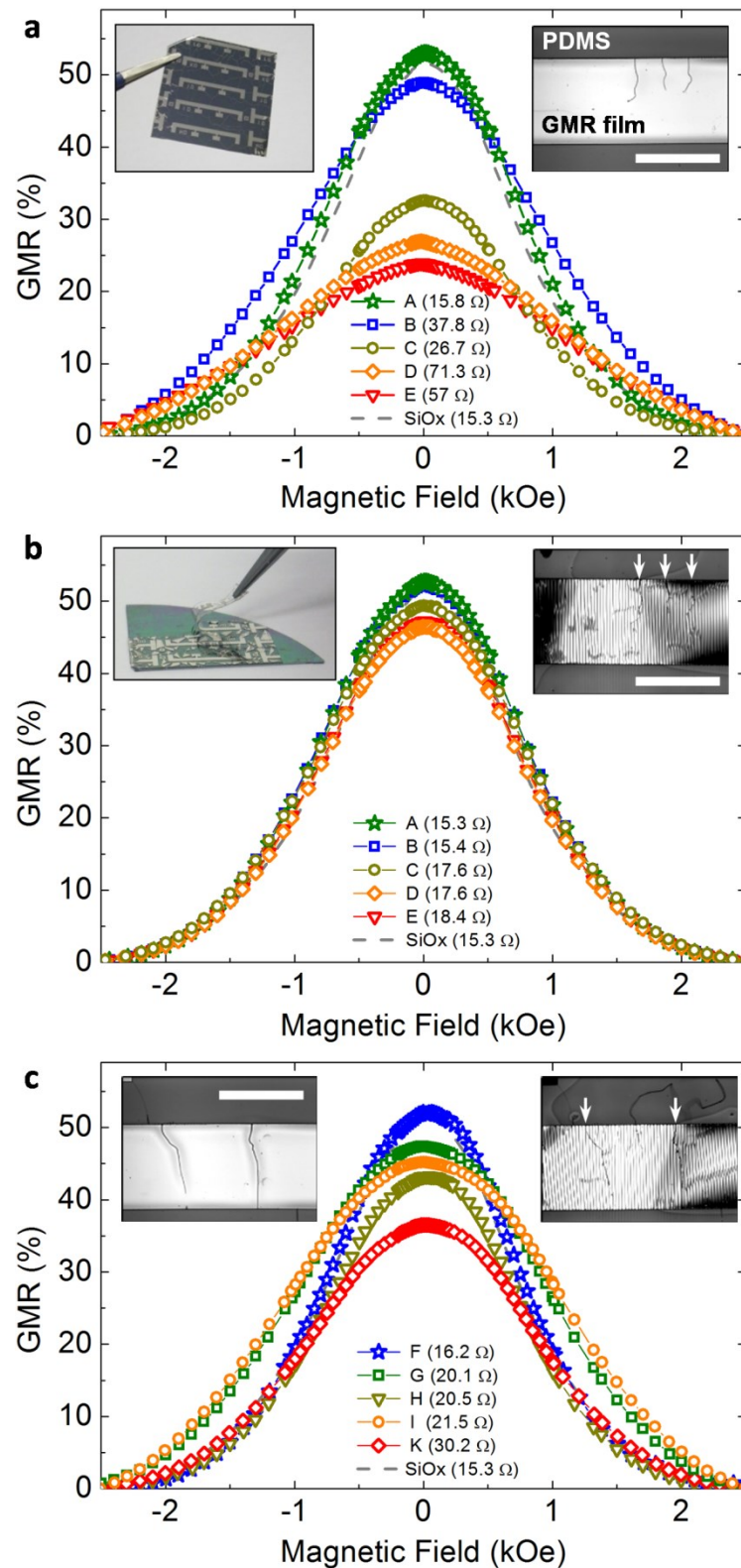


Figure 4.4 | Self-healing of GMR multilayers on PDMS: GMR characterization of $[\text{Co}/\text{Cu}]_{50}^{\text{st}}$ elements (a) before and (b) after peeling from the handling wafer, according to the left hand insets. The insets on the right show respective optical micrographs of a section with cracks. (c) GMR curves of peeled elements that had no electrical contact beforehand. The insets present again a cracked section before (left) and after (right) peeling. Positions of closed cracks after peeling are indicated by white arrows. All scale bars: 1 mm. Figure taken from [145].

The same specimens were characterized again after they were peeled from the handling wafer (figure 4.4b, left hand inset). In this state, the GMR curves are much more comparable and the defected elements recovered to or almost to their full performance. In this respect the GMR multilayers on the elastomeric substrate undergo a *self-healing effect*¹⁴⁵ as they are peeled from their rigid support. The thermally induced wrinkling of the GMR nanomembranes due to the contraction of the PDMS is clearly visible in the right hand inset. This micrograph shows the same section of the corresponding specimen, as in the right hand inset of figure 4.4a. Besides wrinkling, the contraction of the PDMS membrane influences also the cracks by closing them and eventually restoring the electrical conduction across to heal the GMR film. The positions of the three cracks are indicated by the three white arrows on the top edge of the stripe structure. The recovery of the electrical contact across the cracks is also indicated by the reduced absolute resistance values of the healed sensing elements given in the legend. After peeling they are well comparable with the reference value given by the element on the silicon wafer. It is noteworthy, that the closed cracks shown in the right hand inset of figure 4.4b are not increased in length, which proves the gentle detachment of the soft elements during peeling, without overstretching them. The GMR curves presented in figure 4.4c are obtained from sensor elements, which showed no electrical conduction before peeling. Hence, even if cracks run all the way through the structure, preventing the flow of current between the contact pads in the initial state, their functionality can be recovered after peeling, as shown in the insets. Some sensors even show the full sensing performance compared to the reference specimen on silicon wafer (compare blue stars versus the gray dashed line).

The described self-healing effect is a unique feature of the elastomeric substrate, since it requires an induced pre-strain that accounts for a contraction of the support after the preparation of the sensor devices. Furthermore, its appearance is not restricted to magnetic nanomembranes, but may be observed also with other thin film structures. Despite the apparent effectiveness of the self-healing, it has to be clearly stated, that the GMR elements recovered by this means do not exhibit a significant stretchability. Although the electrical contact may be maintained for strains below the thermally induced pre-strain, *i.e.* before the cracks open up completely upon stretching, the signal is usually very noisy due to the unstable conduction across the joint cracks and therefore inappropriate. However, they can be used for sensing on curved but rigid surfaces, where dynamic deformations are suppressed.

A respective demonstrator showing the functionality of a prepared GMR sensor in a non-planar configuration is introduced in the next section. Additionally, an encapsulation layer (*e.g.* of PDMS¹⁸¹ or parylene¹⁶) may help to stabilize the restored contacts across the cracks during moderate deformations. In conclusion, the self-healed sensors complement the choice of already available flexible magnetic sensing elements prepared on flexible plastic membranes and relying on GMR^{4,103,104} as well as on tunnel magnetoresistance (TMR) effects⁵ or even printed GMR elements on paper^{182,183}.

This flexibility offers novel applications and advantages in detection, which are not achievable by rigid magneto-electronic elements^{166,182}.

4.1.4 Demonstrator: Magnetic detection on a curved surface

The prepared GMR elements on free-standing rubber membranes are thin and can easily conform to non-planar surfaces, which makes them interesting components for magnetic field measurements in curved geometries or confined environments. To demonstrate the application potential of the soft GMR sensor element on a proof-of-concept level, the simple setup shown in **figure 4.5a** was assembled. One soft GMR sample was attached to a plastic foil shaped into a ring geometry to track the magnetic field of a rotating permanent magnet. The change in resistance of the GMR multilayer was recorded versus time. When the magnet passes the GMR sensor, a clear decrease of the sample resistance is detected (figure 4.5, right panels). The dynamic response is illustrated by sensing the rotating magnetic field at a higher frequency, which is easily traced with the GMR sensor (figure 4.5c). This setting resamples, in a simple way, the geometry of common rotating electrical machines. In this respect, the regarded GMR sensor may be used as a rotational speed gauge or angular encoder, which can directly be integrated into the curved and narrow air gap between rotor and stator. This proof-of-concept has inspired the development of thin and flexible bismuth based Hall sensorics¹⁸⁴, which have a high potential for applications in electrical machines, especially for significant improvements of magnetically suspended systems¹⁸⁵. A brief review on the preparation and sensing performance of Bi Hall probes, which were pursued in collaboration with colleagues from the IFW and TU Dresden¹⁸⁶, as well as an explanation of their benefits for electrical machines, will be given at the very end of this work (subchapter 5.3).

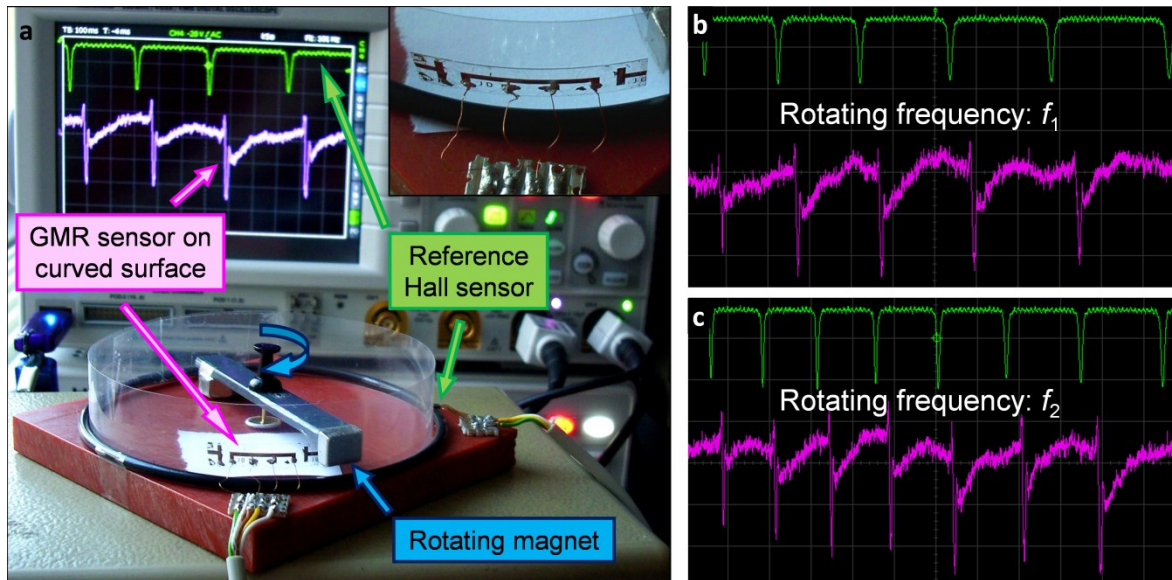


Figure 4.5 | Demonstrator for non-planar geometries: (a) Detection of a rotating magnet using a soft GMR sensor attached to the curved surface of a plastic foil (inset). When the magnet approaches the GMR sensor, a decrease of the sample resistance is observed by spikes in an oscilloscope signal (purple curve). The green curve represents the reference signal taken by a conventional Hall effect sensor. The signal from the GMR and Hall effect sensor are phase-shifted due to the different spatial position of both sensor elements. (b,c) Response of the GMR sensor to the rotating magnetic field with different frequencies ($f_1 < f_2$). The increase of the rotation frequency of the permanent magnet can be easily traced with the GMR sensor. This experiment was conducted in collaboration with Daniil Karnaushenko (IFW Dresden). Figure taken from [6].

4.1.5 Sensitivity enhancement

The magnetoresistive layer stack investigated in the previous chapters was relying on Co/Cu multilayers which are coupled in the 1st AFCM (*i.e.* $[\text{Co}/\text{Cu}]_{50}^{\text{1st}}$). This system is optimized in order to obtain a maximum GMR ratio and exhibits a saturation field of about 2.5 kOe (figure 4.2a). The respective GMR characteristic makes it a good choice to use as sensing elements for magnetic fields in the range of 1 kOe. However, different applications demand different sensing capabilities that require specific features of the sensor response, like a linear characteristic or a high sensitivity to low magnetic field strengths. One example is the application of magnetic sensors in medical diagnostics or bio-analytic systems¹⁸⁷⁻¹⁹⁰, which demands the reliable detection of magnetic field in the range of 10 Oe and below.

In order to demonstrate the potential of the presented compliant magnetic sensor platform for a wider field of applications, different systems of GMR multilayers are prepared on free-standing elastomer membranes, highlighting their unique magnetoelectric properties¹⁶⁶. A total number of four multilayer stacks are fabricated, compared and used on demand in this work: apart from the $[\text{Co}/\text{Cu}]_{50}^{\text{1st}}$ stack already introduced above, these are $[\text{Py}/\text{Cu}]_{50}^{\text{1st}}$, $[\text{Co}/\text{Cu}]_{30}^{\text{2nd}}$ and $[\text{Py}/\text{Cu}]_{30}^{\text{2nd}}$ according to the composition given in chapter 3.1.5. The adaption of GMR multilayer stack includes two approaches to enhance the sensitivity to external magnetic fields, which are approved for rigid substrates⁹⁵. On the one hand, the magnetically softer permalloy, that shows a different switching behavior due to its reduced coercivity, is used as the FM layers in $[\text{Py}/\text{Cu}]_{50}^{\text{1st}}$. On the other hand, the magnetic layers in

the multilayer stack are coupled in the 2nd AFCM by increasing the thickness of the NM spacer layers in $[\text{Co}/\text{Cu}]_{30}^{2\text{nd}}$. As discussed in chapter 2.2.3, this leads to a weaker interlayer exchange coupling between the FM layers. According to (2.4), the sensitivity is related to the slope of the GMR characteristic. Both modifications allow the magnetic moments in the multilayers to align (*i.e.* the resistance to drop) at lower magnetic fields. The $[\text{Py}/\text{Cu}]_{30}^{2\text{nd}}$ stack represents a combination of both approaches by preparing a Py/Cu multilayer coupled in the 2nd AFCM. As for the GMR elements presented in the previous chapters, the multilayers were lithographically structured on a PDMS film with thermally induced pre-strain and then peeled from the carrying wafer after preparation.

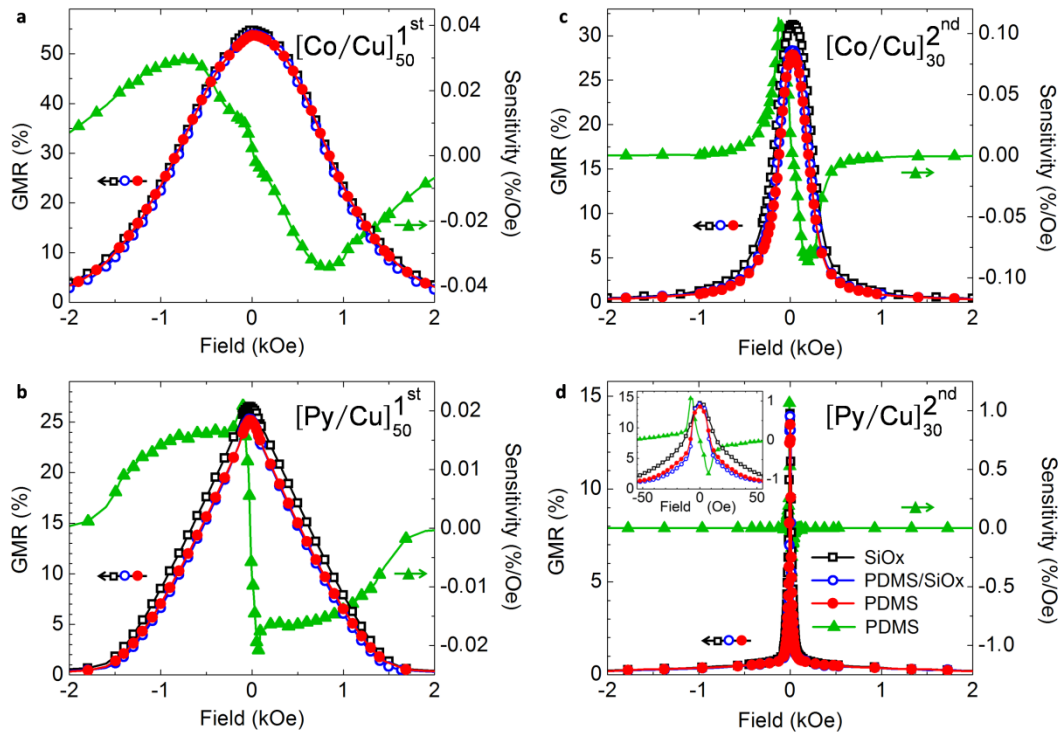


Figure 4.6 | GMR multilayers with enhanced sensitivity on PDMS: Magnetoelectric characterization of the four investigated GMR multilayer stacks: (a) $[\text{Co}/\text{Cu}]_{50}^{1\text{st}}$, (b) $[\text{Py}/\text{Cu}]_{50}^{1\text{st}}$, (c) $[\text{Co}/\text{Cu}]_{30}^{2\text{nd}}$ and (d) $[\text{Py}/\text{Cu}]_{30}^{2\text{nd}}$. The GMR sensors are fabricated on different substrates: rigid SiOx wafer (\blacksquare), PDMS coated SiOx wafer (\bullet) and free-standing PDMS membrane (\blacktriangle). The field dependent sensitivity of the GMR sensors on free-standing PDMS membranes is also shown (\blacktriangle). The inset in (d) shows the same data zoomed in the low field range for better distinction. Figure taken from [166].

For a comparison of their specific sensing capabilities, the four multilayer systems were characterized at room temperature, as shown in **figure 4.6**. Each layer stack was measured on the PDMS film before and after peeling and on a rigid SiOx wafer as a reference. In all four cases, the multilayer elements reveal a similar GMR performance on the elastomeric substrates, as on the rigid reference samples. As in the case of $[\text{Co}/\text{Cu}]_{50}^{1\text{st}}$, also the thermally induced wrinkling that occurs when the PDMS membranes are peeled has little influence on the GMR characteristic in the other three multilayer systems, which proves the applied fabrication technology suitable for a variety of magnetoresistive

sensing elements. The data also includes the magnetic field dependent sensitivity of the different GMR multilayers derived from the measurements on free-standing PDMS membranes.

Compared to the $[\text{Co}/\text{Cu}]_{50}^{1\text{st}}$ model system (figure 4.6a) the magnetically softer Py layers do not lead to an overall increased sensitivity, whereas the magnitude of the GMR ratio is only half as large (figure 4.6b). However, the sensitivity maximum is shifted to the low field range (*i.e.* from about 800 Oe in (a) to 80 Oe in (b)) and the GMR characteristic becomes linear. Therefore, this layer system would be well suited for proximity sensors detecting the distance to a permanent magnet, which typically generates fields of about 1 kOe in close vicinity. The $[\text{Co}/\text{Cu}]_{30}^{2\text{nd}}$ multilayer coupled in the 2nd AFCM results in a narrow response curve without losing as much of the GMR effect (figure 4.6c), giving it an increased sensitivity compared to the multilayers prepared in the 1st AFCM. This system should be chosen, if a high signal for moderate fields up to 500 Oe is needed. The GMR curves obtained for the $[\text{Py}/\text{Cu}]_{30}^{2\text{nd}}$ multilayer are very narrow with a saturation field of about 50 Oe and exhibit a considerable resistance change of more than 13% (figure 4.6d). The sensitivity of these elements on free-standing PDMS reaches a remarkable value of 1.06 %/Oe, which is almost 30 times larger than for the $[\text{Co}/\text{Cu}]_{50}^{1\text{st}}$ samples. Also, the maximum of the sensitivity is at very low fields of only 8 Oe, making it the system of choice for the detection of small or weak magnetic objects¹⁶⁶, for example microscopic magnetic particles as they are used in biotechnology and medical applications^{191,192}. A unique feature that can be added by soft magnetoresistive sensors in this respect will be introduced in the next paragraph. Table 4.1 summarizes the key parameters of the four GMR multilayer systems investigated in this study. The GMR sensor response can be further adapted to specific applications by altering its shape, by means of magnetic shape anisotropy¹¹¹ or adjusting its size to the objects that should be detected.

Table 4.1 | Key parameters of GMR multilayers deposited on PDMS: Denotation, layer stack, GMR magnitude, maximum sensitivity and field of highest sensitivity for the four investigated GMR multilayer stacks, according to the data presented in figure 4.6.

Denotation:	$[\text{Co}/\text{Cu}]_{50}^{1\text{st}}$	$[\text{Py}/\text{Cu}]_{50}^{1\text{st}}$	$[\text{Co}/\text{Cu}]_{30}^{2\text{nd}}$	$[\text{Py}/\text{Cu}]_{30}^{2\text{nd}}$
Panel in figure 4.6:	a	b	c	d
Layer stack:	Co(1 nm)/ [Co(1 nm)/ Cu(1.2 nm)] ₅₀	Ni ₈₁ Fe ₁₉ (1.9 nm)/ [Ni ₈₁ Fe ₁₉ (1.9 nm)/ Cu(0.9 nm)] ₅₀	Co(1 nm)/ [Co(1 nm)/ Cu(2.2 nm)] ₃₀	Ni ₈₁ Fe ₁₉ (1.5 nm)/ [Ni ₈₁ Fe ₁₉ (1.5 nm)/ Cu(2.3 nm)] ₃₀
GMR magnitude				
on SiOx:	54.7%	26.5%	31.3%	14.1%
on SiOx/PDMS:	54%	25.4%	28.3%	13.9%
on PDMS membrane:	53.7%	25.2%	27.9%	13.5%
Max. sensitivity S_{max}: (%/Oe)	0.034	0.022	0.113	1.06
Field of S_{max}:(Oe)	800	80	160	8

4.1.6 GMR sensors in circumferential geometry

In this paragraph, a conceptually new approach for the detection of magnetic objects flowing through a fluidic channel is introduced. This detection scheme is facilitated by the unique mechanical properties of the prepared soft GMR sensor elements, which allow them to be reshaped on demand after their fabrication. It is demonstrated that using this approach the stray fields generated by the flowing magnetic objects can be detected virtually in all directions (*isotropic sensitivity*)¹⁶⁶, which is unique compared to conventional rigid sensors^{88,193}.

Magnetic particles are widely used for diagnostic or therapeutic purposes in biology and medicine^{190-192,194}, implying the necessity of implementation of magnetic field sensors in complex biomedical systems. In this respect, magnetoresistive sensors, especially those relying on the GMR effect represent an efficient solution for the use in fluidic biodetection platforms due to their high sensitivity¹⁹⁵. Planar^{88,196,197} as well as rolled-up⁸⁵ magnetic sensors are already incorporated in microfluidic channels enabling detection of magnetic particles. The fabrication of these magnetic sensors requires intensive lithography processing and is therefore expensive and time consuming^{187,190}. In contrast, for the dynamically developing millifluidic approach¹⁹⁸, which implies the use of millimeter size objects, a sensor can be of a larger scale and its design can be simplified substantially¹⁹⁹. In this case, cost effective solutions for a magnetic sensor with an attractive possibility to be easily integrated into a system and to be reused several times are of great advantage.

GMR elements on free-standing elastomeric membranes can attain the above mentioned requirements in an elegant way. The prepared GMR sensors combine the advantages of being flexible with the speed and performance of conventional magnetoresistive devices on rigid substrates⁶. Due to their compliant nature, they can be efficiently implemented in a millifluidic system by wrapping them tightly around the fluidic channel¹⁶⁶, as shown in **figure 4.7a**. Given the imposed cylindrical symmetry, an isotropic sensitivity can be expected for detection of the stray fields of magnetic particles in a suspension⁸⁷ that flows through the tubing. This is a unique feature of flexible magnetic sensors compared to their rigid planar counterparts, which are able to detect only a component of the magnetic stray field, parallel to the sensor's plane, thus limiting the possibility for efficient and quantitative detection of small magnetic objects. In addition, the cylindrical symmetry of the wrapped sensors makes the detected signal less dependent on the position of a magnetic object inside the tubing, since the sensing element covers its entire circumference. Therefore, this approach can diminish the need of applying an external magnetic bias field to align the magnetic moment of the particles with the direction of maximum sensitivity of a conventional planar sensor. This feature is particularly interesting for a quantitative analysis of microscopic objects *in-flow*, which is currently realized by optical means, mainly²⁰⁰. Advanced magnetic analysis in fluidic systems is based on the selective immobilization of magnetic objects at the sensor site and the subsequent magnetization or alignment of the stray fields^{187,190}. Finally, in combination with magnetic particles as biomarkers^{192,201},

these compliant magnetic sensors can be considered as a new generation of biosensors for cells or even biomolecules^{187,190} evading many difficulties of traditional optical detection methods²⁰² like low speed, excitation, bulky and expensive equipment, biomolecular amplification and the need for transparent packaging. The potential of the magnetic in-flow detection in flexible fluidic systems was subsequently demonstrated in collaboration with G. Lin *et al.*^{86,203}.

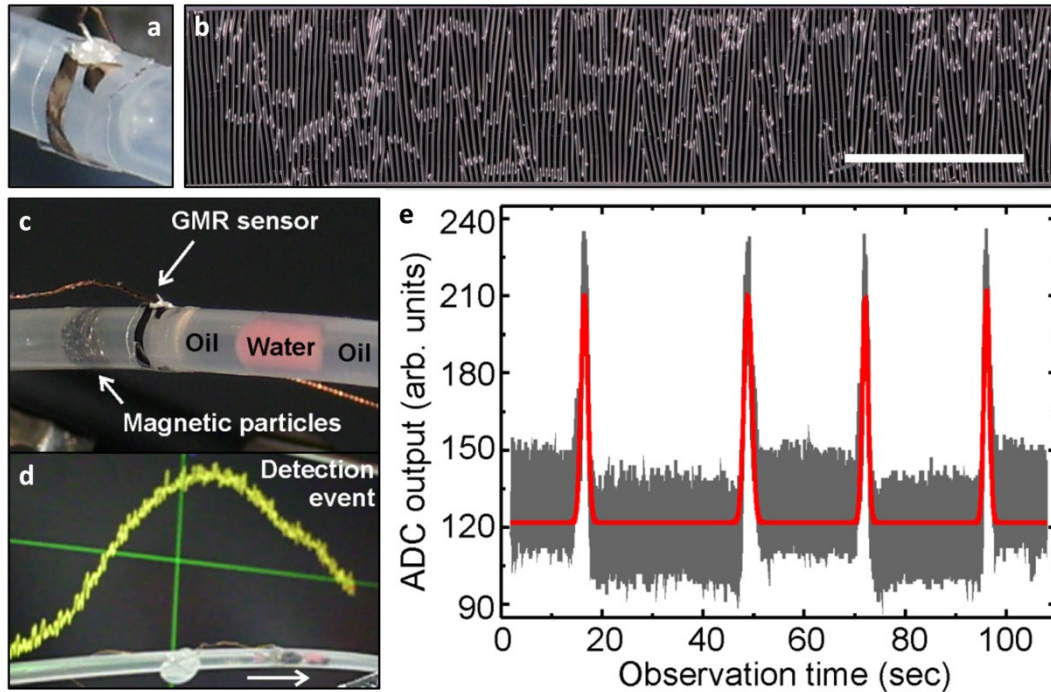


Figure 4.7 | Detection of magnetic particles in a fluidic channel: (a) soft multilayer element of $[\text{Py}/\text{Cu}]_{30}^{2\text{nd}}$ wrapped around the circumference of a Teflon tube and contacted using silver paste. (b) Optical microscopy image of the wrinkled sensor surface on a free-standing PDMS membrane. (scale bar: 1 mm) (c) Agglomerate of FeNdB particles suspended in oil and separated by colored water droplets inside the tube approaching the wrapped GMR sensor. (d) Sensor signal on an oscilloscope (background) as the magnetic cluster is passing the multilayer element (foreground). (e) Several consecutive detection events of particles passing the soft GMR sensor without an alignment of their magnetic moments. The gray line shows the acquired data, the red line is included as a guide to the eye. Experiment conducted in collaboration with Larysa Baraban (TU Dresden) and Daniil Karnaushenko (IFW Dresden). Figure compiled from [166].

To demonstrate the in-flow detection of magnetic particles using the soft GMR multilayer elements within the proposed detection approach, a simple millifluidic circuit was designed using a Teflon tube (inner diameter: 1.5 mm; outer diameter: 3.2 mm). Detection of magnetic particles typically requires a high sensitivity of the sensor to magnetic fields in the range of 10 Oe and below^{85,187,196,204}. As discussed in the previous paragraph, because of their outstanding sensitivity to small magnetic fields, $[\text{Py}/\text{Cu}]_{30}^{2\text{nd}}$ multilayers are chosen for this task. A microscopic image of the GMR layer after peeling, showing its thermally induced wrinkling, is displayed in figure 4.7b. Due to the flexibility of the prepared sensor elements it is possible to wrap the GMR film on the rubber membrane around the entire outer circumference of the millifluidic channel (figure 4.7a,c). No adhesive was used to attach the sensor to the tubing, which renders the detachment and re-use of individual elements possible. The

fluidic circuit allows the flow of magnetic particles inside the tube towards the sensing element. The wrapped sensor was contacted for a two-probe measurement of the electrical resistance with a twisted pair of thin copper wires (0.1 mm) using conductive silver paste and connected to the self-made data acquisition hardware described in chapter 3.2.4. The experiment was performed using commercially available $\text{Fe}_{67}\text{Nd}_{22}\text{B}_{10}$ magnetic particles (FOB Shanghai, Ref. Nr. QJK-ES) dispersed in a mineral oil (Sigma Aldrich, M5904). 2%v/v of sorbitane monooleate (Sigma Aldrich, S6760) was added to reduce the wetting of the dispersion on the tube walls. When placed in a liquid, the magnetic particles quickly aggregate, forming macroscopic clusters with sizes of about 1 mm. These clusters were pumped into the fluidic channel. In order to separate neighboring clusters for detection, water droplets, colored by red ink, were injected into the channel as spacers (figure 4.7c). As the magnetic particles appear in close vicinity of the GMR detector the total resistance of the sensor element decreases, resulting in an easily detectable voltage change of the sensor's output (figure 4.7d). Several consecutive in-flow detection events are demonstrated in figure 4.7e by monitoring the time evolution of the sensor's output. The signal to noise ratio is about 13 dB, which allows detecting reliably the magnetic objects of interest and suggests that even smaller particles can be detected.

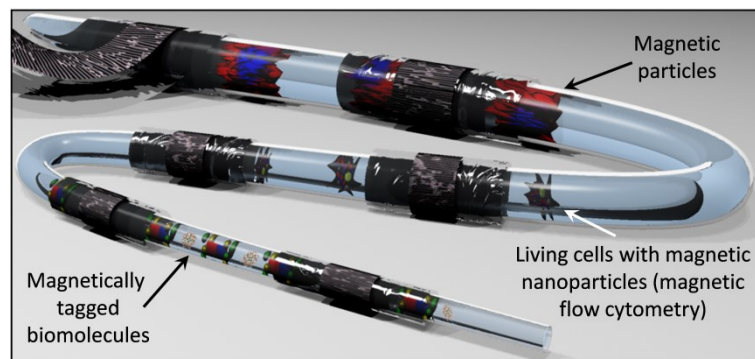


Figure 4.8 | Concept of isotropic detection for biomedical applications: Conceptual sketch demonstrating the potential of compliant magnetic sensors with isotropic sensitivity for the in-flow detection of magnetic objects of different sizes in fluidic channels for biomedical applications. Artwork by Daniil Karnaushenko (IFW Dresden). Figure taken from [166].

In conclusion, the demonstrated concept for in-flow detection of magnetic particles in millifluidics using GMR sensors on PDMS membranes offers the following advantages compared currently available solution based on rigid magnetic sensors: (i) sensing of the magnetic stray fields in virtually all directions (isotropic sensitivity) without the need of an alignment of magnetic moments; (ii) simplicity of the sensor integration into a fluidic circuit; (iii) possibility of being reused on demand. Thus, the approach of flexible magnetic sensors wrapped around the circumference of a fluidic channel potentially opens exciting possibilities in the field of biology and chemistry, which are conceptually highlighted in **figure 4.8**. The displayed tubing may represent a timeline for a further development and miniaturization of the proposed technology, with the upper part (in-flow detection of

magnetic particles) being realized on a proof-of-concept level, as described above. As a next stage, the detection of biological objects, *e.g.* living cells with accumulated magnetic nanoparticles for magnetic-activated cell sorting (MACS)²⁰¹, is envisioned. With further miniaturization, the in-flow detection of magnetically tagged biomolecules^{187,190} seems feasible. However, on smaller scales, the implementation of rolled-up technology²⁰⁵ will be necessary for the sensor fabrication and integration into fluidic systems^{85,206}.

4.1.7 Stretchability test

The demonstrators presented in the sections 4.1.4 and 4.1.6 proved that the prepared GMR multilayer sensors are functional on curved surfaces. However, stretchable devices need to withstand *tensile deformations* as well. In this respect the thermally induced wrinkling of the GMR layer on soft membranes is can help to protect the metallic film from cracking and breaking by smoothing out the buckles during uniaxial elongation of the rubber substrate²⁵. Flat metal films without surface wrinkling are expected to withstand tensile strains of below 1%^{135,136}. In order to test the stretchability of the prepared sensor elements, a sample of $[\text{Co}/\text{Cu}]_{50}^{\text{st}}$ multilayers is mounted into the computer controlled GMR characterization setup with *in situ* stretching capability. Details of the experimental setup and sample mounting are provided in sections 3.2.1 through 3.2.3. For the stretchability investigation, only specimens were used, which revealed no cracks in the GMR film after preparation. The measurement routine includes applying an external uniaxial strain to the sample and, for each strain value, recording a GMR curve at room temperature.

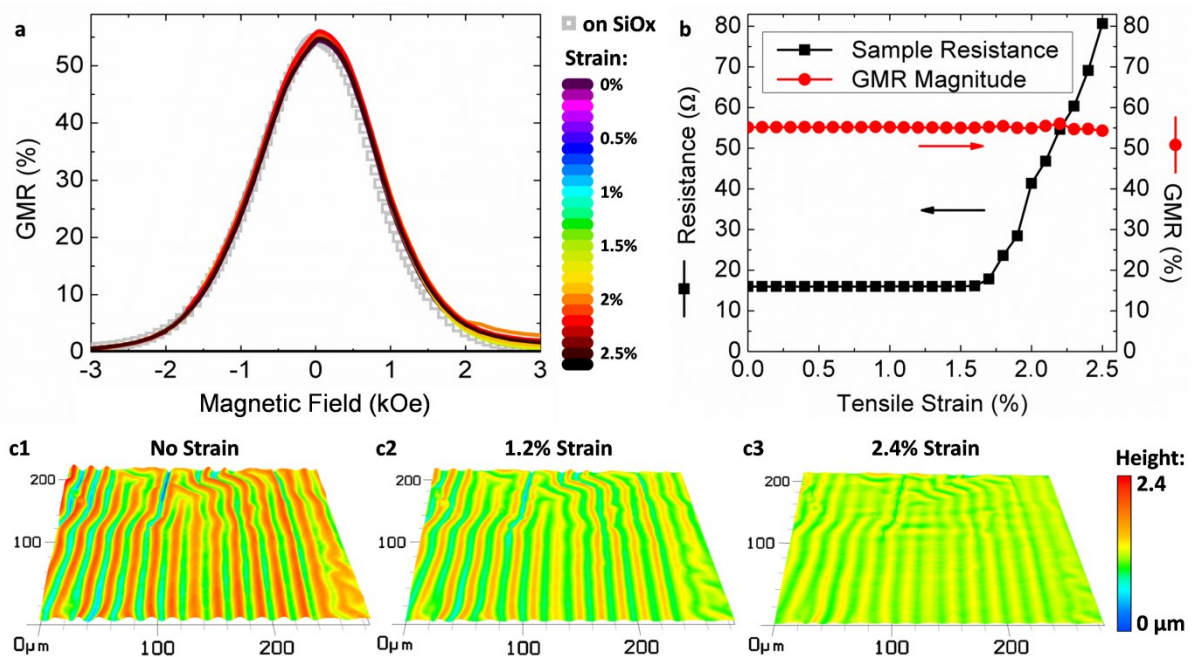


Figure 4.9 | Stretching test of a wrinkled GMR sensor on PDMS membrane: (a) 27 GMR curves of a $[\text{Co}/\text{Cu}]_{50}^{\text{st}}$ multilayer element measured at different applied strains (according to the legend) plus the reference curve recorded on a rigid SiOx wafer (□). (b) GMR magnitude (●) and sample resistance (■) in dependence of the imposed tensile strain. (c) 3D confocal microscopy images of the wrinkled GMR layer subjected to an increasing strain along the horizontal axis.

Figure 4.9a shows GMR curves for increasing strains applied to the multilayer element. All curves, according to the color chart in the legend, are plotted in the graph and are congruent to each other. Hence, the GMR characteristic remains unaffected by applied tensile deformations up to 2.5%. The data obtained during the stretching experiment is summarized in figure 4.9b, which displays the strain dependent GMR magnitude and absolute sample resistance of the sensor element during stretching. The curves show that the resistance remains constant for tensile strains below 1.7%. In this regime the sensor can be regarded as *strain invariant*, as its signal can be directly correlated to an in-plane magnetic field without compensating for an resistance change due to the tensile deformation. With further stretching, the resistance rises strongly until the electrical conduction across the element is lost above 2.6%. This increase of resistance at higher strains is attributed to the formation of microcracks, which lower the cross section of the conducting metal film. The most striking aspect of the stretching experiment is that, although its absolute resistance is increasing by a factor of about 5 during the elongation, the GMR ratio remains at a constant level. Hence, as demonstrated with the matching GMR curves, this suggests that even if the metallic film is partly damaged by the imposed tensile strain, the GMR effect is still present without major deterioration and the sample acts as a magnetic sensor element with the same performance as on rigid silicon substrates¹⁶⁶.

Tensile strains imposed on magnetic multilayers are actually expected to influence the GMR effect by reducing the spacer thickness and thus varying the interlayer exchange coupling^{4,207}. In the conducted stretching experiment however, no change of the GMR ratio upon stretching is found, which indicates that the tensile strain on the actual GMR multilayers is low due to the presence of the wrinkles. A set of confocal micrographs showing the wrinkled topography of the GMR film at zero strain and at two different stretched states is provided in panels (1-3) of figure 4.9c. With increasing strain, the wrinkles become less pronounced and the entire metal film becomes smoother.

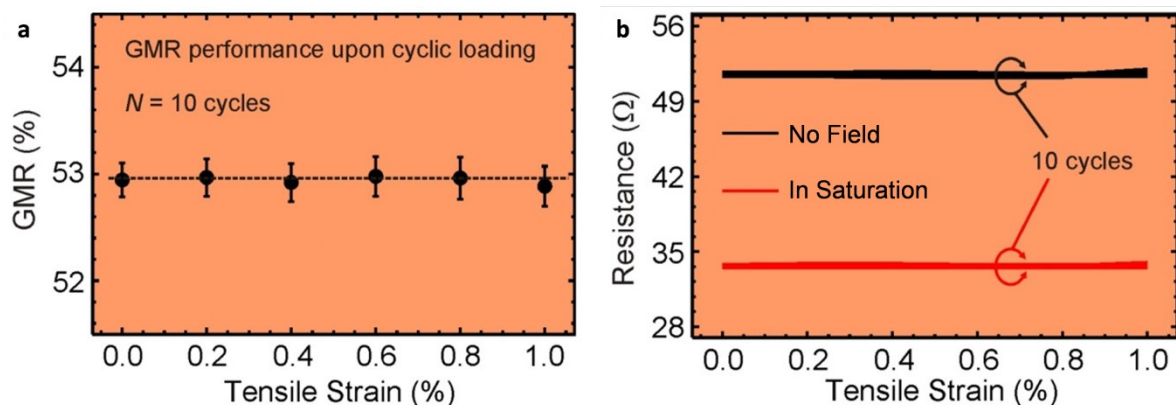


Figure 4.10 | Cyclic loading of stretchable GMR multilayers: (a) GMR ratio of $[\text{Co}/\text{Cu}]_{50}^{\text{st}}$ multilayers on free-standing PDMS in dependence of the tensile strain with deviations from 10 stretching cycles up to 1%. (b) Resistance of the wrinkled GMR film during the experiment measured without applied external magnetic field (black) and at an in-plane field of 3 kOe (red). Figure compiled from [6].

In order to demonstrate the elastic behavior of the prepared sensors, cyclic loading experiments were performed, which include measurements of resistance and the GMR effect during repeated

consecutive stretching and relaxing periods. **Figure 4.10a** shows the progress of the GMR magnitude of a stretchable $[\text{Co}/\text{Cu}]_{50}^{\text{st}}$ multilayer element over tensile strain with the error bars representing the standard deviation from 10 loading cycles between 0% and 1%. The GMR ratio remains at a constant value of $\approx 53\%$ with low deviations of $\approx 0.2\%$. The resistances in the absence of a magnetic field and in magnetic saturation during the 10 cycles are plotted in figure 4.10b. As expected, the resistance of the GMR multilayer upon magnetic saturation is reduced. However, both values (with and without applied magnetic field) remain unchanged when the magnetoelectronic element is reversibly stretched and relaxed, which makes it well-suited for magnetic sensor applications in environments where dynamic deformations are required.

In conclusion, four different kinds of GMR multilayer elements were fabricated on free-standing elastic rubber membranes, which exhibit the same magnetoresistive performance as respective devices prepared on conventional rigid silicon substrates¹⁶⁶. Each of the investigated multilayer systems possesses a magnetoresistive feature, which makes it beneficial to specific sensor applications. Two application fields, namely the operation on a curved surface⁶, *e.g.* in electrical machines for e-mobility, as well as the detection of magnetic particles with a unique isotropic sensitivity¹⁶⁶, *e.g.* for bio and medical applications, were demonstrated on a proof-of-concept level. The GMR films on top of the elastic PDMS membranes are subjected to a pronounced thermally induced wrinkling, which does not affect their magnetoresistive response characteristic⁶. This effect, on the one hand, allows defective elements to be self-healed¹⁴⁵ and, on the other hand, protects the magnetic nanomembrane from breaking upon tensile deformations⁶. *In situ* stretching experiments revealed, that the sensor elements are stretchable up to 2.5% uniaxial strain without altering their magnetic sensing capabilities. Even though the magneto-sensitive film gets damaged at higher strains, the GMR ratio is maintained until the electrical contact is lost¹⁶⁶. The elastic behavior of the prepared sensor elements was demonstrated in a cyclic loading test. These results represent the world's first elastically stretchable magnetic sensors.

4.2 Stretchable spin valves

Besides multilayers, also other GMR systems are known, which provide superior performance in particular aspects that are vital to specific application fields⁹⁵. As introduced in section 2.2.4, spin valves (SV) exhibit a sensitivity that even exceeds the values of $[\text{Py}/\text{Cu}]_{30}^{2\text{nd}}$ or other GMR multilayer systems¹²⁴. This makes them particularly interesting for many applications, where the detection of small magnetic fields is required. Besides the ones already mentioned in section 4.1.5 and 4.1.6, SVs also facilitate orientation and navigation capabilities, *e.g.* by detection of the earth magnetic field. Hence, a mechanical compliance of spin valves, in terms of stretchable magnetoelectronics, is highly promising for wearable^{53,208} and implantable^{65,67} electronics as well as for advanced bio-medical systems⁴⁷ to be equipped with magnetic functionalities. Most of these applications also require higher stretchabilities of the functional components to be integrated. Both aspects, increase of magnetic

sensitivity and stretchability, are covered by the stretchable spin valves¹⁶⁷ introduced in this subchapter.

4.2.1 Random wrinkles and periodic fracture

The fabrication process of stretchable SVs is similar to the stretchable multilayers discussed above. The deposited magnetic layer stack resembles an in-plane IrMn-based top-pinned symmetric SV and is described in detail in chapter 3.1.5. If not stated differently, the exchange bias direction was chosen to be perpendicular to the long axis of the patterned sensor stripe (cross-pinned configuration). The preparation steps are reflected schematically in **figure 4.11** with an emphasis given on the morphologic transitions occurring during the fabrication, which play a key role for the enhanced stretchability in this case. The bottom 5 nm thick Ta seed layer, under the used sputter conditions grows with a strong compressive stress. This stress relaxes into the soft rubber substrate, forming a *random wrinkling* pattern¹⁰⁰. Hence, the subsequent spin valve stack is deposited onto a wrinkled surface in the same process without interrupting the vacuum. An additional pattern of parallel trenches (*periodic fracture*) is induced in the SV film by the peeling process. Upon stretching, a pronounced grating of microcracks occurs, which resembles the pattern of the trenches. The mechanical flexibility and stretchability of the prepared SV sensors is demonstrated in the center of figure 4.11, where a free-standing sample is manually twisted and stretched, respectively, using tweezers.

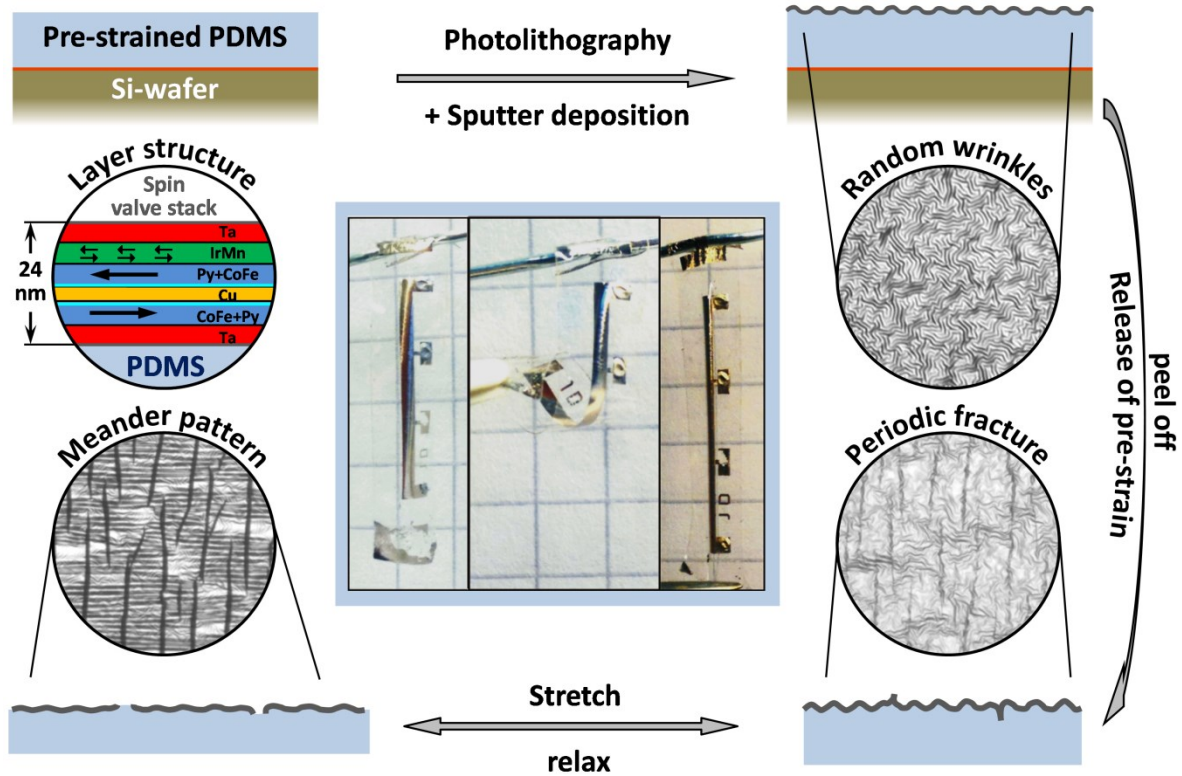


Figure 4.11 | Morphologic transitions during the preparation of stretchable spin valves: The top right part conceptually shows the PDMS film on SiO_x wafer as the substrate and the layer composition of the spin valve stack. After deposition, the SV film is randomly wrinkled, as shown in the top right micrograph. Peeling the sensor element from the supporting wafer leads to the formation of a periodic fracture pattern (bottom right), which acts as a template for the compliant meander pattern that develops upon stretching (bottom left). The central part shows photographs of a prepared SV element (left) that can be distorted (center) or stretched (right). Figure compiled from [167].

A detailed investigation of the sample morphology is crucial to understand the mechanism that accounts for the stretchability obtained in the fabricated spin valves. In AFM measurements on the SV layer stack grown on PDMS, which is still attached to the handling wafer, provided in **figure 4.12a**, the random wrinkling is clearly observed (period: 1.4 μm and amplitude: ≈ 160 nm). An AFM image recorded after peeling the PDMS membrane with the sensor along the stripe direction is given in figure 4.12b, showing the parallel trenches, which are oriented along the short axis of the sensor stripe with a mean periodicity of 13.9 μm . A periodic fracture of the sensor film upon peeling was not observed in the previous case of GMR multilayers prepared in the same way^{6,145,166}. Instead, these multilayers did exhibit a pronounced parallel wrinkling upon peeling, which is in contrast to the observed random wrinkling of the Ta seed layer in this work. The parallel wrinkling in GMR multilayers was assigned to a thermally induced stress in the PDMS film⁶. Although the profile of the periodic fracture differs from the sinusoidal shape of the wrinkling in GMR multilayers, as shown by the line scan in figure 4.12c, the orientation and periodicity of both morphologic features is similar. Hence, the same physical origin of the two morphologic transitions can be expected. This statement is supported by a FIB/SEM investigation presented in section 4.2.4.

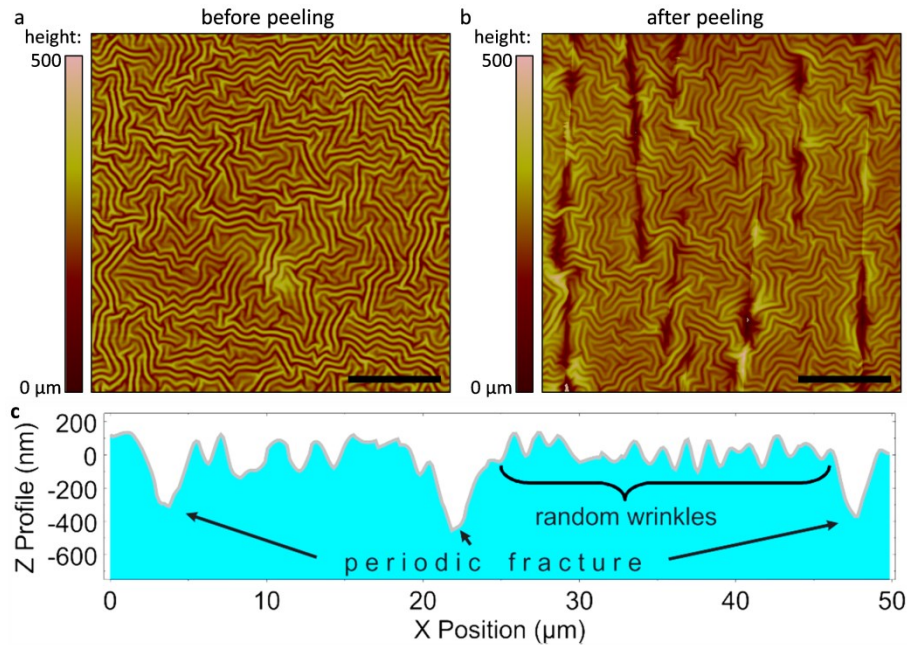


Figure 4.12 | AFM investigation of random wrinkles and periodic fracture: (a,b) AFM measurements of the sensor film before and after peeling, respectively. All scale bars: 20 μm . (c) Line profile extracted from (b) showing both morphologic features. AFM measurements were performed in collaboration with Peixuan Chen (IFW Dresden). Figure compiled from [167].

A rough estimation of the expected thermally induced wrinkling period of the spin valve film, according to the model suggested by Bowden *et al.*²⁴, which is described in section 2.4.3, can be provided, taking into account the film thickness as well as the mechanical properties of both, the metal film and the elastomeric support. However, since the metal film is already wrinkled before peeling, such an estimation has to be based on a nested higher generation wrinkling approach which treats the wrinkled layer as a thicker *effective skin* with different mechanical properties²⁰⁹. With the effective thickness represented by the entire amplitude of the present random wrinkling, its effective Young's modulus and Poisson's ratio is estimated on the base of the resulting materials composition. The 160 nm thick wrinkled effective skin consists of 15% the actual spin valve film (thickness: 24 nm). The remaining 136 nm are shared, in a first approximation, equally between the elastomer underneath ($E_{\text{PDMS}} = 1.6 \text{ MPa}$, $\nu_{\text{PDMS}} = 0.5$) and the air above ($E_{\text{air}} = 0 \text{ MPa}$). The Young's modulus and Poisson's ratio of the spin valve film is estimated by the respective parameters and thicknesses of the individual metal layers to be $E_{\text{SV}} = 193.3 \text{ GPa}$ and $\nu_{\text{SV}} = 0.32$. Using these values provides the estimation for the mechanical properties of the effective skin: $E_f \rightarrow E_{\text{skin}} \approx 29 \text{ GPa}$ and $\nu_f \rightarrow \nu_{\text{skin}} = 0.45$. Together with the properties of the PDMS support ($E_s = 1.6 \text{ MPa}$, $\nu_s = 0.48$; as already worked out in chapter 4.1.2), this gives a wrinkling period of 17.9 μm according to (2.15). This estimation is reasonably close to the observed fracture separation of $13.9 \pm 4.6 \mu\text{m}$. However, despite this good agreement, an influence of overstretching during the peeling process cannot be excluded completely.

4.2.2 GMR characterization

The spin valve elements on rubber membranes are magneto-electrically characterized and the data is compared with the performance of reference samples on rigid silicon substrates fabricated in the same deposition run. **Figure 4.13a** shows the field dependent GMR ratio measured at room temperature for the SV stacks on both substrates with the EB direction set parallel to the sensor stripe (see inset). The GMR curve consists of two sub-loops characteristic for the magnetization reversal of the magnetic free (at small fields) and pinned (shifted to higher fields due to the EB effect) layers. A maximum GMR value of more than 9% is obtained for both samples. Furthermore, the GMR characteristics are comparable which accounts for the good performance of the stretchable SV samples despite the strongly corrugated topography. Since spin valve elements are used for low field applications, its working region is limited to the switching region on the free (sensing) layer (*i.e.* between the two dotted lines). The corresponding GMR curves of only the free layer (minor loop characterization) is separately shown for both substrates in figure 4.13b. Although the maximum GMR ratio of the SV stacks is smaller than for GMR multilayers, a sensitivity of 1.4%/Oe at low fields of 12 Oe is achieved on PDMS, which is superior to the stretchable sensitivity-optimized [Py/Cu]₃₀^{2nd} multilayers¹⁶⁶. Figure 4.13c,d provides similar data for SV sensors with the EB set perpendicular to the lithographically defined sensor geometry. Here, the external magnetic field for the magneto-electronic characterization is applied perpendicular to the sensor stripe to be aligned with the pinning direction. Interestingly, a reduced GMR magnitude is observed on cross-pinned sensors on a rigid silicon substrate (see discussion below). However, also in this case, the GMR characteristics on both substrates are comparable to a certain extent, indicating that also spin valves can be prepared on free-standing rubber membranes with similar sensing performance as on rigid substrates.

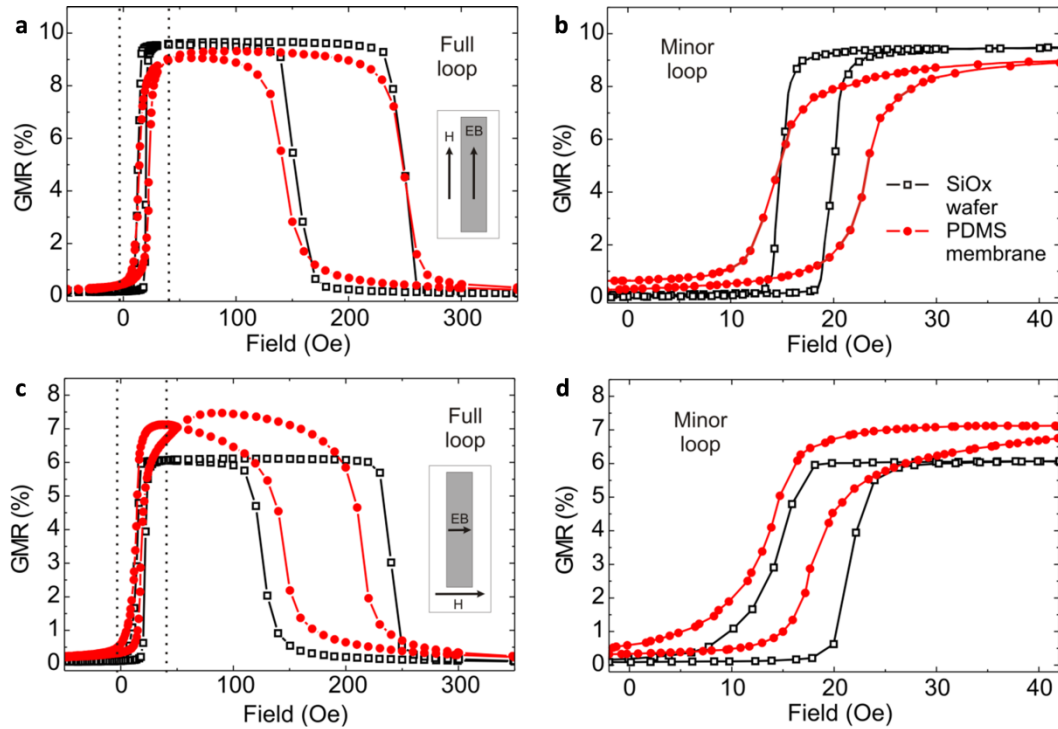


Figure 4.13 | GMR characterization of the spin valves: GMR curves of the prepared spin valve elements on free-standing PDMS membranes (●) and on a rigid SiOx wafer (■). Major loop (a) and minor loop (b) measurement for exchange bias set parallel to the long axis of the sensor stripe, as indicated in the inset. (c,d) Respective loops for exchange bias set perpendicular to the sensor stripe (cross-pinned configuration) as indicated in the inset. Figure taken from [167].

4.2.3 Stretching of spin valves

The free-standing PDMS rubber membranes with photolithographically patterned SV sensors on top were mounted onto the GMR characterization setup with *in situ* stretching capability. This study was conducted on cross-pinned sensor elements, as the stretching is possible perpendicular to the applied field and along the sensor stripe only. The applied field should be aligned with the EB direction for the characterization, as this defines the sensitive axis of the SV sensor. Furthermore, this configuration allows to reduce hysteresis of the free layer²¹⁰. Both aspects are crucial for an optimized sensor response in low field applications. However, since the direction of the EB is defined solely by magnetic means, it is not expected to significantly influence the mechanical stretchability of the prepared sensors. The measurement was performed according to the description given in chapter 3.2.1 GMR curves of the major loop and minor loop obtained at different tensile strains applied to a stretchable SV element are shown in **figure 4.14a** and b, respectively. Remarkably, the characteristic shape of the GMR curve as well as the GMR magnitude is similar up to high tensile strains of 29%. In figure 4.14c, the GMR magnitude and the absolute sample resistance in magnetic saturation are displayed in dependence of the applied strain. For small deformations below 2%, there is a slight increase in both values. Even though the resistance of the SV element increases strongly while the sample is expanded to higher strains, the GMR magnitude changes only very gradually, until the electrical conduction is lost beyond 29%. With increasing strain, the minor loop becomes more

sheared indicating a decrease of the sensitivity. Sensitivity values are obtained by averaging the slope of the ascending and descending branches of the minor loop. Furthermore, it is apparent that the hysteresis loops become significantly broader with rising strain. Both properties are plotted in dependence of the applied strain in figure 4.14d.

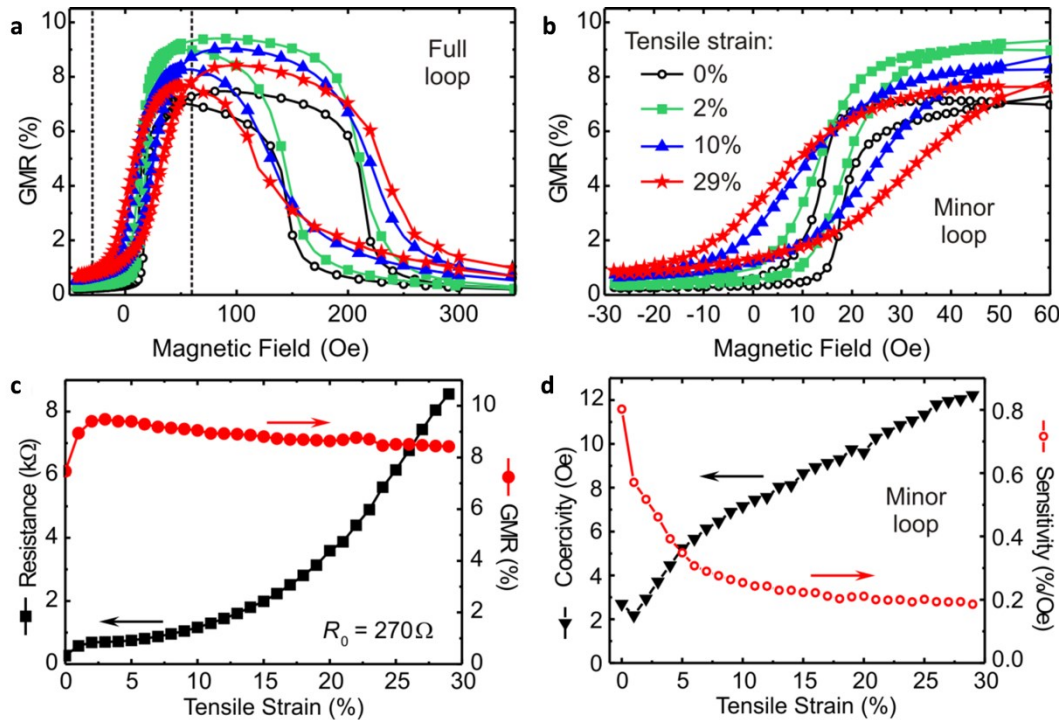


Figure 4.14 | Stretchability of spin valve sensor elements: Major loop (a) and minor loop (b) GMR curves at different applied strains according to the legend given in (b). (c) Magnitude of the GMR effect (●) and absolute sample resistance (■) in dependence of tensile strain up to the point where the electrical contact is lost. (d) Sensitivity of the SV element (○) and coercivity of the free layer (▼) over the applied tensile strain. Figure taken from [167].

In order to test the elasticity and long-term reliability of the reported sensor elements, extensive cyclic loading experiments were performed which involves repeated uniaxial deformations to moderate strains. First, cyclic loading experiments by stretching the sample between 0% and 5% were performed with a stretching rate of $0.03\% \text{ s}^{-1}$. Before cycling, an initial loading step to 10% is applied to the as-prepared sample to define the microcrack pattern as described above. The respective data, as displayed in **figure 4.15a**, shows a stable GMR magnitude and sample resistance in the stretched state, except for a very low increase in resistance during the first 10 cycles. Surprisingly, the resistance tends to increase strongly at the relaxed state until it gradually saturates to the level of the stretched state. This implies that fatigue of the SV film takes place when coming back from the stretched state to the fully relaxed state, *i.e.* as the gaps in the film close during unloading of the sensor element. Furthermore, it is conspicuous that the GMR effect in the relaxed state is increasing while the sensor is subjected to cyclic loading, until it also reaches the level of the stretched sensor. The different GMR magnitudes of the stretched and relaxed sample are in agreement with the data presented in figure 4.14c. The mechanisms leading to the varying magnetoresistance are discussed in the following

section. After about 160 loading cycles, the electrical conduction was lost in the stretched state with the relaxed state remaining stable with further cycling.

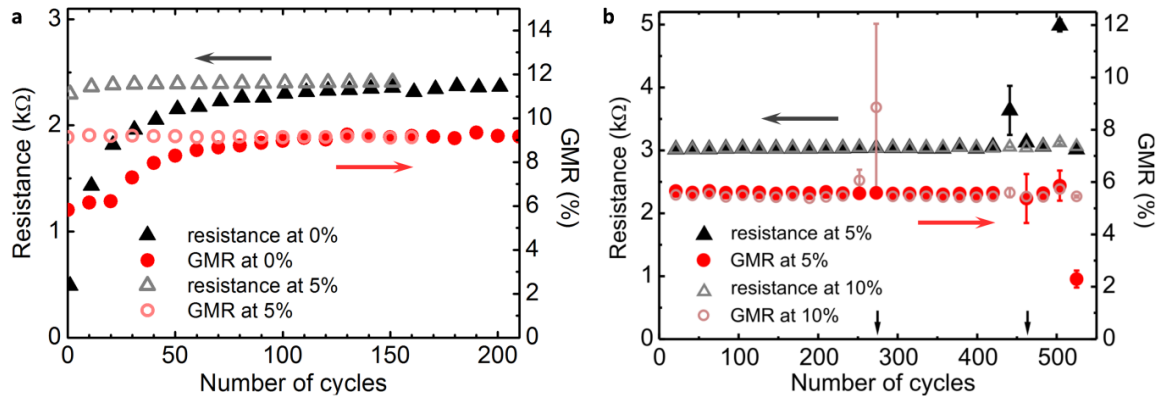


Figure 4.15 | Cyclic loading of stretchable spin valves: Cycling interval: (a) [0..5]%, with initial loading to 10% strain, (b) [5..10]%, with initial loading to 15% strain. Displayed are the GMR magnitude (●,○) and sample resistance (▲,△) at the minimum (filled symbols) and maximum (open symbols) strain over the number of loading cycles. Error bars represent the standard deviations of resistance values at magnetic saturation and GMR values on the plateau between the two hysteresis loops. Figure compiled from [167].

To avoid the fatigue upon full relaxation of the SV element, the cyclic loading procedure was adjusted to stretching between 5% and 10% strain with an initial loading to 15% strain (figure 4.15b). In this experiment the data shows similar GMR and resistance values at both strain states. Furthermore, no fatigue is observed, as all parameters remain at a constant level over several hundred loading cycles. Beyond 500 cycles the data starts to scatter progressively, which is attributed to electrical contact issues, rather than to a failure of the sensor element itself. The arrows on the lower axis indicate cycles when the contact was re-established by adding a small droplet of conductive paste to each bonding site. However, the stable behavior of the prepared SV elements suggests that the number and length of microcracks, created by the initial loading cycle is not changed during this experiment and renders the fabricated elements to be suitable as elastic and highly sensitive magnetoresistive sensors, if repeated relaxation to 0% strain is avoided.

4.2.4 Microcrack formation mechanism

To understand the underlying mechanisms that lead to the unique mechanical and magnetoelectronic behavior of the here presented stretchable sensors, a detailed microscopic investigation is performed. The much higher values of tensile strain that can be applied to the prepared SV elements, compared to the GMR multilayer based sensors^{6,145,166}, are accommodated by a distinct microcrack pattern occurring in the magnetic nanomembrane. **Figure 4.16a-c** shows a series of optical micrographs of the same area on the SV film at different applied strains along the horizontal axis (0%, 5%, and 20% respectively). These pictures reveal that the parallel trenches, which are formed upon peeling the SV elements from the handling support, evolve into open gaps as the rubber substrate underneath is expanded. In this respect, the trenches act as pre-determined fracturing sites for the formation of a compliant crack pattern. This microcrack formation gives rise to a meander-like structure that

maintains a network of connected slaps along the surface which can facilitate high tensile strains²⁹. Arrows in panel c indicate a conductive pathway across the highly stretched sensor surface. As described in chapter 2.4.1, random micro fracture of thin and flat metal films on elastomeric substrates is typically applied to fabricate highly compliant interconnects for stretchable electronic platforms^{102,141,211}. There are also fundamental investigations of periodic microcrack formation in thin metal films on polymeric substrates^{137,138,212,213}. However, a pre-determination of crack formation to obtain highly stretchable meander-like patterns was not obtained so far. Figure 4.16d,e show the topography of the relaxed and stretched SV film, respectively, obtained by confocal laser scanning microscopy. The apparent development of buckles perpendicular to the emerging gaps with rising strain originates from the Poisson's contraction of the elastomeric support^{137,138}.

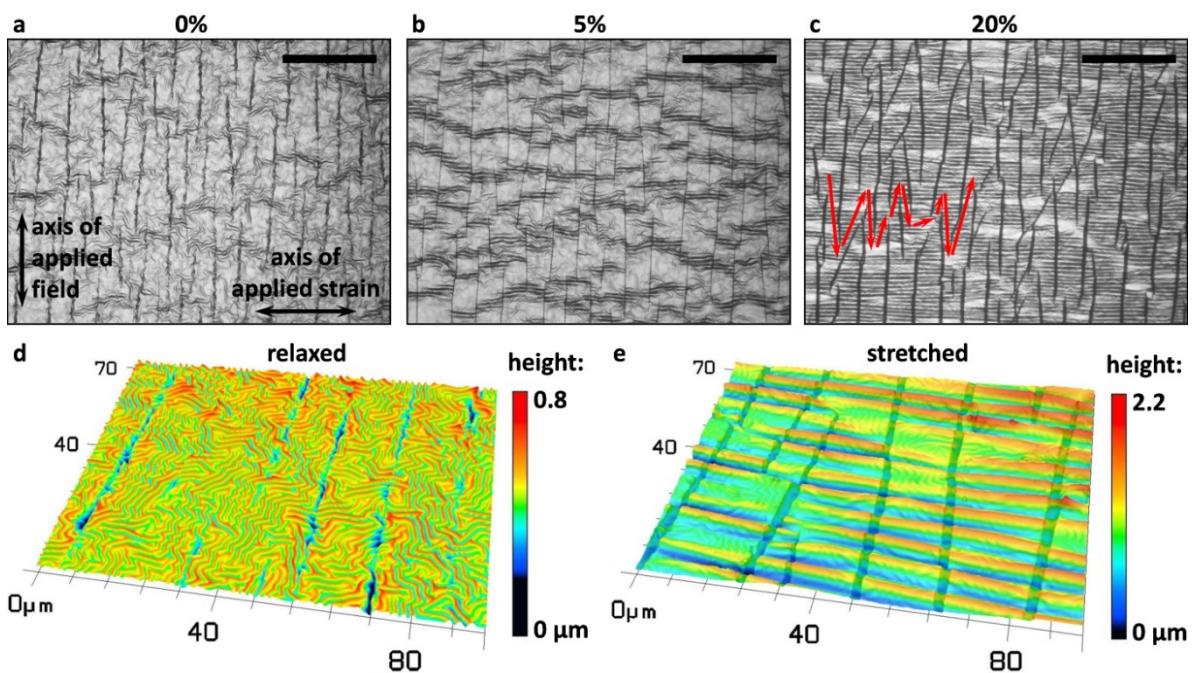


Figure 4.16 | Formation of a compliant microcrack pattern upon stretching: (a-c) Optical micrographs of the sensor surface at 0%, 5% and 20% tensile strains, respectively. Indicated in (a) are the directions of the applied strain and magnetic field. A conductive pathway through the expanded microcrack pattern is indicated in (c). (d,e) 3D confocal laser scanning images showing the topography of the relaxed and stretched SV film, respectively. Figure partially taken from [167].

In order to reveal the nature of the periodic fracture and the compliant microcrack pattern in more detail, FIB cuts through the spin valve layer on the PDMS film were performed. **Figure 4.17** shows SEM images of a selection of cuts through the unstretched sample after it was peeled from the handling wafer. The focus is on the investigation of the parallel trenches that represent the pre-determined fracturing sites for the microcrack pattern. It turns out, that in some cases the SV film is actually not cracked at the trenches that evolve perpendicular to sensor stripe (figure 4.17a) and others are apparently cracked, but still maintain the contact across (figure 4.17b). In figure 4.17c, one example of a completely fractured trench is shown, that was present before the stretching of the sensor. The way a metal film behaves upon compressive deformation on an elastomeric substrate, in

particular concerning the formation of cracks, strongly depends on its ductile properties⁴⁵. The different morphology that results from the release of the thermally induced pre-strain upon peeling, compared to the observations on GMR multilayers (chapter 4.1.2) are attributed mainly to the presence of the brittle IrMn layer. In contrast to the materials present in the multilayers, which all exhibit a good ductility, the IrMn may cause the SV film to crack rather than to wrinkle upon compression. Furthermore, the micrographs show the good adhesion of the wrinkled SV layer to the elastic PDMS membrane underneath, which is an important factor for the high stretchability of the here presented sensor elements.

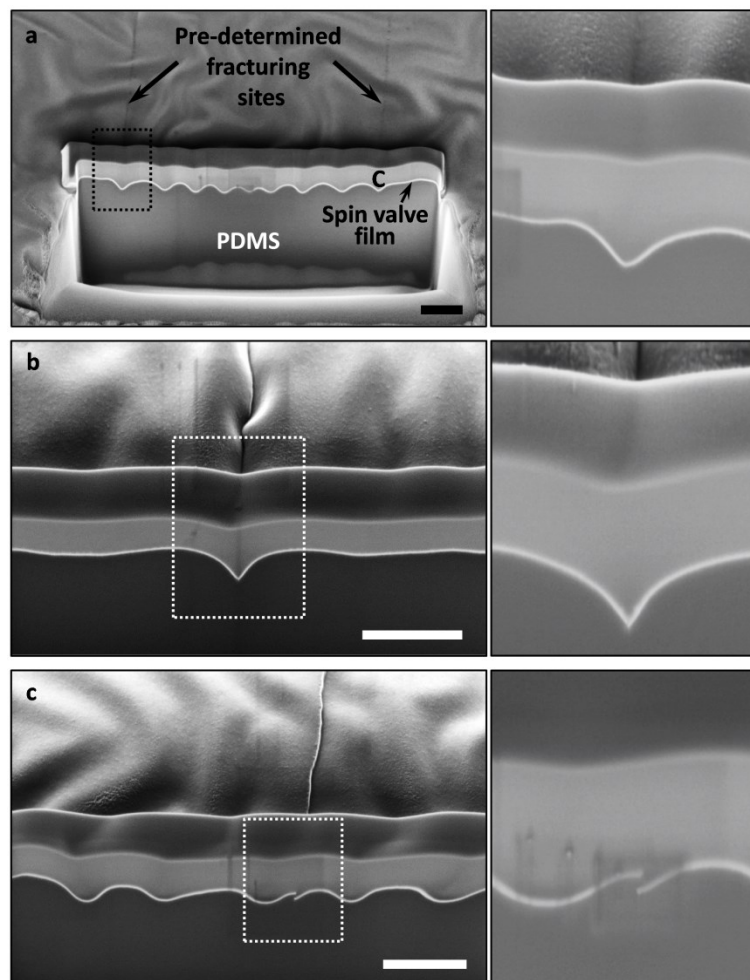


Figure 4.17 | FIB cuts through pre-determined fracturing sites: (a-c) SEM micrographs of three selected cuts through the peeled SV sensor. The right hand images show a magnification of the area marked on the left. All scale bars: 2 μm . A carbon bar was locally deposited prior to FIB milling to stabilize the cut edge. FIB milling and SEM investigation was performed in collaboration with Dr. Stefan Baunack (IFW Dresden). Figure taken from [167].

A further SEM investigation was performed on a SV sensor element in a stretched state, as presented in **figure 4.18**. It is clearly visible, that the random wrinkles from the Ta layer deposition are still present at high strains. Thus, the actual stress on the sensor layer slabs is assumed to be low and most of the strain is accommodated by the broadened microcracks. The deposition induced random

wrinkling supports the accommodation of strain at the sites that bridge the different slabs between two opening gaps. Also visible are the perpendicular buckles that occur upon stretching due to the Poisson contraction (figure 4.18a), which may also have a contribution to the perpetuation of conductive paths at higher strains. A FIB cut through one of the microcracks in the stretched state demonstrates that the adhesion between the metal layer and the PDMS membrane even endures at high tensile deformations (figure 4.18b). From this image, delamination and slipping of the sensor layer upon stretching can be excluded as the main mechanism during the elongation of the underlying PDMS membrane. Thus, a smart interplay between periodic fracture and random wrinkling allows for the high stretchability achieved in the presented SV sensor elements.

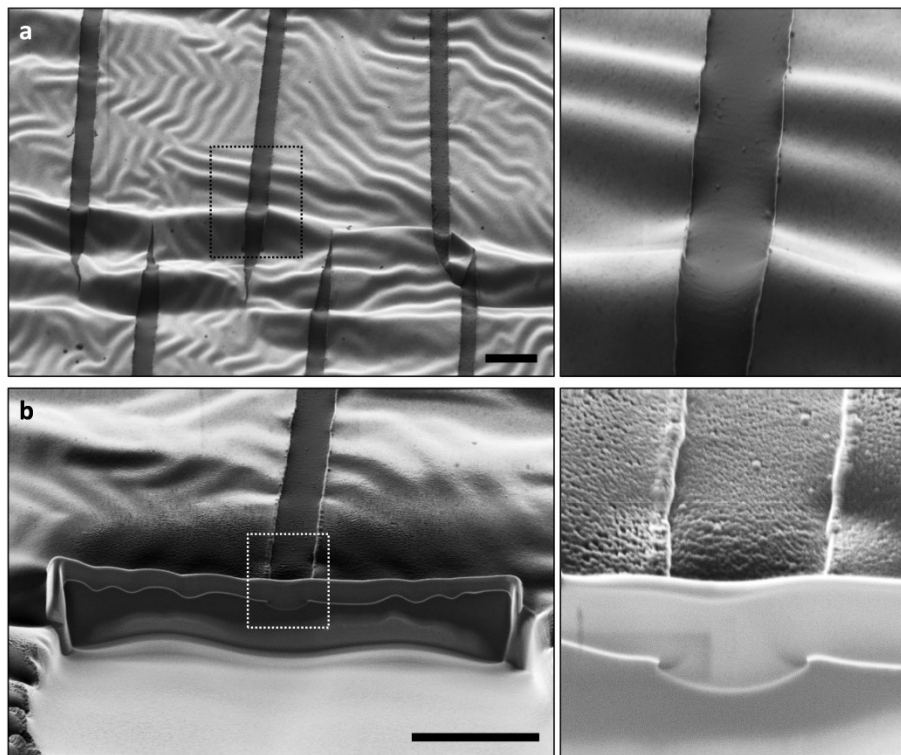


Figure 4.18 | SEM investigation of the stretched spin valve: SEM images of (a) the stretched sensor surface and (b) a FIB cut through a periodic fracture site. The right hand images show a magnification of the area marked on the left. Stretching was done along the horizontal axis by about 20%. All scale bars: 5 μm ; FIB milling and SEM investigation was performed in collaboration with Dr. Stefan Baunack (IFW Dresden). Figure taken from [167].

The induced periodic fracture of the sensor film not only allows for a high stretchability, but is also responsible for transitions in its GMR characteristic, which are highlighted in figure 4.14. As known, the GMR magnitude depends on the relative alignment of the magnetic moments of the free layer and the pinned layer⁹⁵. In the case of cross-pinned SV elements, there is a competition between the shape anisotropy (along the lithographically defined stripe) and the induced anisotropy by EB (perpendicular to the stripe). This biaxial anisotropy results in a misalignment of magnetic moments in the pinned layer, which leads to a reduced GMR effect. The discrepancy due to competing anisotropies is also illustrated in figure 4.13, where the cross-pinned spin valve (panel c) exhibits a lower GMR effect than

in the case of the EB aligned with the shape anisotropy (panel a). Upon stretching, the induced microcracks create perpendicular elongated slabs (figure 4.16), which cause the shape anisotropy to realign along their long axis (*i.e.* parallel to the EB), rather than along the lithographically defined sensor element. This establishes a favorable uniaxial anisotropy with aligned magnetic moments leading to the observed early increase in the GMR magnitude (figure 4.14c). For the cross-pinned sensors on free-standing PDMS, the GMR magnitude is enhanced even before stretching (figure 4.13c), as the periodic fracture is already present to some extent, as shown in figure 4.17c. Since the gaps are opening already at low strains due to the pre-determined periodic fracture, the transition of the shape anisotropy is completed at about 2% of tensile strain, which is enough to overcome the thermally induced pre-strain and open up the trenches into the periodic microcrack pattern. This morphological change induces the early increase in the absolute resistance as well. During cyclic loading the gaps are closing again upon full relaxation, which at the beginning restores the shape anisotropy along the sensor stripe leading to the reduced GMR effect. However, due to the thermally induced pre-strain, the edges of adjacent slabs further push against each other causing the observed fatigue at full relaxation (figure 4.15a). Hence, with continued cycling more and more microcracks remain open at 0% strain, suppressing the reestablishment of the unfavorable biaxial anisotropy. This effect accounts for the asymptotic adaption of the GMR magnitude in the fully relaxed state upon cyclic loading.

For higher applied strains the periodic cracks increase in length and width causing the absolute resistance to raise further (figure 4.14c). For flat metallic films on elastomeric substrates, the number of cracks is expected to increase with applied tensile strain^{138,212}. In the present case, however, the initial number of cracks is predetermined by the period of the parallel trenches upon peeling. It can be assumed that the number of periodic fractures is larger than the number of cracks necessary to accommodate the residual strain. Therefore, the number of cracks is not increasing for low and medium strains (figure 4.16a,b), even if the adhesion to the rubber is maintained and no slipping occurs. For higher strains, the number of necessary cracks eventually exceeds the number of initial periodic trenches and additional cracks may be formed (figure 4.16c). In any case, the first elongation creates the microcrack pattern and defines the absolute resistance of the sensor element, which is maintained for all strains below, except for a full relaxation back to strains below about 2%, as presented by the cyclic loading experiments in figure 4.15. If the strain rises above the first elongation, the microcrack pattern is extended and a higher resistance is set. However, the geometry of the individual slabs does hardly change, which leads to a stable GMR effect, as long as the electrical conduction along the sensor stripe is maintained.

The periodic fracturing can also explain in part the decreasing slope in the switching regions (*i.e.* the sensor's sensitivity) of the GMR curve (figure 4.14d). Indeed, the fragments between the arising gaps are not equal in shape (width: 13.9 μm with 4.6 μm standard deviation) which leads to different

switching fields for the individual slabs and thus a broadening of the magnetic switching behavior for the total sensor element. In addition to the modification of the shape anisotropy upon stretching, *i.e.* the broadening and shearing of the minor loop hysteresis (figure 4.14b) could be related to the occurrence of perpendicular buckling in the SV film. Since these buckles are also perpendicular to the applied magnetic field, the film bending and tilting on the flanks results in local out-of-plane field components. Hence, larger external fields have to be applied in order to align the magnetic moments on these locations.

In conclusion, we demonstrated an easy approach to fabricate highly elastic and sensitive spin valve sensors on free-standing elastomeric membranes by means of a predetermined periodic fracturing mechanism and random wrinkling. Both phenomena work together to create a meander-like self-patterning during the first stretch of the element. Tensile strains of up to 29% could be applied without major changes of the GMR magnitude of around 7%. A sensitivity of 0.8%/Oe was achieved for the as-prepared spin valve, which decreases down to 0.2%/Oe upon stretching. This and other minor influences on the response characteristics during stretching could be explained by the morphological transitions occurring in the sensor film. Cyclic loading experiments were conducted, which revealed a very stable behavior over 500 periods, accounting for the elasticity and reliability of the prepared elements. The proposed technology opens the way for a successful integration of large area magneto-electronic components in stretchable hybrid electronic systems. The obtained stretchability allows applications in the field of wearable²², on-skin⁵³ and implantable⁴⁷ electronics.

4.3 Direct transfer printing of GMR sensorics

All approaches to fabricate stretchable magnetoelectronics described so far rely on the direct deposition and lithographic structuring of magnetoresistive thin films onto elastomeric membranes. The soft substrates, attached to a rigid handling support, were pre-strained thermally in order to induce wrinkling^{6,145,166} or a periodic fracture pattern¹⁶⁷. However, this method, although it allowed to fabricate the world's first stretchable magnetic field sensorics⁶, is associated with severe process limitations, preventing significant advances in performance and level of complexity and thus, restricting the applicability of the technology. First of all, the photolithographic structuring on the PDMS surface is challenging for feature sizes well below 100 μm ¹⁴⁵ and multiple patterning steps, which are absolutely necessary for the integration of magnetoelectronic components into multifunctional stretchable electronics platforms, can hardly be realized on PDMS reliably. Another crucial drawback is related to the limited stretchability of the functional elements relying on wrinkling due to thermally induced pre-strain. In fact, stretchabilities of a few percent only^{145,166} can be achieved in this way, unless cracking of the sensing layer is permitted, which can result in higher stretchabilities¹⁶⁷. However, stretching due to crack formation is applicable only for thin film elements that are much larger than the cracks and hence, this approach contradicts the device miniaturization, which is highly relevant especially for the integration into wearable navigation and orientation

systems, bio-medical systems^{188,189} or for the fine mapping of inhomogeneous magnetic fields and textures. Other applications fields like smart skins^{44,53}, functional medical implants^{47,67} and soft robotics^{69,74}, require stretchabilities of electronic components in the order of 20% or more for useful integration. Further process limitations are related to the thermal and chemical conditions the polymeric substrate can endure during the fabrication of the magnetoelectronic system. These severe limitations call for a novel fabrication strategy of stretchable magnetoelectronic devices that allows for smaller structures and mechanically induced pre-strain. The preparation method described in the following section is inspired by transfer printing techniques¹⁷⁰ and was specifically developed in the scope of this work

4.3.1 The direct transfer printing process

For the fabrication of stretchable magnetic sensorics, a *single step transfer printing* process was developed¹⁶³. It allows preparing miniaturized and complex GMR systems on common rigid (donor) substrates, which are then directly transferred onto the elastomeric receiving substrate, without requiring micropatterned stamps, as for conventional transfer printing methods. With the preparation of entire magnetoelectric sensor systems or arrays including wiring and contact structures on silicon wafer substrates, the full potential of state-of-the-art microfabrication methods and thin film technologies can be exploited to reach a level of complexity that is not met when the magnetic layer stack is directly deposited onto elastomeric membranes. One of the key advantages is that the receiving PDMS substrate can be pre-stretched mechanically during the transfer process, which results in higher wrinkling amplitudes compared to the thermally pre-strained case^{24,27}. This is beneficial to achieve higher stretchabilities without inducing cracks in the functional magnetic layer. Another advantage of this approach is that the direction of the pre-strain can be controlled in order to either prepare systems that are compliant along one defined axis or even achieve biaxial stretchability³⁶. Additionally, the advanced microfabrication potential allows for the combination with compliant meander geometries^{29,142} and fractal designs³².

Figure 4.19 shows the process flow of the developed direct transfer method for GMR multilayer sensor elements. One of the key aspects is a sacrificial layer on top of the donor substrate (figure 4.19a), which facilitates the preparation of GMR sensor systems on its surface. For this purpose, Ca²⁺ metal cross-linked PAA with a total thickness of only 80 nm was chosen, fulfilling all crucial requirements to the sacrificial layer¹⁷³. Details of its preparation can be found in section 3.1.7. The resultant sacrificial layer provides a very small roughness of below 1 nm, as revealed by an AFM investigation in figure 3.11, which is necessary for the successful growth of the high performance magnetic sensor layer. Furthermore, the metal cross-linked PAA possesses high molecular weight (>400K) and is chemically inert to standard microelectronic processing based on photoresists. To still facilitate a gentle removal of the PAA sacrificial layer, it is dissolvable in strong alkaline (pH > 10), acidic (pH < 2) or chelating (a solution of polydentate molecules like

ethylenediaminetetraacetic acid, EDTA) solvents only. In combination with the excellent temperature stability of up to 150°C, these properties allow using the entire spectrum of multiple lithographic patterning and thin film preparation techniques to prepare sophisticated GMR sensoric systems on a Si-wafer donor substrate (figure 4.19b). On top of the sensors, a 4 nm Si capping layer is sputtered that accounts for the plasma induced adhesion to the receiving PDMS membrane. The free-standing PDMS receiver is prepared as described in section 3.1.2, using 1,500 rpm for spin coating, and peeled from the handling support directly after cross-linking (figure 4.19c). The elastomeric membrane of 60 μm thickness is pre-stretched and fixed to a holding frame (as described in section 3.1.6), before it is exposed to a weakly excited RF oxygen plasma at 50 W for 30 seconds together with the Si coated sensors on the donor substrate (figure 4.19d). The pure oxygen plasma activates both, the PDMS silicone rubber surface and the naturally oxidized thin silicon film on top of the sensor surface, which allows for a strong covalent bonding to each other upon contact (figure 4.19e). The adhesion is promoted by means of heat and pressure (60°C and ≈ 10 kPa for 30 minutes), after the uniaxially or biaxially pre-stretched PDMS membrane was flipped on the activated surface of the donor substrate (figure 4.19f). To finalize the transfer, the PDMS membrane is released from the holding frame and the sacrificial layer is dissolved in an aqueous solution of EDTA. This smoothly detaches the donor substrate from the sensor system on the receiving membrane and simultaneously releases the mechanically induced pre-strain, which leads to a wrinkling of the transferred structures on the PDMS rubber (figure 4.19g). Hence, the wrinkled sensor elements on the soft support can be elastically stretched according to the induced pre-strain (figure 4.19h).

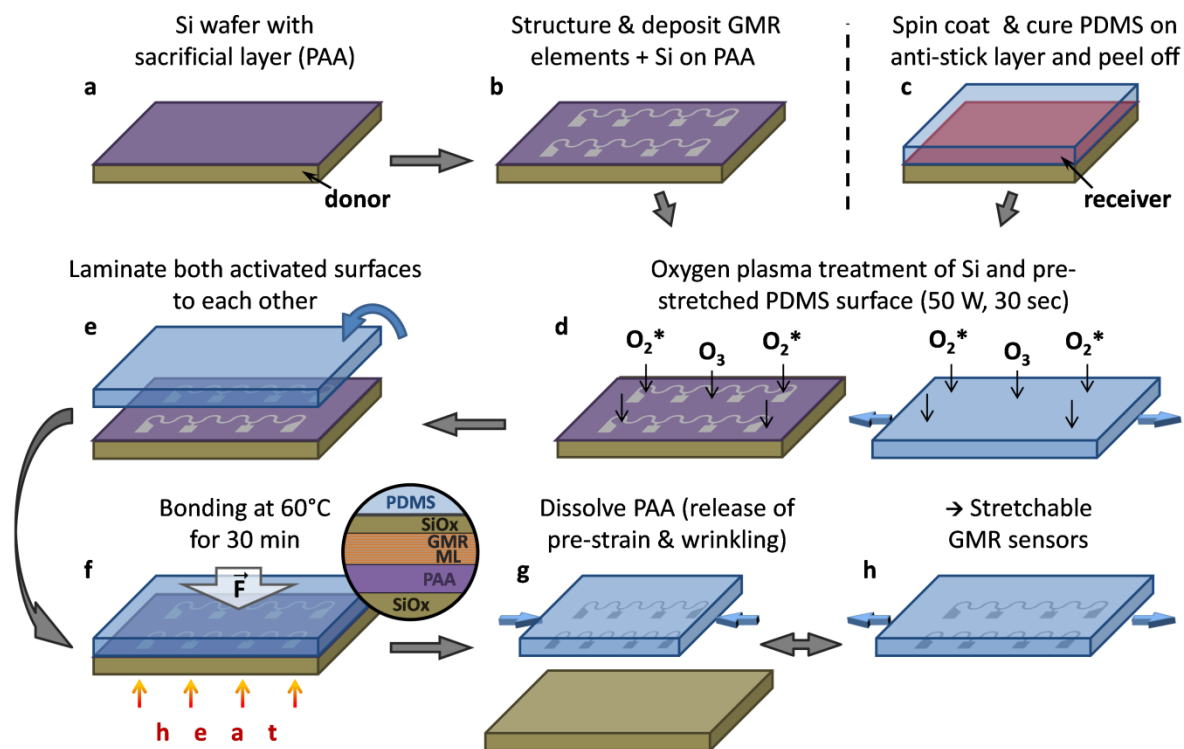


Figure 4.19 | Process flow of the direct transfer printing: (a,b) preparation of GMR multilayers with Si capping layer on a PAA coated Si wafer (donor). (c) Spin coating and curing of a PDMS film (receiver) on an anti-stick layer coated carrier. (d) Oxygen plasma activation of donor and pre-stretched receiver substrate. (e,f) Heat and pressure assisted adhesion of both activated surfaces. The magnified view in (f) shows a cross section of the bonding interface region. The bonding is established between the top Si surface, which is oxidized to SiO_x by the plasma and the activated PDMS (layers not drawn to scale). (g) Dissolving of the PAA sacrificial layer to detach the GMR structures from the donor substrate and release of the pre-strain in the receiver membrane to obtain a wrinkled morphology. (h) The transferred sensors can be elastically stretched in the direction of the pre-strain. The direct transfer process was developed in collaboration with Daniil Karnaushenko (IFW Dresden). Figure taken from [163].

Two different sensor designs were prepared in this study to highlight the two main features enabled by the introduced transfer process. The first layout is an array of micro-sized GMR sensors with electrical contacting, which requires two-step lithography to be performed, to demonstrate the enhanced fabrication potential in terms of miniaturization and level of complexity compared to previous fabrication approach. The second sensor design is a serpentine meander, to demonstrate the increased stretchability using the direct transfer method. The advantage of using the meander-shaped sensors is twofold: on the one hand this shape allows increasing the resistance of the sensor element, which is beneficial from the signal acquisition point of view and on the other hand they allow for an enhanced stretchability compared to the stripe-shaped metal layers^{29,145}. The results for both sensor structures are described in the following two sections, respectively.

4.3.2 Direct transfer of GMR microsensor arrays

The microsensor array consists of five GMR multilayer elements, all of $6\ \mu\text{m}$ width and different lengths, including one sensor shaped to a meander. As displayed in **figure 4.20a,b**, each element is equipped with an electrode structure of $\text{Cr}(5\ \text{nm})/\text{Cu}(50\ \text{nm})$ for reliable contacting, which was

prepared by electron beam evaporation and a second photolithographic patterning step. Since microsensor arrays are mainly used to detect spatially confined and small magnetic fields in the range of several oersteds only¹⁸⁸, the sensing elements in this design consist of highly sensitive $[\text{Py}/\text{Cu}]_{30}^{2\text{nd}}$ multilayers⁹⁵. Two of the sensor elements, a stripe of 60 μm length and the meander, are displayed in figure 4.20c,d, respectively.

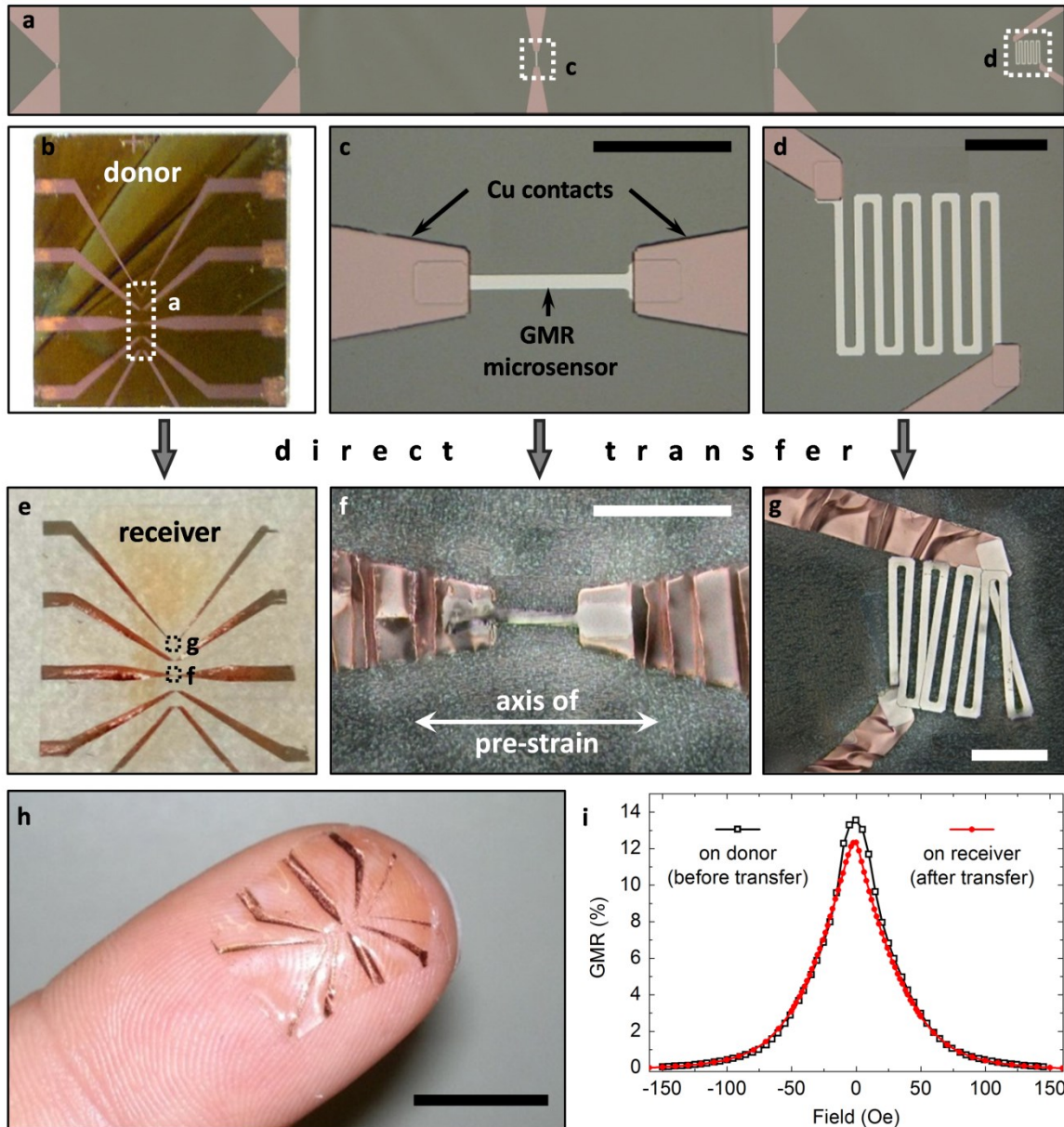


Figure 4.20 | Direct transfer of a GMR microsensor array: (a) Microscope image of the array of five $[\text{Py}/\text{Cu}]_{30}^{2\text{nd}}$ GMR elements (four stripes of different length and one meander, widths: 6 μm). (b) Entire structure including contacts on the rigid donor substrate. (c,d) Magnified views of the 60 μm microsensor stripe and the meander, with contacts to the electrodes, respectively. (e-g) Microsensors transferred to the receiving substrate using a uniaxial pre-strain of 20%, as indicated in (f). All scale bars: 50 μm . (h) The transferred microsensor array can conform to the soft and curved surface of a fingertip (scale bar: 10 mm). (i) GMR characteristics of the meander microsensor element before (\blacksquare) and after (\bullet) the transfer process. The lithographic structuring was performed in collaboration with Gungun Lin (IFW Dresden). Figure compiled from [163].

Figure 4.20e-g shows the same structures as above, respectively, after the transfer to the receiving PDMS membrane. For the microsensor array, a uniaxial pre-strain of 20% along the sensor stripes was used, as indicated in figure 4.20f. In the case of uniaxial pre-strain, the transverse direction has to be pre-stretched as well, in order to compensate for the Poisson's contraction, avoiding the destruction of transferred structures upon strain release. The final sensor array can be applied to any curved or soft surfaces, as demonstrated in figure 4.20h with the GMR microsensors situated on a fingertip. The functionality of the transferred sensors is proven by GMR measurements on the meander element before and after the transfer process (figure 4.20i). Both curves show a similar GMR signal with high sensitivities for small magnetic fields.

4.3.3 Direct transfer of compliant meander shaped GMR sensors

As the second sensor design, the macroscopic serpentine meander with four contact pads, according to figure 3.3b, was used. In this case, $[\text{Co}/\text{Cu}]_{50}^{\text{st}}$ GMR multilayers were chosen. **Figure 4.21a,b** shows the same element before and after the transfer to the receiving PDMS membrane, respectively, using a biaxial pre-strain of 25% x 25%. A confocal microscopy image of the serpentine trace after the transfer is included in figure 4.21c showing the biaxially wrinkled morphology of the GMR film with an amplitude of $\approx 2.5 \mu\text{m}$ and a period of $\approx 11.7 \mu\text{m}$. The theoretically estimated value of the wrinkling period according to the previously employed model by Bowden *et al.*²⁴, is $\lambda = 22.3 \mu\text{m}$, if the 4 nm plasma oxidized silicon layer ($E_{\text{SiO}_2} = 73 \text{ GPa}$ and $\nu_{\text{SiO}_2} = 0.17$) is also taken into account. This value, however, gives only the period of the wrinkles upon their formation and has to be corrected for the compressive deformation of the rubber support upon relaxation, which pushes together the buckles accordingly. For the chosen pre-strain of 25% along one direction, there is a resulting compression of 0.2, which shrinks the calculated wrinkling period to $\lambda = 17.8 \mu\text{m}$. It is known, that oxygen plasma treatment creates a stiff film of the surface of PDMS¹⁷⁷. This layer of increased but unknown Young's modulus, which is not included in this theoretical reflection, may be responsible for the somewhat smaller value of the wrinkling period that is observed experimentally.

The good adhesion of the plasma induced bonding between the GMR multilayer and the PDMS membrane is demonstrated by means of an SEM investigation of the sensor cross-section (figure 4.21d). The cross-section was prepared using FIB etching through the wrinkled magnetic nanomembrane. The images show that the GMR multilayer is firmly attached to the soft PDMS, even throughout the wrinkles. The magnetoelectrical performance of the $[\text{Co}/\text{Cu}]_{50}^{\text{st}}$ multilayer meander on the donor and the receiver substrate is shown in figure 4.21e. The GMR curve determined in this measurement reaches a value of 46% after the transfer from 57% beforehand. This, however, is not an evidence of a reduced total GMR magnitude in the transferred sensor element, since it also reveals an increased saturation field that is beyond the maximum field range of $\pm 5 \text{ kOe}$ achievable in the magnetoelectric characterization setup. This broadening of the GMR curve is attributed to the appearance of out-of-plane components of the magnetization at the locations of the tilted wrinkle side-

walls, which run perpendicular to the applied magnetic field. This effect becomes pronounced in this sample due to the large amplitude of biaxial wrinkles (amplitude/period = 0.4) compared to the previous cases with rather shallow parallel wrinkles (amplitude/period = 0.04), which were thermally induced⁶. A similar effect was already observed by means of perpendicular buckles due to the Poisson contraction in the case of stretchable spin valves¹⁶⁷ described in chapter 4.2.4.

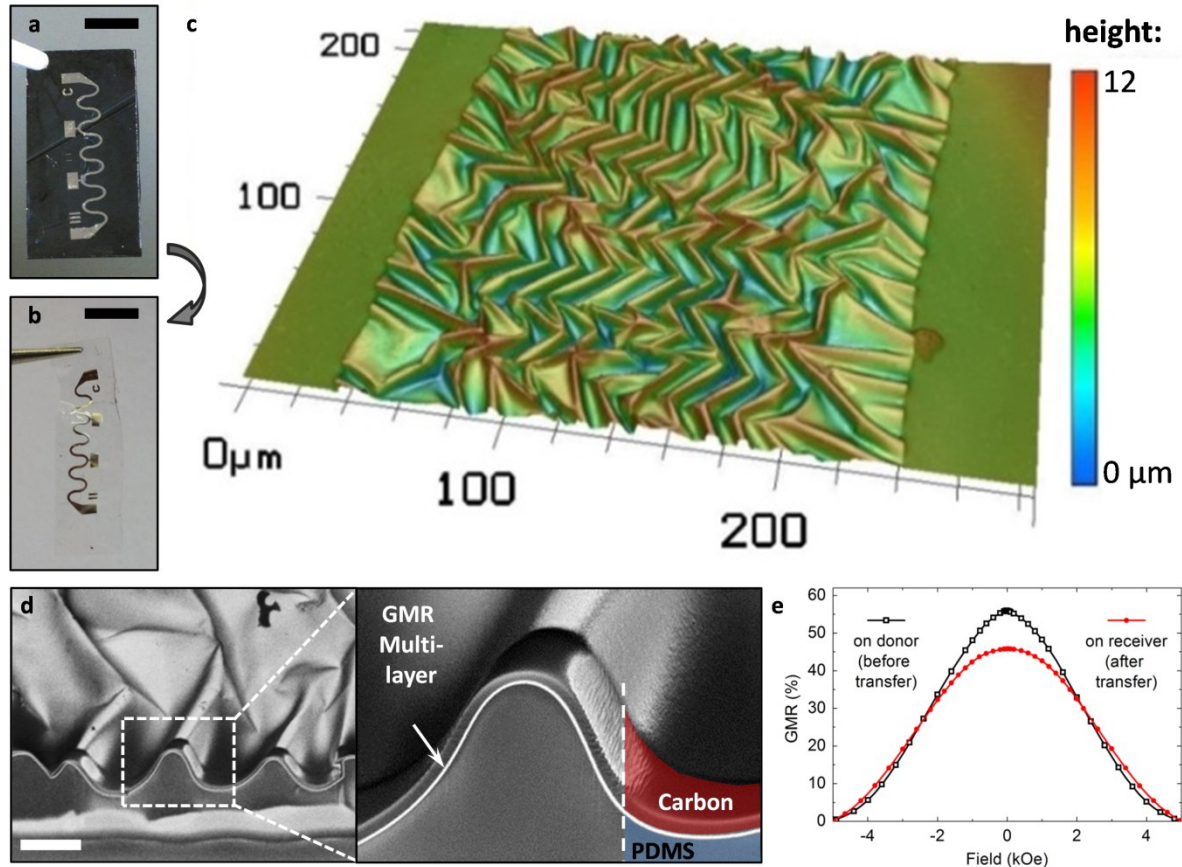


Figure 4.21 | Direct transfer of a compliant meander GMR sensor: (a) A macroscopic serpentine meander element consisting of a $[\text{Co}/\text{Cu}]_{50}^{\text{st}}$ GMR multilayer on the donor substrate. (b) The same meander element after the transfer to a free-standing PDMS membrane using a biaxial pre-strain of 25% x 25%. All scale bars: 5 mm. (c) A confocal microscopy image showing the topography of the wrinkled GMR multilayer element in (b). (d) SEM images of a FIB cut through the transferred GMR film showing the good adhesion of the wrinkled magnetic nanomembrane to the PDMS support (scale bar: 5 μm). (e) GMR characteristics of the serpentine meander before (\blacksquare) and after (\bullet) the transfer process. FIB milling and SEM investigation was performed in collaboration with Dr. Stefan Baunack (IFW Dresden). Figure compiled from [163].

The chosen meander geometry of the transferred sensing elements have been shown to enhance the stretchability of GMR multilayers grown onto PDMS substrates¹⁴⁵. Hence, this type of sensor will be applied to demonstrate the increased stretchability achieved using the direct transfer printing method with mechanically induced pre-strain. Its larger size is beneficial for performing stretching experiments as the evaluation of strain on the magnetoresistive elements and its influence on their sensing behavior is more meaningful than for microscopic sensors.

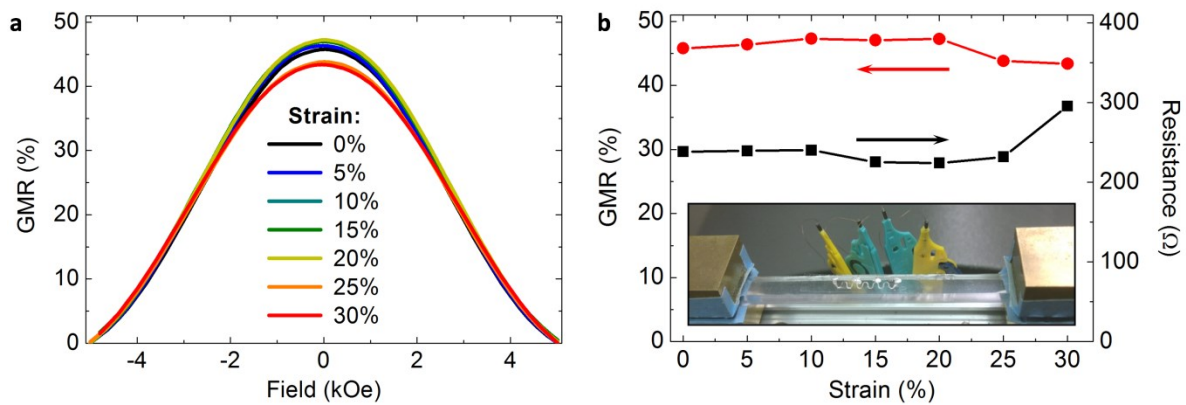


Figure 4.22 | Stretching test of a transferred GMR meander: (a) GMR curves of a $[\text{Co}/\text{Cu}]_{50}^{\text{1st}}$ multilayer meander transferred to a PDMS membrane, measured at different strains applied along the meander, as indicated in the legend. The pre-strain used for the transfer process was 25% x 25%. (b) GMR magnitude (●) and sensor resistance (■) with increasing tensile strain. The inset shows the sensor mounted to the stretching stage and contacted for 4-point *in situ* GMR characterization. Figure compiled from [163].

A transferred GMR meander element was mounted to the computer controlled stretching stage, as shown in the inset of **figure 4.22b**. The sensor characteristics for *in situ* recording of GMR curves as the sample is stretched is plotted for increasing strains in figure 4.22a and shows no significant changes, except for a small drop beyond 20% strain. In figure 4.22b the GMR magnitude and the sensor resistance at zero field is presented in dependence of the applied tensile strain. Both values are subjected to only small changes up to a uniaxial deformation of the sensor of 30%, before the electrical connection is lost. This data demonstrates the compliant properties and invariance of the prepared magnetic sensing elements to application relevant tensile deformations. Especially the maintained resistance, in contrast to the behavior of the spin valves in section 4.2.3, proves that no or only very few cracks are induced in the wrinkled GMR nanomembrane as it expands. The obtained stretchability of 30% is attributed to a combination of the wrinkling due to mechanically induced pre-strain in the stretching direction ($\approx 25\%$) and the additional compliance of the meander pattern ($\approx 5\%$)¹⁴⁵.

In conclusion, a novel fabrication process for stretchable magnetoelectronics was introduced, relying on a single step direct transfer of thin functional elements from a rigid donor substrate to a mechanically pre-stretched elastic membrane. The detachment of magnetic nanomembranes from the donor substrate is facilitated by means of a PAA-based sacrificial layer. To assure a good adhesion to the receiving PDMS elastomeric membrane, an oxygen plasma treatment of the capping Si surface of the sensor, on the one hand, and the pre-stretched PDMS membrane is found to be absolutely crucial. Although the individual fabrication steps, *e.g.* use of sacrificial layers¹⁷³ or plasma treatment are already known, the key novelty of the present approach comes from the combination of different processing steps and materials in exactly the right order to obtain a fabrication route that allows for the superior properties of stretchable magneto-electronics. The fabrication potential of this method in terms of miniaturization and level of complexity was demonstrated by transferring an entire GMR

microsensor array including contact structures in a single step. On the other hand, the stretchability of transferred GMR multilayer elements is presented up to strains of about 30% relying solely on the wrinkled topography and the meander geometry, *without the formation of cracks*. These results denote a one order of magnitude increase in stretchability and miniaturization of compliant GMR multilayers compared to the previously described approach of sensor preparation directly onto the elastomeric substrate with thermally induced pre-strain^{6,145}. Both, the GMR characteristic and sensor resistance remain almost unchanged over the entire range of strain, which was not achieved by any other means so far. Since almost no resistance change is associated with the tensile deformation as well, the sensor elements introduced here are truly strain invariant. Although an unchanged resistance up to high tensile deformations was also observed in the case of stretchable spin valves after the first stretching, a severe damage occurred, when these elements were released back to their fully relaxed state¹⁶⁷. This effect is neither observed nor expected in the present case, due to the absence of cracks in the functional GMR layer. Furthermore, the direction of the pre-strain can be controlled in order to achieve either uniaxial or biaxial stretchability. The presented direct transfer approach is not limited to magnetic nanomembranes, which renders possible the combination of magnetoelectronic components with other stretchable functional elements to form smart multi-functional and interactive electronic systems triggered by magnetic fields.

4.4 Imperceptible magnetoelectronics

In order to go beyond the possibilities provided by using elastomeric membranes like PDMS as support for GMR thin films to obtain arbitrarily shapeable sensing elements, the novel approach of *imperceptible electronics*¹⁶ is exploited. In this respect, ultra-thin GMR sensor foils that are extremely flexible, light-weight and durable are introduced. This work has a particular impact for *electronic skin* systems, which will be highlighted in the first part of this subchapter. The here presented imperceptible magneto-sensitive elements readily conform to ubiquitous objects, which paves the way to go beyond the imitation of natural skin functionalities and could equip the recipient with the “*sixth sense*” of *magnetoception*^{83,84}. Biological skin is soft and flexible but also stretchable, a feature that is most desirable for the artificial equivalent. The prepared GMR foils also lead to outstanding uniaxial and biaxial stretchabilities of far beyond 100% with a very stable performance and long-term persistence, which will be demonstrated in the second part of the chapter. These ultrathin magnetic field sensors offer new functionalities not only for electronic skin devices but also in the fields of soft robotics, safety and healthcare monitoring and consumer electronics. Their application potential is highlighted in several demonstrators throughout this section.

4.4.1 GMR multilayers on ultra-thin PET membranes

Imperceptible electronics relies on the fabrication of functional thin film electronic elements on ultra-thin (<2 μm) polymeric membranes. The reduction of the flexible substrate to a minimum thickness imparts its thus gained mechanical properties of extreme bendability and light-weight to the entire

electronic device¹⁶. Weight and flexibility are key figures of merit for large area electronics or robotic skin^{16,53}, as they critically influence the mechanical response and perception of the artificial system. The unique haptic character of functional electronic devices obtained using this approach allows for intimate contact with soft, biological tissue or organs and complex, arbitrarily shaped 3D free forms. Both, organic and inorganic electronic components were very recently introduced in this respect. Besides electronic circuitry⁵⁵ also tactile sensors,¹⁶ light emitting diodes,³⁸ solar cells,⁴⁸ as well as thermoelectric elements⁴⁵ have been realized.

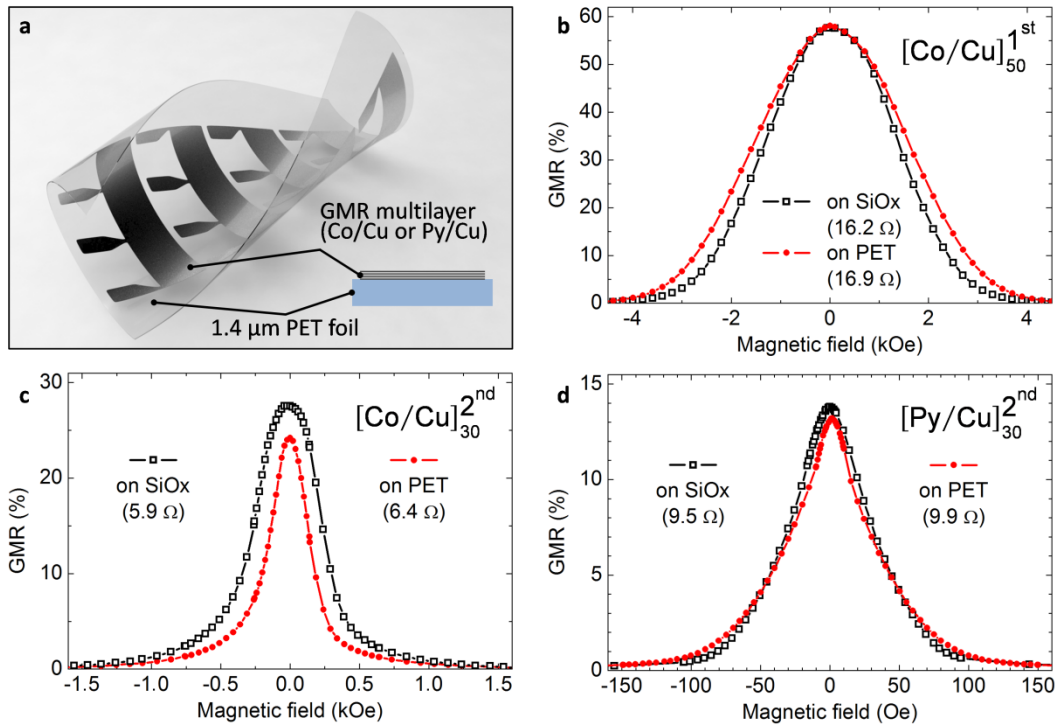


Figure 4.23 | GMR multilayers on ultra-thin PET: (a) Schematics of an imperceptible magnetic sensor foil with a cross section of the GMR layer system (inset). (b,c,d) GMR curves recorded on the PET substrate (●) as well as on SiOx reference wafers (■) for [Co/Cu]₅₀^{1st}, [Co/Cu]₃₀^{2nd} and [Py/Cu]₃₀^{2nd} GMR multilayers, respectively. The electrical resistances at zero field are included in the respective legends. Artwork in (a) by Dmitriy Karnaushenko. Figure compiled from [7].

In this work, GMR multilayer elements were fabricated on ultrathin (1.4 μm) PET membranes, as schematically shown in **figure 4.23a**. The substrate foil, which is commodity scale and commercially available, was attached to a handling support according to the description given in section 3.1.8. As for all sensor elements discussed in this work so far, magnetron sputter deposition at room temperature was performed to prepare different stacks of GMR multilayers with the approved sensor stripe geometry defined by photolithography. Despite the high surface roughness of the PET foil (29 nm according to the AFM investigation in figure 3.12) the prepared [Co/Cu]₅₀^{1st} sensor elements reveal a typical GMR ratio of 57.8% at room temperature (figure 4.23b). Also the electrical resistance is only slightly increased on the PET membrane (16.9 Ω compared to 16.2 Ω on a smooth and rigid SiOx wafer) due to roughness. Since the morphology of the ultra-thin polymeric sheet is governed by isolated hillocks (figure 3.12) the main part of the surface area is still smooth enough to facilitate high

GMR ratios without occurrence of the orange peel effect. Moreover, one can take advantage of the enhanced adhesion of thin metal films on rough polymer surfaces¹⁶, which leads to an improved mechanical resilience. Motivated by these results, also $[\text{Co}/\text{Cu}]_{30}^{2\text{nd}}$ and $[\text{Py}/\text{Cu}]_{30}^{2\text{nd}}$ GMR multilayer elements were prepared on ultrathin PET foils, which also behave very similar to their rigid counterparts, as revealed by their magneto-electric characterization shown in figure 4.23c,d, respectively. These GMR systems have more stringent requirements with respect to substrate quality, but exhibit much higher sensitivities to small magnetic fields^{95,166}. This is especially desirable for smart skin, biomedical and orientation applications^{196,199} and also strengthens the potential of imperceptible magnetoelectronics for a wide field of GMR applications.

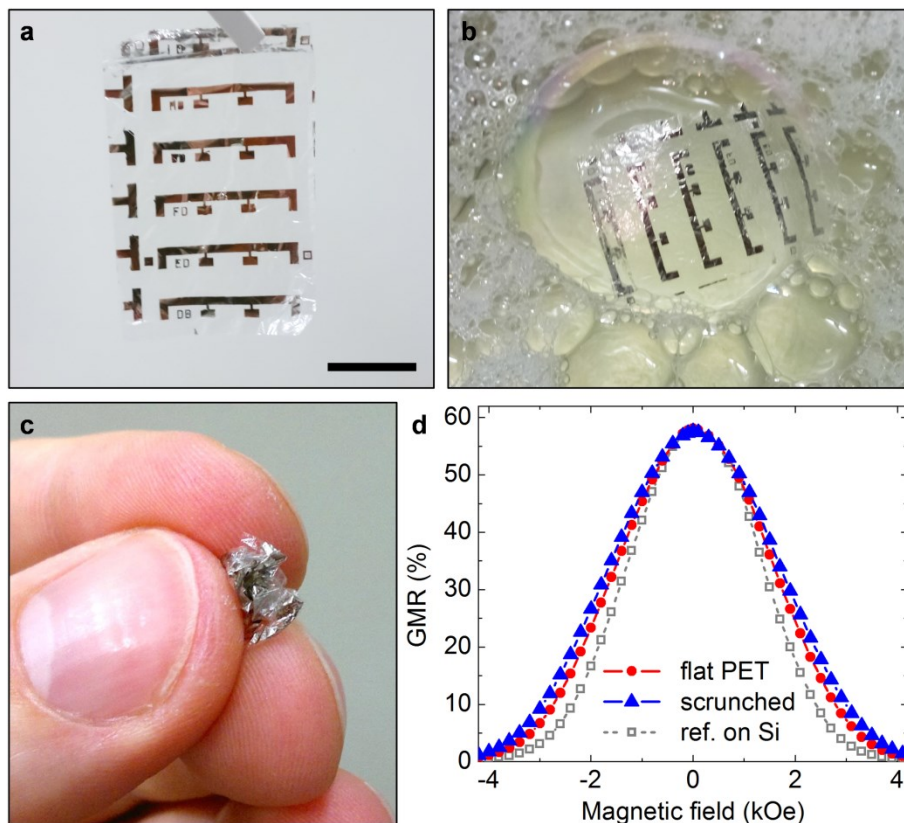


Figure 4.24 | Ultra-thin and light-weight GMR sensors: (a) Free-standing array of five $[\text{Co}/\text{Cu}]_{50}^{1\text{st}}$ multilayer elements on 1.4 μm -thick PET foil (scale bar: 10 mm). (b) The ultralight ($\approx 3 \text{ g}/\text{m}^2$) sensor array floating on a soap bubble and (c) scrunched between fingertips. (d) GMR characteristics of one $[\text{Co}/\text{Cu}]_{50}^{1\text{st}}$ element as-prepared (\bullet , $R_0 = 16.9 \Omega$), after crumpling as shown in (d) (\blacktriangle , $R_0 = 17.9 \Omega$) and a comparison to a reference sample on rigid silicon (\blacksquare , $R_0 = 16.2 \Omega$). Samples were prepared in collaboration with Martin Kaltenbrunner (University of Tokyo). Figure compiled from [7].

After device fabrication, the magneto-sensitive membrane is readily peeled off the handling support without causing damage. **Figure 4.24a** shows a free standing ultra-thin (1.5 μm total thickness) array of five lithographically structured $[\text{Co}/\text{Cu}]_{50}^{1\text{st}}$ GMR multilayer elements. The extreme light-weight and compliant nature of the sensor elements is demonstrated in figure 4.24b where an array of magnetic field sensors is floating on a soap bubble. The sensor foil is highly flexible and tearproof; it can be

completely scrunched up and rubbed between fingertips multiple times, as shown in figure 4.24c, without signs of performance degradation. This is corroborated by GMR characteristics (figure 4.24d) recorded for the as fabricated sensor and after crumpling, showing that even severe mechanical wear has virtually no influence on the device characteristics.

4.4.2 Imperceptible GMR sensor skin

Magnetoception is a sense which allows bacteria, insects and even vertebrates like birds and sharks to detect magnetic fields for orientation and navigation^{83,84}. Humans are however unable to perceive magnetic fields naturally. Magnetosensorics is a versatile tool to assess orientation or mechanical movements that should become wearable on-skin and may also be operated *in vivo* in order to add these unfamiliar senses to our natural cognition. Foreseeable applications include real time monitoring of artificial muscles, joints or valves of the heart to diagnose early stages of dysfunctions. Such advanced applications require very specific mechanical properties of the sensing elements, such as bending radii smaller than 10 μm , stretchabilities exceeding 100% as well as a sensitivity for magnetic fields below 100 Oe. Such a compliant nature makes magnetoelectronic devices ideally suited also for wearable, yet unobtrusive and imperceptible orientation and manipulation aids.

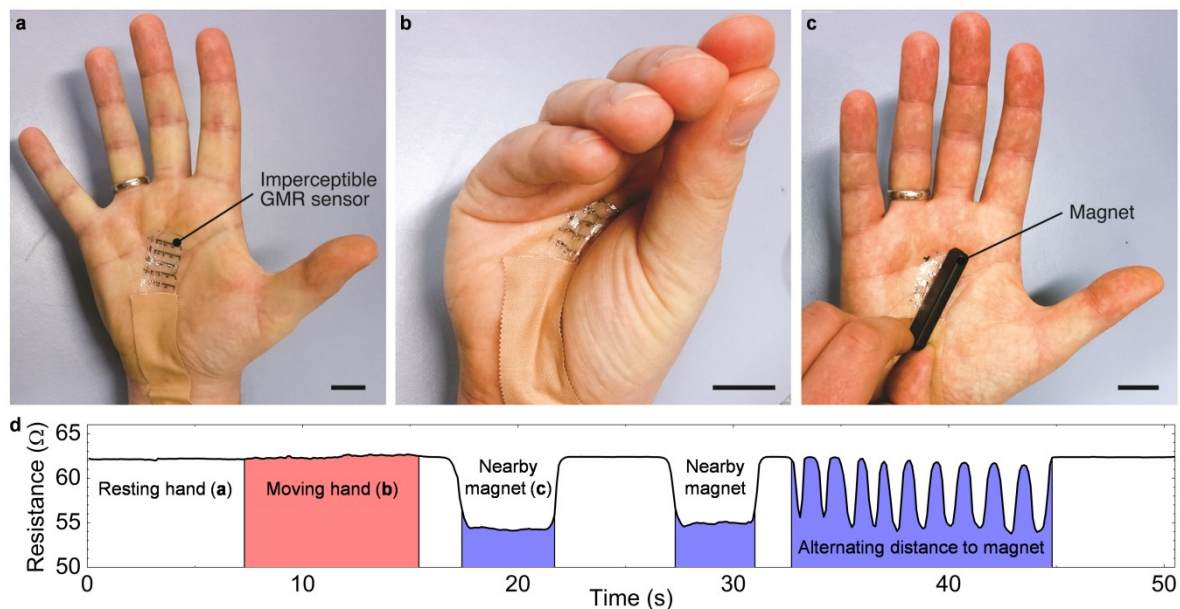


Figure 4.25 | Imperceptible GMR sensors: (a-c) Imperceptible $[\text{Co}/\text{Cu}]_{50}^{\text{1st}}$ GMR sensor array on a human palm with one element connected to a readout circuit during rest, moving the hand and in proximity to a permanent magnet, respectively. All scale bars: 20 mm. (d) recorded resistance of the sensor element for panels (a) through (c). This experiment was conducted in collaboration with Daniil Karnaushenko (IFW Dresden). Figure taken from [7].

Imperceptible magnetoelectronic elements are readily worn directly on the palm of the author's hand as demonstrated in **figure 4.25**. Here, a set of five $[\text{Co}/\text{Cu}]_{50}^{\text{1st}}$ GMR sensors intimately conforms to the inner hand and simultaneously follows the motions and deformations of the skin when the hand is moved (figure 4.25a,b). The presented elements are denoted imperceptible, because their presence on

the skin is haptically not perceived by the recipient. One sensor element is electrically contacted with thin copper wires and the resistance of the on-skin sensor is recorded while moving the fingers, opening and closing the hand, applying a magnetic field with a permanent magnet and alternating the distance to the magnet (figure 4.25c). The recorded signal plotted in figure 4.25d shows a small, noise-induced fluctuation during the motion of the hand (which amounts to less than 0.3%), whereas the field of the approaching permanent magnet induces a strong resistance drop of about 13% at its nearest position. Altering the distance between the permanent magnet and the on-skin GMR element results in a corresponding change in the sensor's resistance. Note that magnetic saturation of the $[\text{Co}/\text{Cu}]_{50}^{\text{1st}}$ multilayer element is not reached, as the full bandwidth of the sensor is not utilized here.

With just about 1.5 μm total thickness, the prepared magneto-electronic foils are light ($\approx 3 \text{ g/m}^2$) and unmatched in flexibility, they are operable with smallest radii of curvature, yet highly durable and withstand severe crumpling without any performance degradation. Despite their imperceptible design, these novel GMR sensors exhibit the same sensitivities as their counterparts on rigid Si/SiO_2 wafer substrates. Due to their unconventional mechanical properties, they can dynamically conform to arbitrary surfaces, including human skin, and seamlessly follow deformations or distortions without performance degradation. As ready-to-use epidermal sensing elements, they extend the cognition of electronic skin systems to a medium that by no means can be naturally detected by human beings. These intriguing capabilities will be demonstrated in the following paragraph.

4.4.3 Demonstrator: Fingertip magnetic proximity sensor

Electronic skin on fingertips²¹⁴ is especially attractive for precise input and as communication interfaces due to our finger's fine motor skills. In **figure 4.26** an on-skin magnetic proximity sensor is demonstrated where a single imperceptible $[\text{Co}/\text{Cu}]_{30}^{\text{2nd}}$ GMR element is attached to a fingertip and connected to a read out circuit (section 3.2.4 for details of the signal acquisition and conditioning electronics). The presence of any kind of magnetic field can thus be detected by simply pointing the finger towards it, and its strength is in this case visualized by an array of LEDs (figure 4.26a-c). Unlike optical sensors, no line-of-sight between the sensor and the magnetic field emitter is required. This allows transmitting "magnetic messages" through all non-magnetic objects like safety enclosures, displays or even walls. The encoding can be realized both statically via permanent magnets as well as dynamically simply with current driven wirings. In all those demonstrations, the imperceptible GMR sensors require no encapsulation or capping layers.

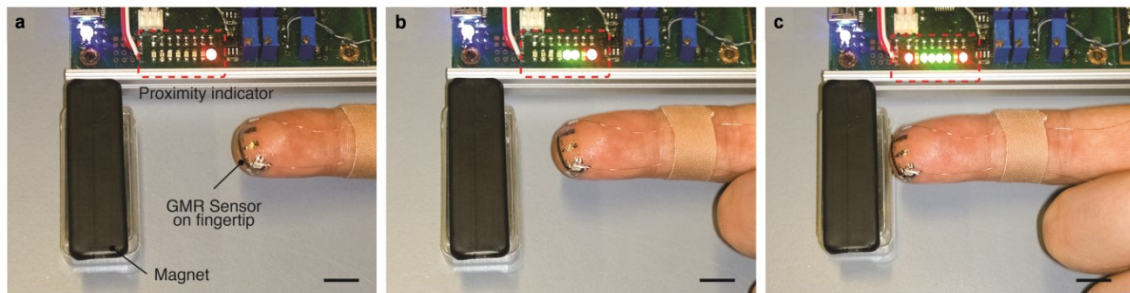


Figure 4.26 | Fingertip magnetic proximity detector: (a,b,c) Imperceptible $[\text{Co}/\text{Cu}]_{30}^{2\text{nd}}$ sensor element on the fingertip connected to a linear array of LEDs (dashed red frame). All scale bars: 10 mm. Experiment conducted in collaboration with Daniil Karnaushenko (IFW Dresden). Figure taken from [7].

The demonstrated on-skin proximity detection system is a proof of concept for touch-less human-machine interaction relying on imperceptible magneto-electronics. Similar approaches for motion and displacement sensorics are applicable for soft robots^{69,79} or functional medical implants^{65,67} as well as for magnetic functionalities in epidermal electronics⁵³.

4.4.4 Ultra-stretchable GMR sensors

Artificial skin components should not only be flexible, but also elastic and ideally even withstand high biaxial deformations. Although the used ultra-thin PET foil is hardly stretchable itself, imperceptible electronics offers an elegant route to facilitate very high levels of tensile strain without any sacrifices in device performance by a facile post-fabrication transfer step onto a pre-strained elastomer^{16,38,48}. In the case of GMR elements, this leads to magnetic sensing devices that can reversibly attain nearly a 10-fold of stretch deformations compared to the previously described concepts, with remarkable long-term stability. Furthermore, the magneto-sensitive elements can be prepared to be compliant to uniaxial or biaxial a deformations, which highlights their universal application potential for stretchable electronic systems.

Individual elements of imperceptible GMR sensor foil are laminated onto pre-stretched stripes of highly stretchable VHB tape, as illustrated in **figure 4.27a**. Its strongly adhesive surface allows for an easy transfer of the ultra-thin PET foil from the handling support. When the rubber tape is allowed to relax, out-of-plane wrinkles are formed not solely in the GMR thin film, but in the entire imperceptible sensor foil (*i.e.* GMR layer + ultra-thin PET membrane), instead. This not only enables the stretching of the device along the direction of the initial deformation of the supporting tape, as in previous cases. The presence of a thin flexible, but not stretchable polymer membrane supports the delicate GMR nanomembrane throughout its corrugations and protects it from high mechanical stresses during arbitrary deformations of the sensor device, which allows for very high stretchabilities. The maximum compression and therefore stretchability of the sensors is mainly determined by the pre-strain magnitude of the elastomer along the respective direction before lamination and limited by the packing density of the out-of-plane folds¹⁶. In order to test the limits of the uniaxial stretchability for the specific combination of materials studied here, large pre-strains of 600% were used for the fabrication

of compliant devices. For such high pre-strains, the VHB tape is unable to relax back to its initial length upon release, as adjacent buckles start to push against each other. Optical microscopy and SEM top view images provided in figure 4.27b,c respectively, reveal the highly wrinkled topography of the sensors after the relaxation of pre-strain. Due to the viscoelastic behavior of the VHB tape, the length of the sensor elements after a relaxation period of at least one day is defined as the reference length in stretching experiments, which corresponds to 0% strain.

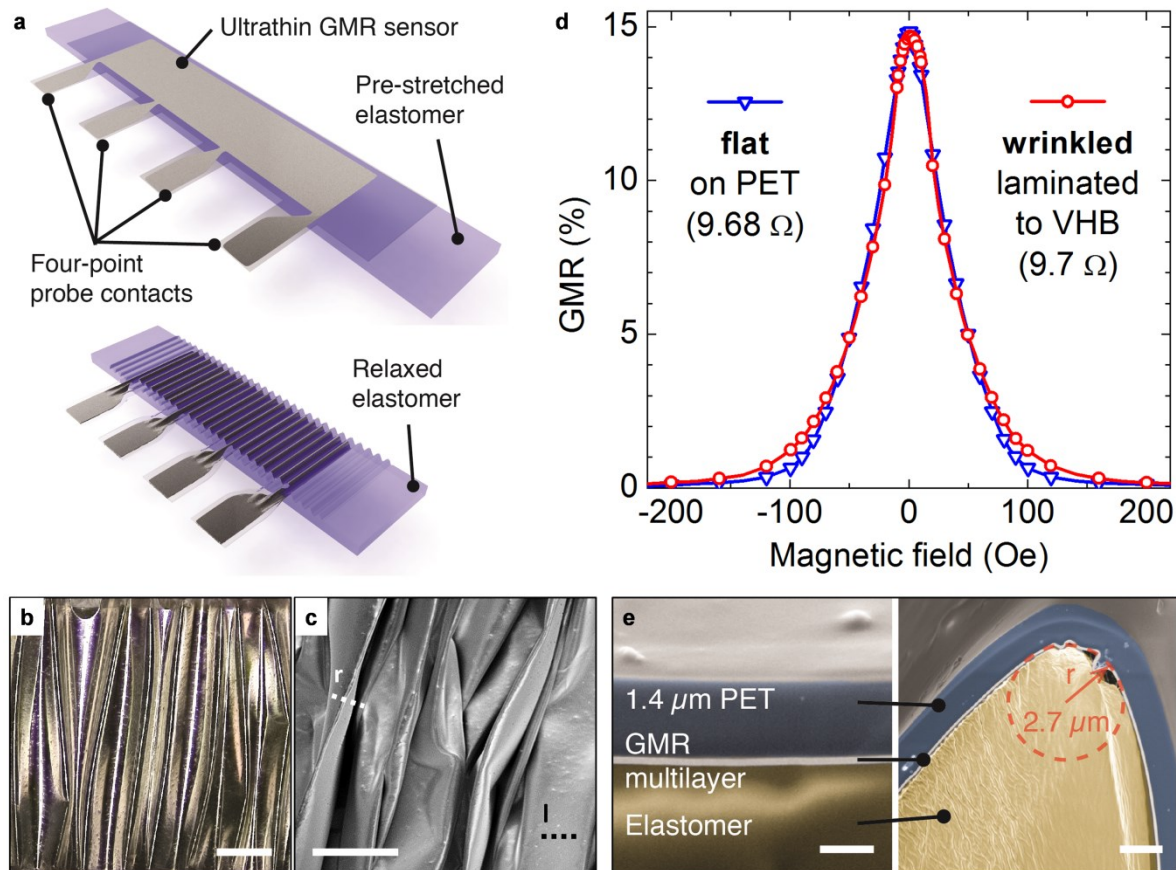


Figure 4.27 | Lamination of imperceptible GMR multilayers onto pre-stretched adhesive tape: (a) The post fabrication step to obtain ultra-stretchable GMR sensors from imperceptible elements by face-down lamination onto a highly pre-stretched stripe of VHB tape. Four contact pads are reaching beyond the tape (top). Relaxing the elastomer results in out-of-plane wrinkling of the sensor foil and enables re-stretching (bottom). (b,c) Optical microscopy (scale bar: 200 μm) and SEM (scale bar: 100 μm) top view images, respectively, revealing the wrinkled structure of the sensor surface in the relaxed state. (d) GMR curves of an imperceptible $[\text{Py}/\text{Cu}]_{30}^{\text{nd}}$ multilayer element at a flat state before lamination onto the pre-stretched VHB support (∇) and at a highly wrinkled state after release of pre-strain (\circ). (e) Cross-sectional SEM images of a $[\text{Co}/\text{Cu}]_{50}^{\text{st}}$ sensor foil laminated to the rubber tape. The GMR nanomembrane is encapsulated between the ultra-thin PET and the stretchable adhesive tape. Some parts of the magnetoresistive foil on the tip of the buckles are bent into radii of curvature of less than 3 μm (right). The location of cuts shown on the left and right is indicated in (c). Scale bars: 1 μm left, 2 μm right. Artwork in (a) by Dmitriy Karnausenko, FIB milling and SEM investigation was performed in collaboration with Dr. Stefan Baunack (both IFW Dresden). Figure compiled from [7].

The magneto-sensitive capabilities of the presented elements are not affected by the post-processing, as shown in figure 4.27d on the example of a $[\text{Py}/\text{Cu}]_{30}^{\text{nd}}$ multilayer device measured before and after the lamination and wrinkling on the VHB tape. The GMR elements are laminated face down to the

pre-stretched VHB tape, which in turn acts as an encapsulation for the functional magnetic layer between the stretchable tape and the ultra-thin PET foil, as visualized by SEM imaging of the sample's cross-section (figure 4.27e) prepared by FIB milling. In order to realize reliable contacting of the buried GMR layer, the approved sensor layout was adapted by elongated contact pads that after the lamination reach sideways beyond the stretchable tape (figure 4.27a). Hence, contacting to thin copper wires was done on the metalized bottom side of the free waving PET foil using conductive silver paste.

The cross-sectional SEM images of samples prepared with a high uniaxial pre-strain presented in figure 4.27e reveal, that some parts of the magnetoresistive foil on the tip of the buckles are bent into radii of curvature of less than 3 μm , while the sensor not only remains functional, but also maintains its full performance. For an approximation of the peak strain in the wrinkled PET/GMR membrane, the model for the bilayer bending strain¹³⁴ discussed in section 2.3.6 can be applied. The associated equation (2.13) computes the maximum lateral strain ε_b in a stiff film (elastic module: E_f , thickness d_f) on a softer substrate (elastic module: E_s , thickness d_s) upon bending to a radius R_b . The elastic modulus of the $[\text{Co}/\text{Cu}]_{50}^{\text{st}}$ GMR layer ($d_f=111$ nm) is again set to be $E_f = 171$ GPa by its material composition, as assumed in section 4.1.2. The properties of the PET foil are $E_s=3$ GPa and $d_s=1,400$ nm. For the measured radius of curvature of 3 μm in the relaxed (*i.e.* fully wrinkled) state, the calculated strain on the GMR film is about 5.6%. In the case of expansive deformation (*i.e.* in the valleys of the wrinkled film), this value is above the fracture strain of the GMR layer. Different effects are considered to reduce the actual strain, *e.g.* an increased strength observed in multilayer thin films¹³⁶ or the shifting of the neutral mechanical plane¹³⁴ closer to the active element by the sandwiching VHB elastomer. In addition, for the case of compressive strain on the GMR layer underneath the buckles, the FIB cut presented in figure 4.27e revealed further microscopic wrinkling of the magnetic nanomembrane on the PET to accommodate the bending stress. Beyond that, a much lower curvature in the wrinkle valleys can be observed (figure 4.27c), which would also reduce tensile strains. A maximum peak strain of 0.5% in the GMR layer would allow a bending radius of below 40 μm according to (2.13). The locations of the presented FIB cuts are marked in the top view SEM image in figure 4.27c.

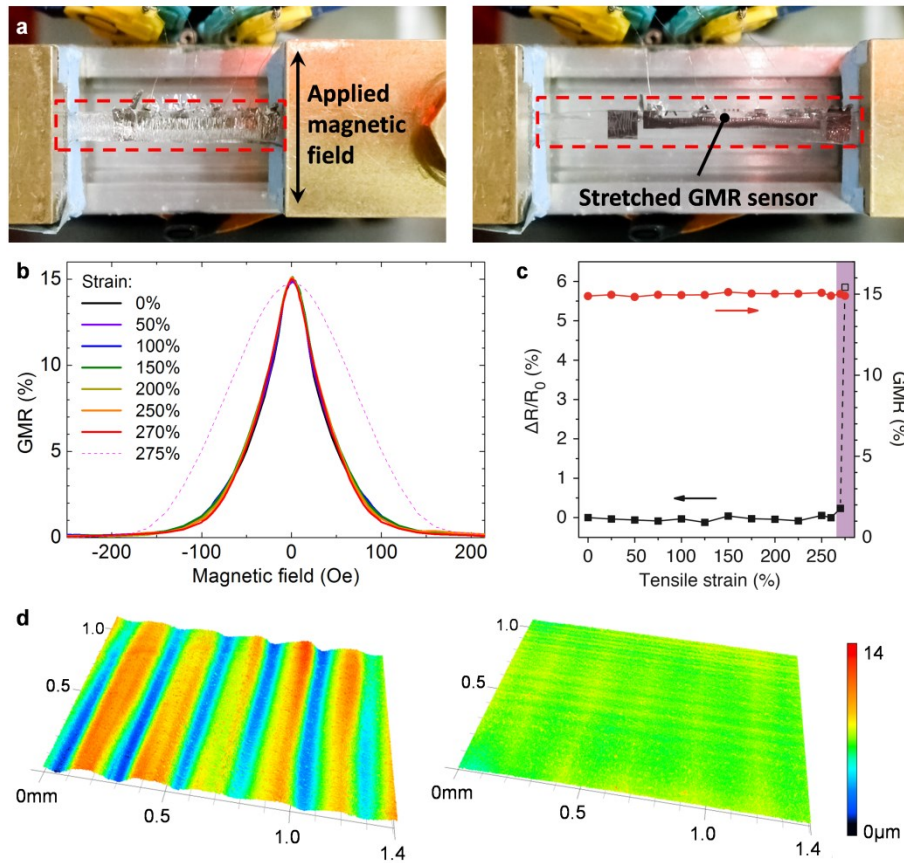


Figure 4.28 | Stretching of imperceptible GMR sensors: (a) A $[\text{Py}/\text{Cu}]_{30}^{2\text{nd}}$ sample mounted to the *in situ* stretching stage relaxed (left) and fully elongated (right). The arrow in the left image indicates the axis of the applied magnetic field. (b) GMR curves recorded for strains from 0% to 250% in increments of 50%, plus 270% and 275%, according to the legend. (c) ● GMR magnitude and ■ resistance change normalized to 0% strain ($R_0 = 9.7 \Omega$) as a function of applied strain. The shaded region indicates overstretching. (d) 3D confocal laser scanning micrographs showing the topography of the stretchable GMR sensors's surface (metalized side up) at a stretched state just before reaching the maximum strain (left) and precisely at the maximum strain, above which the resistance starts to increase (right). Figure compiled from [7].

The stretchability of the post processed sensor elements is investigated in the GMR characterization setup with *in situ* stretching stage. A top view of a mounted and contacted stretchable $[\text{Py}/\text{Cu}]_{30}^{2\text{nd}}$ GMR sensing element in a relaxed (left) and the fully stretched state (right) is provided in **figure 4.28a**. The axis of the applied magnetic field is perpendicular to the sensor stripe (along the wrinkles). The strain was increased in steps of 10% with a rate of $100 \mu\text{m/s}$ (0.7 %/s) between the magnetoelectric measurements. The recorded GMR curves at different tensile strain levels up to 270% along the direction of pre-strain are congruent with each other, as presented in figure 4.28b. The progression of the GMR magnitude and the relative resistance change due to stretching of the sensor are plotted as a function of the uniaxial deformation in figure 4.28c. Both values also remain unchanged over this entire strain regime (relative standard deviations: $RSD_R < 0.1\%$; $RSD_{\text{GMR}} < 0.6\%$). At 270%, the PET foil with the GMR layer is fully elongated and the wrinkles vanish, as shown in the

right hand picture of figure 4.28a. Confocal microscopy images of a sample at the maximum strain and just below are also included in figure 4.28d. Once the foil is stretched even slightly beyond its fully flat state, the resistance rapidly increases due to some ultimate tensile deformations of the flattened GMR layer (shaded region in figure 4.28c). Surprisingly, by overstretching the GMR element by several percent, here from 270% to 275%, the magnitude of the GMR effect is not reduced. The respective GMR curve for the overstretched sensor, shows a significant increase of its saturation field instead (figure 4.28b), which may be due to a modification of the interlayer exchange coupling by slightly reduced layer thicknesses in the strained GMR film. This effect, however, is fully reversible and the reduced saturation field is restored as soon as some strain is released.

To investigate the long-term behavior and reliability of the imperceptible, highly stretchable magnetoresistive elements upon deformation, cyclic loading experiments were performed. Wrinkled $[\text{Py}/\text{Cu}]_{30}^{\text{nd}}$ multilayer sensors were prepared, as described, using a pre-strain of 150% for lamination. The strain interval for the repeated loading and unloading was set from 50% to 100% to meet the maximum permanent operation limits of the test setup and to avoid slacking due to the strong viscoelasticity of the rubber tape during this long-term test. The here investigated magnitude of strain meets the typical demands for most on-skin and *in vivo* operations. Cyclic loading was conducted with a rate of 150 $\mu\text{m}/\text{s}$ (1.25 %/s) and 1 second delay at the reversal points and 9 cycles were driven between the GMR measurements at both reversal points.

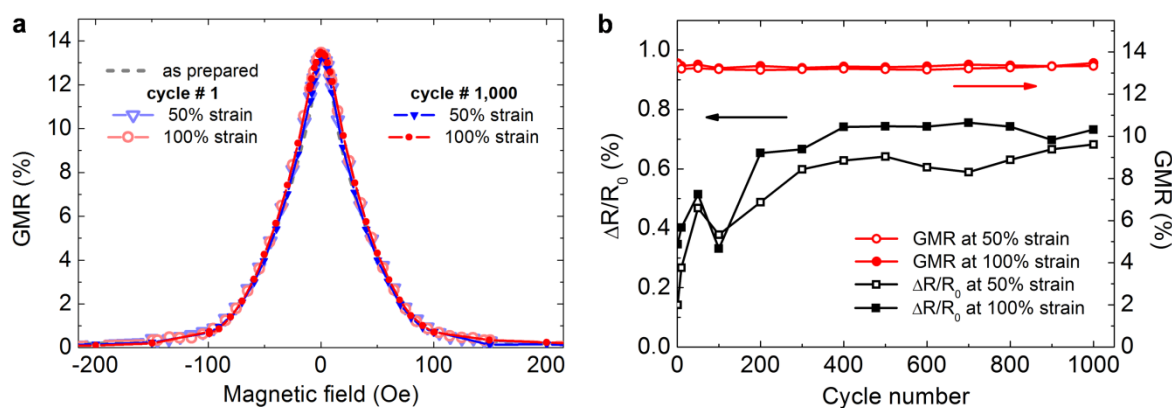


Figure 4.29 | Reliability upon cyclic loading: (a) GMR curves of a $[\text{Py}/\text{Cu}]_{30}^{\text{nd}}$ element under cyclic loading between 50% strain (\blacktriangledown) and 100% strain (\bullet), measured after the first cycle (open symbols) and after, cycle No. 1,000 (closed symbols). The characteristic of the as-prepared sample (at 0% strain) is also plotted in dashed gray. (b) \bullet GMR magnitude and \blacksquare resistance change normalized to the as-prepared sample ($R_0 = 10.0 \Omega$) at 50% strain (open symbols) and 100% strain (closed symbols) as a function of cycle number. Figure compiled from [7].

The GMR characteristics for the 1st and 1,000th loading cycle are displayed in **figure 4.29a** for the low- and high-strain state. They show no evidence of fatigue or any other influence of repeated loading. The recorded traces are congruent with each other and to the control measurement of the as-prepared sensor in the fully relaxed state (0% strain). Figure 4.29b plots the GMR magnitude and relative resistance change (normalized to the as-prepared sensor before lamination) for the high (100%) and

low (50%) strain reversal points versus cycle number. The GMR values remain at their high level throughout the 1,000 loading cycles, and even the electrical resistance of the nanomembrane stays nearly unchanged (far less than 1% resistance change over 1,000 cycles). Although a slight resistance increase is observed over the first 200 cycles, saturation sets in and no further fatigue occurs. This is remarkable for a fully functional sensor element, as such a long-term stability is rarely observed even for simple stretchable conductors¹⁴¹.

These results prove in a compelling way that imperceptible GMR sensors are rugged and very durable, a prerequisite for “real world” electronic skin and stretchable electronics applications. The here presented stretchable GMR sensors outperform all previously introduced elements in terms of stretchability, reliability and application potential by a multiple. Since both the GMR magnitude and the sensor’s resistance are invariant to stretching, no additional strain calibration is necessary and the sensor elements can be regarded as truly strain invariant. The outstanding resilience of the presented imperceptible and stretchable GMR elements against high and repeated mechanical deformations can be attributed to the ductile properties of the used metals in the Co/Cu and Py/Cu GMR stacks, in particular those of copper. It has recently been shown, that thin copper films are much less susceptible to aging upon repeated deformations in the concept of imperceptible electronics compared to *e.g.* Al or Ag electrodes⁴⁵.

4.4.5 Biaxial stretchability

The ultimate goal for stretchable electronic systems is to be compliant also against high biaxial deformations. Sensor elements ideally show orthogonality of arbitrary imposed deformations to the detected signal. For the case of GMR sensors, this means that both, the magnetoelectric characteristic and the resistance, are not altered by any deformation, including areal expansion of the device. Using biaxial pre-strain, the here presented GMR sensing elements can also be stretched in all lateral directions simultaneously. This feature is demonstrated in **figure 4.30** by the operation of an imperceptible sensor on an expanding diaphragm. The diaphragm was prepared as described in section 3.1.6. An imperceptible $[\text{Co}/\text{Cu}]_{30}^{2\text{nd}}$ sensor element is attached face down to the top of the VHB membrane while it is strongly inflated by water, which generates the strong biaxial pre-strain. The GMR sensor is contacted on the two outmost contact pads with 50 μm copper wires and silver paste before lamination. Upon deflating the diaphragm, the attached sensor is biaxially compressed and wrinkles accordingly. A photograph of the biaxially stretched GMR sensor on the inflated diaphragm being placed between the pole shoes of the magnetoelectric characterization setup is provided in figure 4.30a.

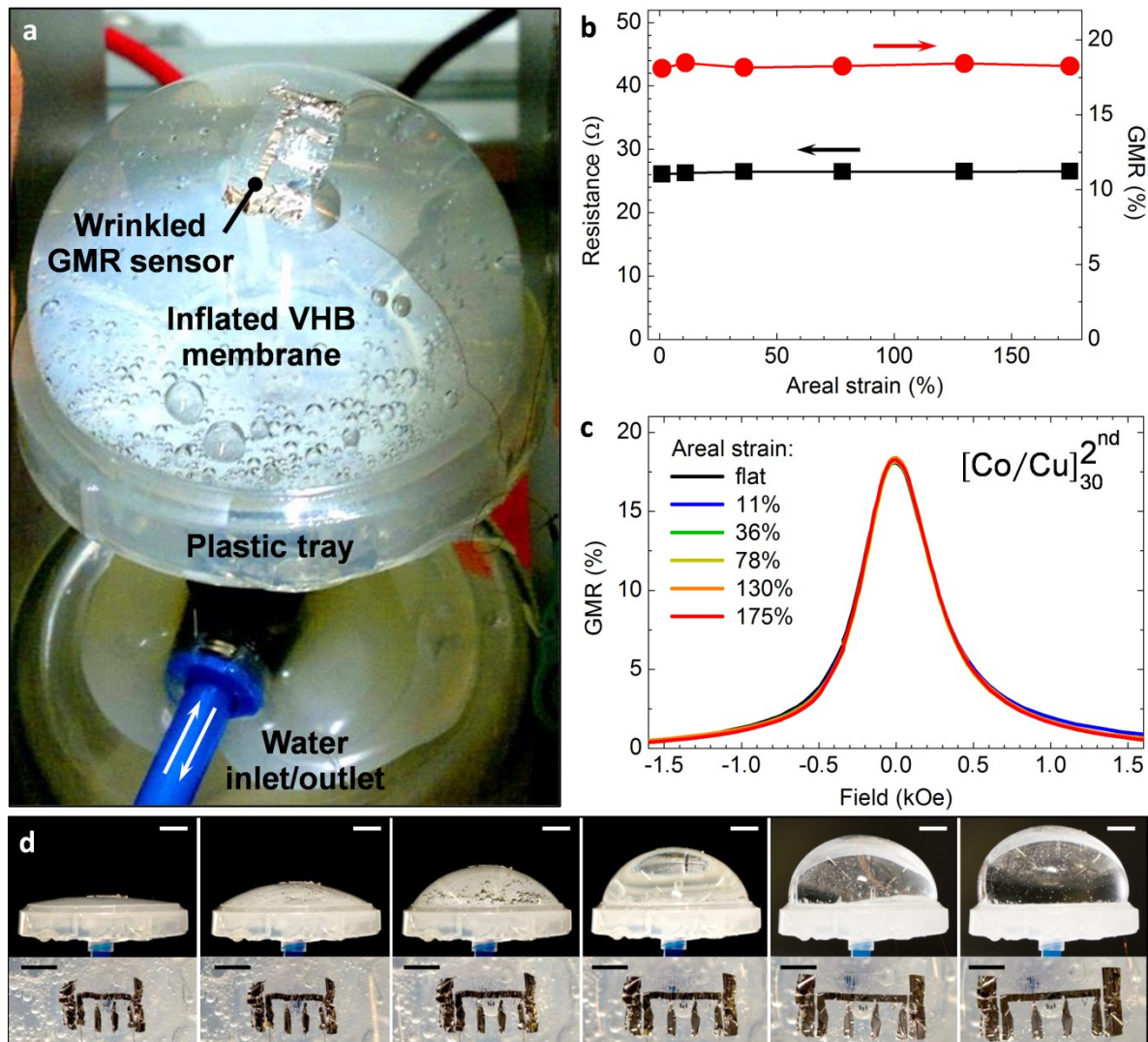


Figure 4.30 | Biaxial stretchability on an expanding diaphragm: (a) Biaxially stretchable $[\text{Co}/\text{Cu}]_{30}^{2\text{nd}}$ GMR sensor on a VHB diaphragm inflated by water. (b) GMR magnitude (●) and sensor resistance (■) as a function of applied areal strain. (c) GMR curves recorded for different inflation states. The corresponding areal strain was estimated from the side view photographs of each inflated state shown in the upper row of (d), in collaboration with Martin Melzer (University of Potsdam). The bottom row shows the biaxially wrinkled sensor for the inflation above, respectively. Scale bars: 10 mm (top), 5 mm (bottom). Photography in (d) was performed in collaboration with Dmitriy Karnaushenko (IFW Dresden). Figure compiled from [7].

Figure 4.30b shows the GMR characterization results of the $[\text{Co}/\text{Cu}]_{30}^{2\text{nd}}$ sensor on the diaphragm at different inflation states, from planar to 175% areal strain. As for the uniaxial case, the GMR magnitude as well as the absolute sensor resistance remain at a constant level with stretching. In this experiment, the stretchable GMR element was characterized with a two-point resistance measurement, which demonstrates the contact resistance being also stable with applied strain. Furthermore, for biaxial stretching, the GMR curves at different strains are congruent with each other as well (figure 4.30c). A set of images showing the inflation of the diaphragm (top) and the respective wrinkling of the sensor (bottom) for all strain levels characterized in this experiment is given in figure 4.30d. The side-view photographs at the top were in fact used to estimate the amount of areal strain at the sensor position as described in section 3.1.6.

With the demonstration of biaxial stretchability, the developed platform for magnetic sensorics reveals excellent capabilities in terms of strain invariance. The here presented GMR elements are compliant to literally any kind of deformation that can occur on an arbitrary surface. These versatile features are imparted to the magnetoelectronic devices by their ultra-thin and –flexible, yet robust polymeric support. Hence, the field of potential applications can be even extended, compared to uniaxially stretchable sensor devices, as presented by a final demonstrator in the following section.

4.4.6 Demonstrator: Dynamic detection of diaphragm inflation

The geometry of an expanding diaphragm was chosen as it represents several potential applications for biaxially compliant magnetic sensors, *e.g.* soft diaphragm actuators made of electro-active polymers^{76,215} or multifunctional medical implants on muscular biological tissue⁶⁷. Using the stretchable sensor on the diaphragm, one can for example easily detect its inflation by adding a permanent magnet at a central position into the water chamber, as shown in **figure 4.31a**. In this configuration, the sensor resistance gives a measure for the distance to the permanent magnet, and hence the inflation of the diaphragm (figure 4.31b). For this task, a $[\text{Co}/\text{Cu}]_{30}^{\text{nd}}$ element was chosen, as it gives the largest GMR signal in the typical field range (<500 Oe) of a permanent magnet in few millimeters to few centimeters distance, among the here studied multilayer systems (figure 4.6). The obtained sensor signal for a permanently pulsating diaphragm is displayed in figure 4.31c, which readily monitors its inflation and deflation in real time.

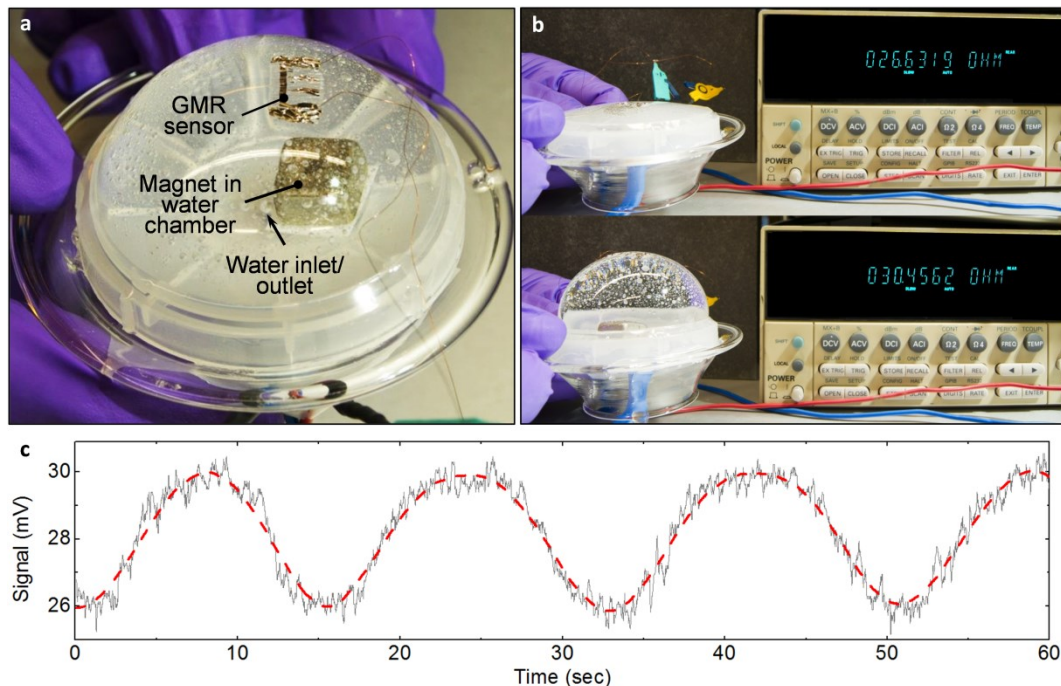


Figure 4.31 | Demonstrator of a magnetic detector for soft diaphragm actuation (a) Inflated diaphragm with compliant $[\text{Co}/\text{Cu}]_{30}^{\text{nd}}$ GMR sensor and a permanent magnet fixed in the water chamber on the plastic tray. (b) The resistance of the sensor is displayed on a directly connected multimeter for the deflated (top) and inflated (bottom) diaphragm. (c) Recorded sensor signal for a pulsating diaphragm demonstrating the dynamic magnetic detection of its inflation. The dashed line is a smoothed graph to guide the eye. Experiment conducted in collaboration with Dmitriy & Daniil Karnaushenko and Dr. Denys Makarov (all IFW Dresden). Figure compiled from [7].

5. CONCLUSIONS & OUTLOOK

5.1 Achievements

The here presented work reflects the successful establishment of stretchable GMR based magnetic sensorics, describing the entire development from the first attempts to verify the functional concept⁶ to the realization of ready-to-use highly compliant and strain invariant sensor devices with remarkable robustness⁷. The developed technology platform offers considerable application potentials in the field of smart skins and textiles, soft robotics, medical implants and consumer electronics. The GMR effect, which occurs in carefully prepared thin metallic films comprising magnetic materials, was chosen as the basic magnetic sensing principle. Magnetoresistive layer stacks were deposited or transferred onto elastomeric films, which serve as compliant supports and determine the unique mechanical properties of the sensor elements. Photolithographic structuring was performed to define test layouts that allow for accurate magnetoelectrical characterization. This, however, renders the sensor design and hence some of its spatial, electric and magnetic properties to be adapted for specific applications or system requirements. Stretchability of the GMR sensors is achieved by specific morphologic features brought into the magnetosensitive thin films, which accommodate the applied tensile deformation while maintaining the electrical and magnetic integrity of the device.

The morphologic feature that is mostly applied in this work to obtain stretchable GMR elements is wrinkling¹⁴⁷, which occurs if a soft material with a harder skin is compressed laterally. The usage of a thermally induced pre-strain in the elastomeric support and subsequent wrinkling of a GMR multilayer that was deposited on top led to the realization of the world's first elastically stretchable magnetic sensor element⁶. The magnetoelectric performance of this first demonstrator was identical to GMR multilayer sensors fabricated on conventional rigid substrates and did not degrade if stretched by several percent. Based on that, different optimizations and advancements were conducted in order to enhance the sensor properties. The sensitivity to low magnetic fields, as required for most e-skin and biomedical applications, was increased by lowering the magnetic coupling strength between the ferromagnetic layers, by using magnetically softer materials the GMR stack¹⁶⁶ or by replacing the GMR multilayers by more advanced spin valve stacks¹⁶⁷. The application of spin valves also gave rise to an improved stretchability by incorporating predetermined periodic fracturing sites in combination with deposition-induced random wrinkles¹⁶⁷.

Increasing the resilience against tensile deformation without relying on crack formation was achieved by using mechanically instead of thermally induced pre-strain. For this purpose, a novel fabrication process was developed that allows transferring the GMR sensor devices from a rigid donor substrate to a pre-strained rubber membrane, which results in stretchabilities of about 30% in GMR multilayers¹⁶³. The introduced direct transfer process also greatly enhances the miniaturization and level of complexity of the compliant GMR devices, as their initial preparation can be done on conventional

rigid substrates. Therefore, entire microsensor arrays including electrode structures could be transferred to elastomeric receiver substrates in a single step¹⁶³.

The final breakthrough in stretchable magnetoelectronics came with the preparation of GMR multilayer elements onto ultra-thin (1.4 μm) plastic membranes, which leads to magnetic sensors that are extremely light weight ($\approx 3 \text{ g/m}^2$), conform to arbitrary surface geometries and seamlessly follow deformations or distortions without performance degradation⁷. As these imperceptible magnetoelectronic devices can be worn directly on the skin, they can add a “sixth sense” of magnetoception⁸⁴ to electronic skin systems. Laminating the ultra-thin GMR foil onto highly pre-stretched rubber tape, results in large stretchabilities of up to 270% without altering any of their magnetoelectric characteristics; hence they are truly strain invariant. These magnetic sensors can even be stretched biaxially and showed a remarkable durability by enduring 1,000 loading cycles without any fatigue.

With the optimizations described above, the key attributes of stretchable GMR sensors (*i.e.* sensitivity, stretchability, miniaturization and durability) were improved by about two orders of magnitude^{7,163,167} compared to the original design⁶. The comprehensive magnetoelectrical characterization of the sensing performance upon tensile deformation was realized in a magnetoresistive measuring setup, which was equipped with a custom designed computer controlled module for *in situ* stretching. The presentation of the sensor performance at different development stages is supplemented with in-depth microscopic investigations of the sensor morphology and its transitions upon stretching as well as analyses of their possible influence on the sensing behavior. Various demonstrations of prospective application examples on a proof-of-concept level were included as well. Furthermore, several novel aspects, like self-healing¹⁴⁵, isotropic sensitivity¹⁶⁶ or on-skin magnetoception⁷, which are evoked in magnetic sensorics by the unique mechanical properties, are highlighted. Since the developed platform was demonstrated with different kinds of magnetoresistive systems, including various multilayers¹⁶⁶ and spin valves¹⁶⁷, it represents a universal basis for the realization of stretchable GMR based sensorics and may even be extended to advanced spintronic systems⁸² (*e.g.* magnetoresistive memories²¹⁶ or magnetic logic devices²¹⁷).

The experience gained during the development of stretchable magnetoresistive sensorics could successfully be applied to support different other works, *e.g.* the development of a technological platform for flexible microfluidics with integrated magnetic analytics⁸⁶, that were generated within the research team over the time. Another highly important project in this respect includes the realization of flexible hall sensorics¹⁸⁴, which has very promising potential for an application in electrical machines and drives. This work is briefly introduced in subchapter 5.3. Beyond that, recently also other groups studied magnetic structures embedded in or on soft materials^{109,218,219}, which gave rise to both, interesting fundamental phenomena as well as promising application potentials.

5.2 Outlook

5.2.1 Further development steps

The sensor layout utilized in the present work was designed as a test structure for the establishment of stretchable GMR sensorics that allows for precise magnetoelectric characterization. Since photolithographic patterning of the magnetoresistive nanomembranes was successfully applied from the very beginning, the device structure can be adapted and scaled to meet the requirements for specific applications and design concepts. Patterning defined meander structures, for instance, will adapt the electrical parameters of individual sensing elements to the requirements of a specific signal processing electronics. Preparing the GMR elements into a Wheatstone bridge configuration would allow for a differential signal and may compensate for temperature effects. An integration of compliant ferromagnetic structures²¹⁹ can help to realize a magnetic biasing of the proposed GMR sensors to operate them around a defined working point of the GMR response curve in a fully stretchable design. This would not only allow using the maximum sensitivity of the respective elements but may also add a sense of directionality to lift the symmetry of magnetic field sign in GMR multilayers. Finally, detailed finite element method (FEM) mechanical modeling will be necessary to further guide sensor improvements.

For a successful commercialization of stretchable magnetic sensors, the long-term stability upon deformation far beyond the 1,000 loading cycles shown in this work has to be verified. To further reduce the impact of mechanical stresses on the functional magnetic nanomembrane upon device deformation, the GMR film may be situated in a neutral mechanical plane¹³⁴. For the imperceptible magnetic sensors, this can be realized by chemical vapor depositions of parylene, which results in a thin and inert passivation layer⁵⁵. It homogeneously covers also highly non-planar surfaces with a controllable thickness and is even biocompatible. This would also render these sensors suitable for more practical on-skin and *in vivo* use, by preventing long-term damage from aggressive body fluids. However, further reliability tests against the persistent exposure to temperature changes, humidity and vibrations have to be undertaken to qualify soft magnetic sensors for “real world” applications. Apart from that, the general fabrication processes applied here principally allow for large area and high throughput production of the introduced compliant GMR sensors.

Future work will also focus on optimizations to interface electrically and mechanically with other soft electronic components enabling for example signal conditioning⁵⁵, multiplexing¹⁶ or wireless readout and remote sensing⁵³ to overcome the mayor issue of reliable electrical contacting. The integration of stretchable magnetoelectronics with various functional elements on comparable platforms like solar cells⁴⁸, light emitting diodes³⁸, rechargeable batteries⁵¹ as well as temperature⁴⁵ and tactile¹⁶ sensors, will enable autonomous and versatile soft smart systems with a multitude of sensing and responsive features.

5.2.2 Prospective applications.

Several potential application areas of stretchable magnetic sensorics, *i.e.* smart skins and textiles, soft robotics and medical implants, were already mentioned in the motivation of this work (subchapter 1.1). Some more specific implementation scenarios were also demonstrated throughout the results chapter. The dynamic detection of a soft diaphragm's actuation (section 4.4.6), for example, demonstrates the high potential of stretchable magneto-electronics for the emerging field of soft robotics^{69,71} and elastomeric actuators^{39,72}. Position and motion tracking in conventional machines and facilities (*e.g.* in automotive and production) is after all the main application area of magnetic sensorics, nowadays. Besides being cost efficient, this is mainly because on the emitting side (*i.e.* by means of permanent magnets) no power supply is needed, which also greatly enhanced the design freedom. The current establishment of soft robotic machines^{68,74,75,77} calls for similar sensoric counterparts that share their novel mechanical properties. The stretchable GMR sensors developed here meet all the requirements, in particular high sensitivity, strain invariance and mechanical robustness, for the integration into soft robotic systems. However, in order to keep the entire system soft, unlike in the presented demonstrator, the magnetic emitter should be compliant as well. Recently, P. Tseng *et al.* introduced stretchable designs of micromagnet arrays²¹⁹. The intelligent incorporation of compliant magnetic structures and stretchable GMR sensors into soft actuators, *e.g.* according to **figure 5.1a**, would allow for a highly integrated solution for detecting its deformations in real-time.

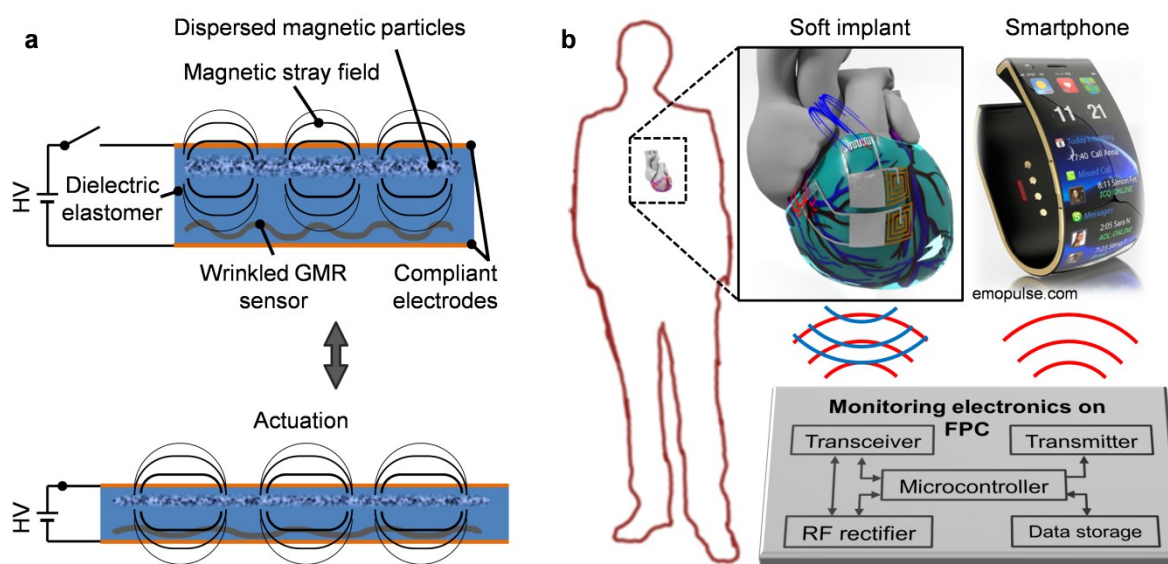


Figure 5.1 | Examples of prospective applications: Conceptual view of two application examples for stretchable magneto-electronics. **(a)** Integrated actuation gauge in a dielectric elastomer actuator (DEA). The DEA consists of a rubber dielectric film sandwiched between two compliant electrodes. Upon application of a high voltage, the electrostatic attraction of the electrodes squeezes the DEA, causing it to actuate laterally. The integrated stretchable GMR sensor detects a signal from the dispersed magnetic particles beneath the opposite electrode, due to their reduced distance upon actuation. **(b)** Smart medical implant for heart valve monitoring. Stretchable GMR sensors attached to the surface of the heart detect the motion of small permanent magnets implanted on the cardiac valves. Equipped with a wireless transmission module, it could automatically send an emergency call via the patient's mobile communication device, in the case of detected irregularities. Figure (b) was compiled by Denys Makarov and Dmitriy Karnaushenko.

Furthermore, the demonstration of on-skin magnetoception⁷ already enables magnetic proximity detection (section 4.4.3) and, with improvements mentioned above, will also allow for navigation and touchless control features in electronic skins. This work is foreseen to inspire a diverse number of e-skin devices that will benefit from a “sixth sense” magnetoception. Unlike optical sensors, no line-of-sight between the sensor and the magnetic field emitter is required. This allows transmitting “magnetic messages” through all non-magnetic objects like safety enclosures, displays or even walls. This can have profound application potentials for high security environments. The encoding can be realized both statically via permanent magnets as well as dynamically with current driven wirings. Passivated into biocompatible enclosures, like parylene, the imperceptible sensor elements will also add the magnetic functionalities to medical implants⁴⁷ and advanced surgical tools⁶⁷. The magnetic signal would need to come from artificial sources, like magnetic particles or small permanent magnets, being fixed onto the moving parts under surveillance. This would allow monitoring specific physiological actions and processes (e.g. joints or muscular and cardiac valve activity) and, for example alert at imminent seizures (figure 5.1b).

Finally, the successful realization of compliant arrays of microsized GMR sensors using the direct transfer approach renders high resolution magnetic mapping on arbitrary non-planar surfaces possible. Similar investigations are by now only feasible on planar geometries, using optical or scanning probe techniques, or my means of synchrotron radiation. A GMR microsensor array, however, could perform real-time monitoring in a very compact configuration that allows the application also in an industrial environment. A multiplexing technique should necessarily be integrated into such a microsensory system, though, to account for an efficient data acquisition from numerous sensing elements.

5.3 Technological impact: Flexible Bi Hall sensorics

Despite the appealing properties of the here developed stretchable GMR based sensorics platform and their far-reaching application potential, there are application areas, where stretchability is not necessarily required. One prominent example is the magnetic field characterization and monitoring in conventional electrical machines and drives. This section briefly reviews activities on the development of flat and flexible bismuth based Hall sensorics²²⁰ that was carried out due to specific requests from this particular industrial sector.

5.3.1 Application potential

Figure 5.2a shows a simplified cross section of a rotary electrical machine, with a rotor part positioned between the stator poles. Electrical windings around the stator poles generate high magnetic fields inside the air gap between rotor and stator to drive the machine. For high-performance electrical machines, the air gap needs to be as narrow as possible (typically $\leq 500 \mu\text{m}$). As the *magnetic flux density* is the relevant system variable for magnetic force generation, the direct measurement of magnetic fields is of special interest for further optimizations and improved control of such

electromotive devices. Magnetic monitoring has profound advantages for *active magnetic bearing* (AMB) systems, in particular, as it enables *flux based control* of the magnetic levitation²²¹. AMBs achieve increasing acceptance in many applications like turbo pumps and turbines, flywheels, beam choppers, active vibration damping, satellite stabilization or as implanted ventricular assist devices. Flux based control strategies offer enhanced stiffness, damping and redundancy for AMBs, allow for more precise control of the rotor position during its operation and may help to reduce production costs^{185,221}.

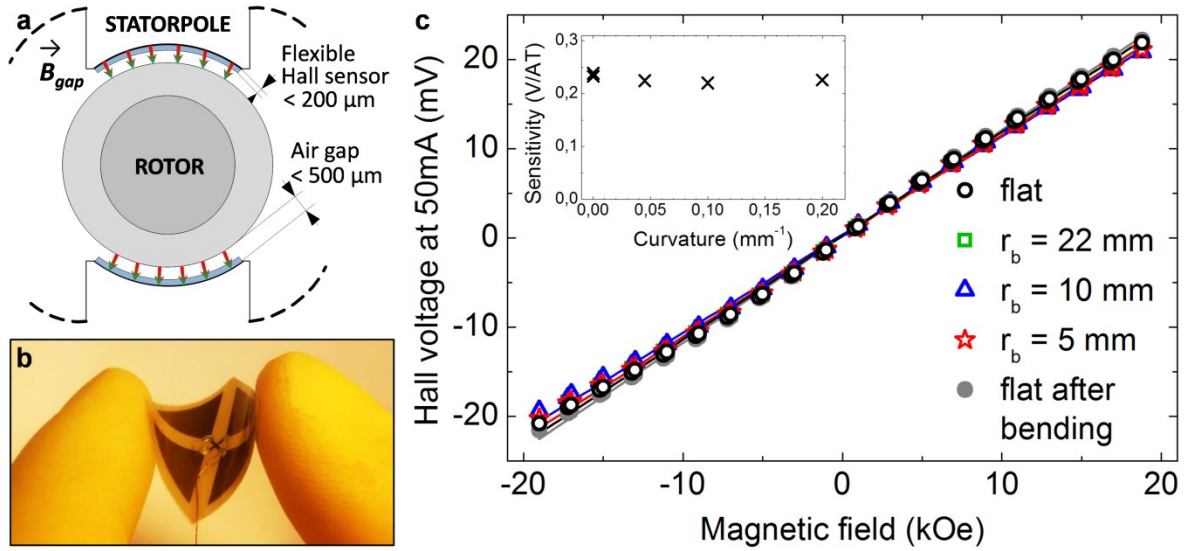


Figure 5.2 | Flexible bismuth based Hall sensors for electrical machines and drives: (a) Conceptual cross-section of a rotary electrical machine with a magnetic field in the air gap between rotor and stator. (b) Fabricated bismuth Hall probe bent between the fingers. (c) Sensor response at 50 mA supply current for different bending radii. The inset shows the Hall sensitivity in dependence of the sensor curvature. Sketch in (a) was drawn by Falk Bahr (TU Dresden) Figure compiled from [186,220].

5.3.2 Thin and flexible Hall probes

Since the magnetic field generated inside the air gap is oriented perpendicular to the stator pole surface and can reach up to about 22 kOe in magnitude, Hall effect sensors are the primary choice for its recognition. In order to meet the safety margins inside the air gap, an integrated magnetic sensor device should preferably be below 200 μm in height and feature a certain flexibility to obtain conformal contact to the curved stator pole, as indicated in figure 5.2a; features that are not available in commercial semiconductor based Hall sensors²²².

2 μm bismuth films sputtered onto flexible polyether ether ketone (PEEK) substrates and lithographically patterned into a cross shape, in collaboration with Ingolf Mönch (IFW Dresden), were applied to realize bendable Hall probes with a total height of only 80 μm , including encapsulation with adhesive tape²²⁰ (figure 5.2b). After contacting with twisted pairs of copper wires, the total sensor height was 280 μm . Hall characterizations clearly revealed a stable sensor response to out-of-plane fields for bending radii down to 5 mm, as shown in figure 5.2c, which qualifies the prepared bismuth

probes for the usage also in small magnetic bearings and on curved surfaces of other electrical machines.

The prepared sensors were successfully used to demonstrate their capability for flux based control of magnetically suspended systems in a collaborative work with Balk Fahr and Wilfried Hofmann at the TU Dresden¹⁸⁶. In a levitating ball test setup, the flux based control using the feedback from the flexible Bi Hall sensors revealed less overshooting, reduced displacement and smaller response times compared to conventional control strategies²²⁰.

5.3.3 Continuative works and improvements

To allow for mass production at low cost, bismuth films were deposited directly onto commercially available flexible printed circuits (FPCs)¹⁸⁴, designed by Daniil Karnaushenko (IFW Dresden). This fabrication approach helps to reduce the total sensor thickness to 150 μm , including contacts. The Hall sensitivity of the sputtered Bi layer was optimized by Yevhen Zabala (IFW Dresden / IFJ Krakow) through adapting the film thickness and sputter conditions and by applying post annealing, to reach the bulk value of bismuth. More complex sensor arrangements, such linear or 2D sensor arrays, were readily obtained, by adapting the FPC design¹⁸⁴, by G. Santiago Cañion B. (IFW Dresden). These layouts can be used for position monitoring and on-line magnetic mapping in spatially confined environments or non-planar geometries. Suitable packaging strategies for flexible Bi probes were developed as well as reliability tests conducted by Daniel Ernst (TU Dresden)²²³.

The thus obtained flexible Hall sensor prototypes are to be tested under real conditions in the narrow air gaps of a multiaxis AMB test setup, by Falk Bahr (TU Dresden), to demonstrate flux based control and its advantages under more realistic conditions. In addition, the application potential for wearable magnetic sensorics was demonstrated¹⁸⁴. Bismuth Hall probes were already provided to external partners, including research institutes and companies, for in-field testing.

5.4 Activities on technology transfer and public relations

The present thesis represents a highly interdisciplinary project on the junction of physics, engineering and materials science. The outcome of this work was frequently presented on the domestic and international level at most renowned scientific conferences for the magnetism and materials science communities (*e.g.* INTERMAG, MMM conference, MRS meeting, DPG meeting) as well as on more focused seminars (*e.g.* Heraeus seminar, Lüscher seminar). However, due to the highly applied nature of the conducted work, various activities for the *technology transfer* were undertaken along with the described scientific development of stretchable magnetoelectronics to initiate and support an effective innovation process. The obtained achievements were put into the broader concept of *shapeable magnetic sensorics*, which also includes approaches for flat and flexible¹⁸⁴ as well as printable^{182,183,224} designs of magnetic sensor devices. This concept was frequently presented to leading industry representatives at innovation fairs and exhibitions (*e.g.* Hannover Messe, Innovation Days,

Sensor + Test) or during organized lab tours. The intellectual property rights were reserved by patent applications²²⁵.

In order to make the achieved developments accessible to public community, the prepared demonstrators, that were described throughout this work, were presented to a broad public *e.g.* during the long night of sciences and to interested students at guided lab sightseeings on a regular base. Various aspects of this work, in particular the latest developments of imperceptible magnetic sensorics⁷, were highlighted in the newspapers and the news section of many web sites with a scientific background, both nationally and internationally. Furthermore, a telephone interview about on-skin magnetoception was broadcasted live during a well-known radio show.

With the gained expertise, I could strongly contribute to related projects, which helped to acquire further third party funding, mainly from public sources, *e.g.* European Research Council (ERC), German Federal Ministry of Education and Research (BMBF) and German Research Foundation (DFG).

References

- 1 Rogers, J. A., Someya, T., and Huang, Y. G., Materials and Mechanics for Stretchable Electronics. *Science* **327** (5973), 1603 (2010).
- 2 Wagner, S. and Bauer, S., Materials for stretchable electronics. *MRS Bull.* **37** (3), 207 (2012).
- 3 Bauer, S. et al., 25th Anniversary Article: A Soft Future: From Robots and Sensor Skin to Energy Harvesters. *Adv. Mater.* **26** (1), 149 (2014).
- 4 Chen, Y. F. et al., Towards flexible magnetoelectronics: Buffer-enhanced and mechanically tunable GMR of Co/Cu multilayers on plastic substrates. *Adv. Mater.* **20** (17), 3224 (2008).
- 5 Barraud, C. et al., Magnetoresistance in magnetic tunnel junctions grown on flexible organic substrates. *Appl. Phys. Lett.* **96** (7), 3 (2010).
- 6 Melzer, M. et al., Stretchable Magnetoelectronics. *Nano Lett.* **11** (6), 2522 (2011).
- 7 Melzer, M. et al., Imperceptible magnetoelectronics. *Nat. Commun.* **6**, 6080 (2015).
- 8 Forrest, S. R., The path to ubiquitous and low-cost organic electronic appliances on plastic. *Nature* **428** (6986), 911 (2004); Sun, Y. G. and Rogers, J. A., Inorganic semiconductors for flexible electronics. *Adv. Mater.* **19** (15), 1897 (2007); Shahrjerdi, D. and Bedell, S. W., Extremely Flexible Nanoscale Ultrathin Body Silicon Integrated Circuits on Plastic. *Nano Lett.* **13** (1), 315 (2013).
- 9 Kim, D. H. et al., Stretchable and foldable silicon integrated circuits. *Science* **320** (5875), 507 (2008).
- 10 Sekitani, T. et al., A rubberlike stretchable active matrix using elastic conductors. *Science* **321** (5895), 1468 (2008).
- 11 Someya, T., *Stretchable Electronics*. (Wiley-VCH, Weinheim, 2013).
- 12 Sekitani, T. and Someya, T., Stretchable, Large-area Organic Electronics. *Adv. Mater.* **22** (20), 2228 (2010).
- 13 Lipomi, D. J., Tee, B. C. K., Vosgueritchian, M., and Bao, Z. N., Stretchable Organic Solar Cells. *Adv. Mater.* **23** (15), 1771 (2011).
- 14 Kim, J.-H., Han, M. J., and Seo, S., Flexible, stretchable, and patchable organic devices integrated on freestanding polymeric substrates. *Journal of Polymer Science Part B: Polymer Physics* (2015).
- 15 Someya, T. et al., Conformable, flexible, large-area networks of pressure and thermal sensors with organic transistor active matrixes. *Proc. Natl. Acad. Sci. U. S. A.* **102** (35), 12321 (2005).
- 16 Kaltenbrunner, M. et al., An ultra-lightweight design for imperceptible plastic electronics. *Nature* **499** (7459), 458 (2013).
- 17 Kim, D. H. et al., Stretchable, Curvilinear Electronics Based on Inorganic Materials. *Adv. Mater.* **22** (19), 2108 (2010).
- 18 Kim, R. H. et al., Waterproof AllInGaP optoelectronics on stretchable substrates with applications in biomedicine and robotics. *Nat. Mater.* **9** (11), 929 (2010).
- 19 Cheng, S. and Wu, Z. G., Microfluidic stretchable RF electronics. *Lab Chip* **10** (23), 3227 (2010).
- 20 Gonzalez, M. et al., Design and implementation of flexible and stretchable systems. *Microelectron. Reliab.* **51** (6), 1069 (2011).
- 21 Park, M. et al., Highly stretchable electric circuits from a composite material of silver nanoparticles and elastomeric fibres. *Nat. Nanotechnol.* **7** (12), 803 (2012).
- 22 Vandeparre, H., Watson, D., and Lacour, S. P., Extremely robust and conformable capacitive pressure sensors based on flexible polyurethane foams and stretchable metallization. *Appl. Phys. Lett.* **103** (20), 4 (2013).
- 23 Cavallo, F. and Lagally, M. G., Semiconductors turn soft: inorganic nanomembranes. *Soft Matter* **6** (3), 439 (2010).
- 24 Bowden, N. et al., Spontaneous formation of ordered structures in thin films of metals supported on an elastomeric polymer. *Nature* **393** (6681), 146 (1998).
- 25 Lacour, S. P., Wagner, S., Huang, Z. Y., and Suo, Z., Stretchable gold conductors on elastomeric substrates. *Appl. Phys. Lett.* **82** (15), 2404 (2003).
- 26 Wagner, S. et al., Electronic skin: architecture and components. *Physica E* **25** (2-3), 326 (2004).
- 27 Jones, J., Lacour, S. P., Wagner, S., and Suo, Z. G., Stretchable wavy metal interconnects. *J. Vac. Sci. Technol. A* **22** (4), 1723 (2004).

- 28 Lacour, S. P. et al., Stretchable interconnects for elastic electronic surfaces. *Proc. IEEE* **93** (8),
1459 (2005).
- 29 Gray, D. S., Tien, J., and Chen, C. S., High-conductivity elastomeric electronics. *Adv. Mater.*
16 (5), 393 (2004).
- 30 Gonzalez, M. et al., Design of metal interconnects for stretchable electronic circuits.
Microelectron. Reliab. **48** (6), 825 (2008).
- 31 Araki, T. et al., Printable and Stretchable Conductive Wirings Comprising Silver Flakes and
Elastomers. *IEEE Electron Device Lett.* **32** (10), 1424 (2011); Wang, X. L. et al., Stretchable
Conductors with Ultrahigh Tensile Strain and Stable Metallic Conductance Enabled by
Prestrained Polyelectrolyte Nanoplayers. *Adv. Mater.* **23** (27), 3090 (2011); Jeong, G. S. et
al., Solderable and electroplatable flexible electronic circuit on a porous stretchable elastomer.
Nat. Commun. **3** (2012); Park, J. et al., Three-dimensional nanonetworks for giant
stretchability in dielectrics and conductors. *Nat. Commun.* **3** (2012).
- 32 Fan, J. A. et al., Fractal design concepts for stretchable electronics. *Nat. Commun.* **5**, 8 (2014).
- 33 Kim, D. H. et al., Ultrathin Silicon Circuits With Strain-isolation Layers and Mesh Layouts
for High-Performance Electronics on Fabric, Vinyl, Leather, and Paper. *Adv. Mater.* **21** (36),
3703 (2009).
- 34 Lagally, M. G., Silicon nanomembranes. *MRS Bull.* **32** (1), 57 (2007).
- 35 Khang, D. Y., Jiang, H. Q., Huang, Y., and Rogers, J. A., A stretchable form of single-crystal
silicon for high-performance electronics on rubber substrates. *Science* **311** (5758), 208 (2006).
- 36 Choi, W. M. et al., Biaxially stretchable "Wavy" silicon nanomembranes. *Nano Lett.* **7** (6),
1655 (2007).
- 37 Yu, Z. B., Niu, X. F., Liu, Z. T., and Pei, Q. B., Intrinsically Stretchable Polymer Light-
Emitting Devices Using Carbon Nanotube-Polymer Composite Electrodes. *Adv. Mater.* **23**
(34), 3989 (2011).
- 38 White, M. S. et al., Ultrathin, highly flexible and stretchable PLEDs. *Nat. Photonics* **7** (10),
811 (2013).
- 39 Pelrine, R., Kornbluh, R., Pei, Q. B., and Joseph, J., High-speed electrically actuated
elastomers with strain greater than 100%. *Science* **287** (5454), 836 (2000).
- 40 Li, X., Gu, T. L., and Wei, B. Q., Dynamic and Galvanic Stability of Stretchable
Supercapacitors. *Nano Lett.* **12** (12), 6366 (2012).
- 41 Lipomi, D. J. et al., Skin-like pressure and strain sensors based on transparent elastic films of
carbon nanotubes. *Nat. Nanotechnol.* **6** (12), 788 (2011).
- 42 Yamada, T. et al., A stretchable carbon nanotube strain sensor for human-motion detection.
Nat. Nanotechnol. **6** (5), 296 (2011); Ramuz, M., Tee, B. C. K., Tok, J. B. H., and Bao, Z. N.,
Transparent, Optical, Pressure-Sensitive Artificial Skin for Large-Area Stretchable
Electronics. *Adv. Mater.* **24** (24), 3223 (2012).
- 43 Ko, H. C. et al., A hemispherical electronic eye camera based on compressible silicon
optoelectronics. *Nature* **454** (7205), 748 (2008).
- 44 Webb, R. C. et al., Ultrathin conformal devices for precise and continuous thermal
characterization of human skin. *Nat. Mater.* **12** (10), 938 (2013).
- 45 Drack, M. et al., An Imperceptible Plastic Electronic Wrap. *Adv. Mater.* **27** (1), 34 (2015).
- 46 Graudejus, O. et al., Characterization of an Elastically Stretchable Microelectrode Array and
Its Application to Neural Field Potential Recordings. *J. Electrochem. Soc.* **156** (6), P85
(2009).
- 47 Kim, D. H. et al., Materials for multifunctional balloon catheters with capabilities in cardiac
electrophysiological mapping and ablation therapy. *Nat. Mater.* **10** (4), 316 (2011).
- 48 Kaltenbrunner, M. et al., Ultrathin and lightweight organic solar cells with high flexibility.
Nat. Commun. **3** (2012).
- 49 McKay, T. G., O'Brien, B. M., Calius, E. P., and Anderson, I. A., Soft generators using
dielectric elastomers. *Appl. Phys. Lett.* **98** (14), 3 (2011); Qi, Y. et al., Enhanced
Piezoelectricity and Stretchability in Energy Harvesting Devices Fabricated from Buckled
PZT Ribbons. *Nano Lett.* **11** (3), 1331 (2011).
- 50 Lee, M. et al., A Hybrid Piezoelectric Structure for Wearable Nanogenerators. *Adv. Mater.* **24**
(13), 1759 (2012).
- 51 Kettlgruber, G. et al., Intrinsically stretchable and rechargeable batteries for self-powered
stretchable electronics. *J. Mater. Chem. A* **1** (18), 5505 (2013).
- 52 Xu, S. et al., Stretchable batteries with self-similar serpentine interconnects and integrated
wireless recharging systems. *Nat. Commun.* **4** (2013).

- 53 Kim, D. H. et al., Epidermal Electronics. *Science* **333** (6044), 838 (2011).
- 54 Hwang, S. W. et al., A Physically Transient Form of Silicon Electronics. *Science* **337** (6102),
1640 (2012); Bauer, S. and Kaltenbrunner, M., Built To Disappear. *ACS Nano* **8** (6), 5380
(2014).
- 55 Salvatore, G. A. et al., Wafer-scale design of lightweight and transparent electronics that
wraps around hairs. *Nat. Commun.* **5** (2014).
- 56 Lumelsky, V. J., Shur, M. S., and Wagner, S., Sensitive Skin. *IEEE Sens. J.* **1** (1), 41 (2001);
Hammock, M. L. et al., 25th Anniversary Article: The Evolution of Electronic Skin (E-Skin):
A Brief History, Design Considerations, and Recent Progress. *Adv. Mater.* **25** (42), 5997
(2013).
- 57 Jeong, J. W. et al., Materials and Optimized Designs for Human-Machine Interfaces Via
Epidermal Electronics. *Adv. Mater.* **25** (47), 6839 (2013).
- 58 Yeo, W. H. et al., Multifunctional Epidermal Electronics Printed Directly Onto the Skin. *Adv.*
Mater. **25** (20), 2773 (2013).
- 59 Graz, I. et al., Flexible active-matrix cells with selectively poled bifunctional polymer-ceramic
nanocomposite for pressure and temperature sensing skin. *J. Appl. Phys.* **106** (3) (2009).
- 60 Schwartz, G. et al., Flexible polymer transistors with high pressure sensitivity for application
in electronic skin and health monitoring. *Nat. Commun.* **4**, 8 (2013); Park, J. et al., Tactile-
Direction-Sensitive and Stretchable Electronic Skins Based on Human-Skin-Inspired
Interlocked Microstructures. *ACS Nano* **8** (12), 12020 (2014).
- 61 Gong, S. et al., A wearable and highly sensitive pressure sensor with ultrathin gold nanowires.
Nat. Commun. **5**, 8 (2014).
- 62 Huang, X., Yeo, W. H., Liu, Y. H., and Rogers, J. A., Epidermal Differential Impedance
Sensor for Conformal Skin Hydration Monitoring. *Biointerphases* **7** (1-4) (2012).
- 63 Son, D. et al., Multifunctional wearable devices for diagnosis and therapy of movement
disorders. *Nat. Nanotechnol.* **9** (5), 397 (2014).
- 64 Tee, B. C. K., Wang, C., Allen, R., and Bao, Z. N., An electrically and mechanically self-
healing composite with pressure- and flexion-sensitive properties for electronic skin
applications. *Nat. Nanotechnol.* **7** (12), 825 (2012).
- 65 Kim, D. H. et al., Dissolvable films of silk fibroin for ultrathin conformal bio-integrated
electronics. *Nat. Mater.* **9** (6), 511 (2010).
- 66 Viventi, J. et al., Flexible, foldable, actively multiplexed, high-density electrode array for
mapping brain activity in vivo. *Nat. Neurosci.* **14** (12), 1599 (2011); Ware, T. et al.,
Fabrication of Responsive, Softening Neural Interfaces. *Adv. Funct. Mater.* **22** (16), 3470
(2012); Park, G. et al., Immunologic and Tissue Biocompatibility of Flexible/Stretchable
Electronics and Optoelectronics. *Adv. Healthc. Mater.* **3** (4), 515 (2014).
- 67 Kim, D. H. et al., Electronic sensor and actuator webs for large-area complex geometry
cardiac mapping and therapy. *Proc. Natl. Acad. Sci. U. S. A.* **109** (49), 19910 (2012).
- 68 Martinez, R. V. et al., Robotic Tentacles with Three-Dimensional Mobility Based on Flexible
Elastomers. *Adv. Mater.* **25** (2), 205 (2013).
- 69 Shepherd, R. F. et al., Multigait soft robot. *Proc. Natl. Acad. Sci. U. S. A.* **108** (51), 20400
(2011).
- 70 Zysset, C. et al., Textile integrated sensors and actuators for near-infrared spectroscopy. *Opt.*
Express **21** (3), 3213 (2013); Smart Textiles: [http://smarttextiles.se/en/saturday-light-fever-
2/#prettyPhoto](http://smarttextiles.se/en/saturday-light-fever-2/#prettyPhoto), (2015).
- 71 Ilievski, F. et al., Soft Robotics for Chemists. *Angew. Chem.-Int. Edit.* **50** (8), 1890 (2011).
- 72 Schuhladen, S. et al., Iris-Like Tunable Aperture Employing Liquid-Crystal Elastomers. *Adv.*
Mater. **26** (42), 7247 (2014).
- 73 Kofod, G., Wirges, W., Pajananen, M., and Bauer, S., Energy minimization for self-organized
structure formation and actuation. *Appl. Phys. Lett.* **90** (8), 3 (2007).
- 74 Martinez, R. V. et al., Soft Actuators and Robots that Are Resistant to Mechanical Damage.
Adv. Funct. Mater. **24** (20), 3003 (2014).
- 75 Morin, S. A. et al., Camouflage and Display for Soft Machines. *Science* **337** (6096), 828
(2012).
- 76 Keplinger, C. et al., Harnessing snap-through instability in soft dielectrics to achieve giant
voltage-triggered deformation. *Soft Matter* **8** (2), 285 (2012).
- 77 Mosadegh, B. et al., Pneumatic Networks for Soft Robotics that Actuate Rapidly. *Adv. Funct.*
Mater. **24** (15), 2163 (2014).

- 78 Keplinger, C. et al., Stretchable, Transparent, Ionic Conductors. *Science* **341** (6149), 984
(2013).
- 79 Kwok, S. W. et al., Magnetic Assembly of Soft Robots with Hard Components. *Adv. Funct.*
Mater. **24** (15), 2180 (2014).
- 80 Cherenack, K. et al., Woven Electronic Fibers with Sensing and Display Functions for Smart
Textiles. *Adv. Mater.* **22** (45), 5178 (2010); Zysset, C. et al., Combining electronics on flexible
plastic strips with textiles. *Text. Res. J.* **83** (11), 1130 (2013).
- 81 Wolf, S. A. et al., Spintronics: A spin-based electronics vision for the future. *Science* **294**
(5546), 1488 (2001); Bedoya-Pinto, A. et al., Flexible spintronic devices on Kapton. *Appl.*
Phys. Lett. **104** (6), 5 (2014).
- 82 Bader, S. D. and Parkin, S. S. P., in *Annual Review of Condensed Matter Physics, Vol 1*
(Annual Reviews, Palo Alto, 2010), Vol. 1, pp. 71.
- 83 Blakemore, R., MAGNETOTACTIC BACTERIA. *Science* **190** (4212), 377 (1975).
- 84 Wiltschko, W. and Wiltschko, R., Magnetic orientation and magnetoreception in birds and
other animals. *J. Comp. Physiol. A -Neuroethol. Sens. Neural Behav. Physiol.* **191** (8), 675
(2005).
- 85 Monch, I. et al., Rolled-Up Magnetic Sensor: Nanomembrane Architecture for In-Flow
Detection of Magnetic Objects. *ACS Nano* **5** (9), 7436 (2011).
- 86 Lin, G. G. et al., A highly flexible and compact magnetoresistive analytic device. *Lab Chip* **14**
(20), 4050 (2014).
- 87 Pamme, N., Magnetism and microfluidics. *Lab Chip* **6** (1), 24 (2006).
- 88 Loureiro, J. et al., Toward a magnetoresistive chip cytometer: Integrated detection of magnetic
beads flowing at cm/s velocities in microfluidic channels. *Appl. Phys. Lett.* **95** (3), 3 (2009).
- 89 Liang, J. J. et al., Elastomeric polymer light-emitting devices and displays. *Nat. Photonics* **7**
(10), 817 (2013).
- 90 Lenz, J. and Edelstein, A. S., Magnetic sensors and their applications. *IEEE Sens. J.* **6** (3), 631
(2006).
- 91 Hall, E. H., On a New Action of the Magnet on Electric Currents. *Amer. J. Math.* **2** (3), 287
(1879).
- 92 Thomson, W., On the Electro-Dynamic Qualities of Metals: Effects of Magnetization on the
Electric Conductivity of Nickel and of Iron. *Proc. R. Soc. Lond.* **8**, 546 (1856).
- 93 Yuasa, S. et al., Giant room-temperature magnetoresistance in single-crystal Fe/MgO/Fe
magnetic tunnel junctions. *Nat. Mater.* **3** (12), 868 (2004).
- 94 Ripka, P., REVIEW OF FLUXGATE SENSORS. *Sens. Actuator A-Phys.* **33** (3), 129 (1992).
- 95 Parkin, S. S. P., GIANT MAGNETORESISTANCE IN MAGNETIC NANOSTRUCTURES.
Annu. Rev. Mater. Sci. **25**, 357 (1995).
- 96 Nagasaka, K., CPP-GMR technology for magnetic read heads of future high-density recording
systems. *J. Magn. Magn. Mater.* **321** (6), 508 (2009).
- 97 (Royal Swedish Academy of Sciences: [http://www.nobelprize.org/
nobel_prizes/physics/laureates/2007/advanced-physicsprize2007.pdf](http://www.nobelprize.org/nobel_prizes/physics/laureates/2007/advanced-physicsprize2007.pdf), 2007).
- 98 Baril, L., Gurney, B., Wilhoit, D., and Speriosu, V., Magnetostriction in spin valves. *J. Appl.*
Phys. **85** (8), 5139 (1999).
- 99 Duenas, T. et al., Micro-sensor coupling magnetostriction and magnetoresistive phenomena. *J.*
Magn. Magn. Mater. **242**, 1132 (2002).
- 100 Graudejus, O., Gorn, P., and Wagner, S., Controlling the Morphology of Gold Films on
Poly(dimethylsiloxane). *ACS Appl. Mater. Interfaces* **2** (7), 1927 (2010).
- 101 Cerda, E., Ravi-Chandar, K., and Mahadevan, L., Thin films - Wrinkling of an elastic sheet
under tension. *Nature* **419** (6907), 579 (2002).
- 102 Lacour, S. P. et al., Mechanisms of reversible stretchability of thin metal films on elastomeric
substrates. *Appl. Phys. Lett.* **88** (20), 3 (2006).
- 103 Parkin, S. S. P., Roche, K. P., and Suzuki, T., GIANT MAGNETORESISTANCE IN
ANTIFERROMAGNETIC CO/CU MULTILAYERS GROWN ON KAPTON. *Jpn. J. Appl.*
Phys. Part 2 - Lett. **31** (9A), L1246 (1992).
- 104 Parkin, S. S. P., Flexible giant magnetoresistance sensors. *Appl. Phys. Lett.* **69** (20), 3092
(1996).
- 105 Lohndorf, M. et al., Highly sensitive strain sensors based on magnetic tunneling junctions.
Appl. Phys. Lett. **81** (2), 313 (2002); Lohndorf, M. et al., Strain sensors based on
magnetostrictive GMR/TMR structures. *IEEE Trans. Magn.* **38** (5), 2826 (2002).

- 106 Uhrmann, T. et al., Magnetostrictive GMR sensor on flexible polyimide substrates. *J. Magn. Magn. Mater.* **307** (2), 209 (2006).
- 107 Ozkaya, B., Saranu, S. R., Mohanan, S., and Herr, U., Effects of uniaxial stress on the magnetic properties of thin films and GMR sensors prepared on polyimide substrates. *Phys. Status Solidi A-Appl. Mat.* **205** (8), 1876 (2008).
- 108 Aurongzeb, D., Self-assembly of fractal nanowires and stripe magnetic domain on stretchable substrate. *Appl. Phys. Lett.* **89** (12), 3 (2006).
- 109 Briones, J. et al., Large area patterned magnetic films by depositing cobalt layers on nano-wrinkled polydimethylsiloxane templates. *Appl. Phys. Lett.* **103** (7) (2013).
- 110 Baibich, M. N. et al., GIANT MAGNETORESISTANCE OF (001)FE/(001)CR MAGNETIC SUPERLATTICES. *Phys. Rev. Lett.* **61** (21), 2472 (1988); Binasch, G., Grunberg, P., Saurenbach, F., and Zinn, W., ENHANCED MAGNETORESISTANCE IN LAYERED MAGNETIC-STRUCTURES WITH ANTIFERROMAGNETIC INTERLAYER EXCHANGE. *Phys. Rev. B* **39** (7), 4828 (1989).
- 111 Johnson, M. T., Bloemen, P. J. H., denBroeder, F. J. A., and deVries, J. J., Magnetic anisotropy in metallic multilayers. *Rep. Prog. Phys.* **59** (11), 1409 (1996).
- 112 Grunberg, P. et al., LAYERED MAGNETIC-STRUCTURES - EVIDENCE FOR ANTIFERROMAGNETIC COUPLING OF FE LAYERS ACROSS CR INTERLAYERS. *Phys. Rev. Lett.* **57** (19), 2442 (1986).
- 113 Ruderman, M. A. and Kittel, C., INDIRECT EXCHANGE COUPLING OF NUCLEAR MAGNETIC MOMENTS BY CONDUCTION ELECTRONS. *Physical Review* **96** (1), 99 (1954); Kasuya, T., A THEORY OF METALLIC FERROMAGNETISM AND ANTIFERROMAGNETISM ON ZENERS MODEL. *Prog. Theor. Phys.* **16** (1), 45 (1956); Yosida, K., MAGNETIC PROPERTIES OF CU-MN ALLOYS. *Physical Review* **106** (5), 893 (1957).
- 114 Power, S. R. and Ferreira, M. S., Indirect Exchange and Ruderman–Kittel–Kasuya–Yosida (RKKY) Interactions in Magnetically-Doped Graphene. *Crystals* **3** (1), 49 (2013).
- 115 Wetzig, K. and Schneider, C. M., *Metal Based Thin Films for Electronics*, 2 ed. (Wiley-VCH, Weinheim, 2006).
- 116 Meiklejohn, W. H. and Bean, C. P., NEW MAGNETIC ANISOTROPY. *Physical Review* **102** (5), 1413 (1956).
- 117 Nogues, J. and Schuller, I. K., Exchange bias. *J. Magn. Magn. Mater.* **192** (2), 203 (1999).
- 118 Mauri, D., Siegmann, H. C., Bagus, P. S., and Kay, E., SIMPLE-MODEL FOR THIN FERROMAGNETIC-FILMS EXCHANGE COUPLED TO AN ANTIFERROMAGNETIC SUBSTRATE. *J. Appl. Phys.* **62** (7), 3047 (1987).
- 119 Malozemoff, A. P., RANDOM-FIELD MODEL OF EXCHANGE-ANISOTROPY AT ROUGH FERROMAGNETIC-ANTIFERROMAGNETIC INTERFACES. *Phys. Rev. B* **35** (7), 3679 (1987); Stiles, M. D. and McMichael, R. D., Temperature dependence of exchange bias in polycrystalline ferromagnet-antiferromagnet bilayers. *Phys. Rev. B* **60** (18), 12950 (1999); Nowak, U. et al., Domain state model for exchange bias. I. Theory. *Phys. Rev. B* **66** (1), 9 (2002); Suess, D. et al., Exchange bias of polycrystalline antiferromagnets with perfectly compensated interfaces. *Phys. Rev. B* **67** (5), 8 (2003); Nogues, J. et al., Exchange bias in nanostructures. *Phys. Rep.-Rev. Sec. Phys. Lett.* **422** (3), 65 (2005); O'Grady, K., Fernandez-Outon, L. E., and Vallejo-Fernandez, G., A new paradigm for exchange bias in polycrystalline thin films. *J. Magn. Magn. Mater.* **322** (8), 883 (2010).
- 120 Neel, L., MAGNETISME - SUR UN PROBLEME DE MAGNETOSTATIQUE RELATIF A DES COUCHES MINCES FERROMAGNETIQUES. *Comptes Rendus Hebdomadaires Des Seances De L Academie Des Sciences* **255** (14), 1545 (1962).
- 121 Mott, N. F., The Electrical Conductivity of Transition Metals *Proceedings of the Royal Society A* **153**, 683 (1936).
- 122 Pal, A. K., Chaudhuri, S., and Barua, A. K., ELECTRICAL-RESISTIVITY AND TEMPERATURE-COEFFICIENT OF RESISTIVITY OF COBALT FILMS. *J. Phys. D-Appl. Phys.* **9** (15), 2261 (1976); Hanaoka, Y., Hinode, K., Takeda, K., and Kodama, D., Increase in electrical resistivity of copper and aluminum fine lines. *Mater. Trans.* **43** (7), 1621 (2002).
- 123 Kubinski, D. J. and Holloway, H., Giant magnetoresistance in Co/Cu multilayers: Influence of Co thickness at the first antiferromagnetic maximum. *J. Appl. Phys.* **79** (9), 7395 (1996).
- 124 Dieny, B. et al., GIANT MAGNETORESISTANCE IN SOFT FERROMAGNETIC MULTILAYERS. *Phys. Rev. B* **43** (1), 1297 (1991).

- 125 Dante, R. C., Santamaria, D. A., and Gil, J. M., Crosslinking and Thermal Stability of
Thermosets Based on Novolak and Melamine. *J. Appl. Polym. Sci.* **114** (6), 4059 (2009).
- 126 Lewis, P. R. and Price, C., ELECTRON-MICROSCOPY OF SYM-SBS BLOCK
POLYMERS. *Polymer* **13** (1), 20 (1972).
- 127 Treloar, L. R. G., ELASTICITY AND RELATED PROPERTIES OF RUBBERS. *Rep. Prog.*
Phys. **36** (7), 755 (1973).
- 128 Debenedetti, P. G. and Stillinger, F. H., Supercooled liquids and the glass transition. *Nature*
410 (6825), 259 (2001).
- 129 Mooney, M., A theory of large elastic deformation. *J. Appl. Phys.* **11** (9), 582 (1940); Rivlin,
R. S. and Saunders, D. W., LARGE ELASTIC DEFORMATIONS OF ISOTROPIC
MATERIALS .7. EXPERIMENTS ON THE DEFORMATION OF RUBBER. *Philosophical*
Transactions of the Royal Society of London Series a-Mathematical and Physical Sciences
243 (865), 251 (1951).
- 130 Ogden, R. W., LARGE DEFORMATION ISOTROPIC ELASTICITY - CORRELATION OF
THEORY AND EXPERIMENT FOR INCOMPRESSIBLE RUBBERLIKE SOLIDS.
Proceedings of the Royal Society of London Series a-Mathematical and Physical Sciences **326**
(1567), 565 (1972).
- 131 Lakes, R., FOAM STRUCTURES WITH A NEGATIVE POISSONS RATIO. *Science* **235**
(4792), 1038 (1987).
- 132 Winter, H. H. and Chambon, F., ANALYSIS OF LINEAR VISCOELASTICITY OF A
CROSS-LINKING POLYMER AT THE GEL POINT. *J. Rheol.* **30** (2), 367 (1986).
- 133 Mullins, L., Effect of stretching on the properties of rubber. *J. Rubber Res.* **16**, 15 (1947).
- 134 Suo, Z., Ma, E. Y., Gleskova, H., and Wagner, S., Mechanics of rollable and foldable film-on-
foil electronics. *Appl. Phys. Lett.* **74** (8), 1177 (1999).
- 135 Chiu, S. L., Leu, J., and Ho, P. S., FRACTURE OF METAL-POLYMER LINE
STRUCTURES .1. SEMIFLEXIBLE POLYIMIDE. *J. Appl. Phys.* **76** (9), 5136 (1994).
- 136 Huang, H. B. and Spaepen, F., Tensile testing of free-standing Cu, Ag and Al thin films and
Ag/Cu multilayers. *Acta Mater.* **48** (12), 3261 (2000).
- 137 Taylor, A. A., Edlmayr, V., Cordill, M. J., and Dehm, G., The effect of film thickness
variations in periodic cracking: Analysis and experiments. *Surf. Coat. Technol.* **206** (7), 1830
(2011).
- 138 Douville, N. J., Li, Z. Y., Takayama, S., and Thouless, M. D., Fracture of metal coated
elastomers. *Soft Matter* **7** (14), 6493 (2011).
- 139 Cao, W. Z., Gorm, P., and Wagner, S., Modeling the electrical resistance of gold film
conductors on uniaxially stretched elastomeric substrates. *Appl. Phys. Lett.* **98** (21), 3 (2011).
- 140 Vandeparre, H. et al., Localization of Folds and Cracks in Thin Metal Films Coated on
Flexible Elastomer Foams. *Adv. Mater.* **25** (22), 3117 (2013).
- 141 Graz, I. M., Cotton, D. P. J., and Lacour, S. P., Extended cyclic uniaxial loading of stretchable
gold thin-films on elastomeric substrates. *Appl. Phys. Lett.* **94** (7), 3 (2009).
- 142 Li, T., Suo, Z. G., Lacour, S. P., and Wagner, S., Compliant thin film patterns of stiff
materials as platforms for stretchable electronics. *J. Mater. Res.* **20** (12), 3274 (2005).
- 143 Hsu, Y. Y. et al., The effect of pitch on deformation behavior and the stretching-induced
failure of a polymer-encapsulated stretchable circuit. *J. Micromech. Microeng.* **20** (7), 11
(2010).
- 144 Verplancke, R., Bossuyt, F., Cuypers, D., and Vanfleteren, J., Thin-film stretchable electronics
technology based on meandering interconnections: fabrication and mechanical performance. *J.*
Micromech. Microeng. **22** (1), 9 (2012).
- 145 Melzer, M., Kopylov, A., Makarov, D., and Schmidt, O. G., Stretchability and self-healing of
wrinkled GMR multilayers on elastomeric membranes. *SPIN* **3**, 6 (2013).
- 146 Cerda, E. and Mahadevan, L., Geometry and physics of wrinkling. *Phys. Rev. Lett.* **90** (7), 4
(2003).
- 147 Genzer, J. and Groenewold, J., Soft matter with hard skin: From skin wrinkles to templating
and material characterization. *Soft Matter* **2** (4), 310 (2006).
- 148 Huang, Z. Y., Hong, W., and Suo, Z., Nonlinear analyses of wrinkles in a film bonded to a
compliant substrate. *J. Mech. Phys. Solids* **53** (9), 2101 (2005).
- 149 Lacour, S. P., Jones, J., Suo, Z., and Wagner, S., Design and performance of thin metal film
interconnects for skin-like electronic circuits. *IEEE Electron Device Lett.* **25** (4), 179 (2004).
- 150 Lacour, S. P. et al., Stiff subcircuit islands of diamondlike carbon for stretchable electronics. *J.*
Appl. Phys. **100** (1), 6 (2006).

- 151 Carlson, A. et al., Transfer Printing Techniques for Materials Assembly and
152 Micro/Nanodevice Fabrication. *Adv. Mater.* **24** (39), 5284 (2012).
- 153 Kim, D. H. et al., Materials and noncoplanar mesh designs for integrated circuits with linear
154 elastic responses to extreme mechanical deformations. *Proc. Natl. Acad. Sci. U. S. A.* **105** (48),
155 18675 (2008).
- 156 Xu, S. et al., Soft Microfluidic Assemblies of Sensors, Circuits, and Radios for the Skin.
157 *Science* **344** (6179), 70 (2014).
- 158 Jung, I. et al., Paraboloid electronic eye cameras using deformable arrays of photodetectors in
159 hexagonal mesh layouts. *Appl. Phys. Lett.* **96** (2), 3 (2010).
- 160 Graz, I. M., Cotton, D. P. J., Robinson, A., and Lacour, S. P., Silicone substrate with in situ
161 strain relief for stretchable thin-film transistors. *Appl. Phys. Lett.* **98** (12), 3 (2011).
- 162 Lu, N. S., Yoon, J. I., and Suo, Z. G., Delamination of stiff islands patterned on stretchable
163 substrates. *Int. J. Mater. Res.* **98** (8), 717 (2007).
- 164 Zhu, S. et al., Ultrastretchable Fibers with Metallic Conductivity Using a Liquid Metal Alloy
165 Core. *Adv. Funct. Mater.* **23** (18), 2308 (2013).
- 166 Duffy, D. C., McDonald, J. C., Schueller, O. J. A., and Whitesides, G. M., Rapid prototyping
167 of microfluidic systems in poly(dimethylsiloxane). *Anal. Chem.* **70** (23), 4974 (1998).
- 168 Bender, M. et al., High resolution lithography with PDMS molds. *J. Vac. Sci. Technol. B* **22**
169 (6), 3229 (2004); Missinne, J. et al., Stretchable optical waveguides. *Opt. Express* **22** (4), 4168
170 (2014); Fuard, D. et al., Optimization of poly-di-methyl-siloxane (PDMS) substrates for
171 studying cellular adhesion and motility. *Microelectron. Eng.* **85** (5-6), 1289 (2008).
- 172 Roth, J., Doctoral, Technische Universität Dresden, 2008.
- 173 Lambrecht, J., Wolf, H. P., and Gerlach, E., in *Silikonelastomere für Kabelgarnituren,*
174 *Isolatoren und Überspannungsableiter – Profil einer Werkstofffamilie*, edited by J.
175 Kindersberger (VDE Publishing, Berlin, 2003), pp. 17.
- 176 Grigoras, S., in *Computational modeling of polymers*, edited by J. B. Bicerano (CRC Press,
177 New York, 1992), pp. 161.
- 178 Melzer, M. et al., Direct Transfer of Magnetic Sensor Devices to Elastomeric Supports for
179 Stretchable Electronics. *Adv. Mater.* (2014).
- 180 Egelhoff, W. F. and Steigerwald, D. A., THE ROLE OF ADSORBED GASES IN METAL
181 ON METAL EPITAXY. *J. Vac. Sci. Technol. A-Vac. Surf. Films* **7** (3), 2167 (1989).
- 182 Egelhoff, W. F. et al., Oxygen as a surfactant in the growth of giant magnetoresistance spin
183 valves. *J. Appl. Phys.* **82** (12), 6142 (1997).
- 184 Melzer, M. et al., Elastic magnetic sensor with isotropic sensitivity for in-flow detection of
185 magnetic objects. *RSC Adv.* **2** (6), 2284 (2012).
- 186 Melzer, M., Lin, G. G., Makarov, D., and Schmidt, O. G., Stretchable Spin Valves on
187 Elastomer Membranes by Predetermined Periodic Fracture and Random Wrinkling. *Adv.*
188 *Mater.* **24** (48), 6468 (2012).
- 189 Ali, M. et al., Antiferromagnetic layer thickness dependence of the IrMn/Co exchange-bias
190 system. *Phys. Rev. B* **68** (21), 7 (2003).
- 191 Parkin, S., Spin-polarized current in spin valves and magnetic tunnel junctions. *MRS Bull.* **31**
192 (5), 389 (2006).
- 193 Meitl, M. A. et al., Transfer printing by kinetic control of adhesion to an elastomeric stamp.
194 *Nat. Mater.* **5** (1), 33 (2006).
- 195 Chanda, D. et al., Large-area flexible 3D optical negative index metamaterial formed by
196 nanotransfer printing. *Nat. Nanotechnol.* **6** (7), 402 (2011).
- 197 Ahn, J. H. et al., Heterogeneous three-dimensional electronics by use of printed semiconductor
198 nanomaterials. *Science* **314** (5806), 1754 (2006); Kim, S. et al., Microstructured elastomeric
199 surfaces with reversible adhesion and examples of their use in deterministic assembly by
200 transfer printing. *Proc. Natl. Acad. Sci. U. S. A.* **107** (40), 17095 (2010).
- 201 Linder, V. et al., Water-soluble sacrificial layers for surface micromachining. *Small* **1** (7), 730
202 (2005).
- 203 Brochu, P. and Pei, Q. B., Advances in Dielectric Elastomers for Actuators and Artificial
204 Muscles. *Macromol. Rapid Commun.* **31** (1), 10 (2010).
- 205 Stoyanov, H. et al., Soft Conductive Elastomer Materials for Stretchable Electronics and
206 Voltage Controlled Artificial Muscles. *Adv. Mater.* **25** (4), 578 (2013).
- 207 Parkin, S. S. P., Li, Z. G., and Smith, D. J., GIANT MAGNETORESISTANCE IN
208 ANTIFERROMAGNETIC CO/CU MULTILAYERS. *Appl. Phys. Lett.* **58** (23), 2710 (1991).

- 177 Bowden, N., Huck, W. T. S., Paul, K. E., and Whitesides, G. M., The controlled formation of
ordered, sinusoidal structures by plasma oxidation of an elastomeric polymer. *Appl. Phys. Lett.*
178 **75** (17), 2557 (1999).
- 178 Cendula, P. et al., Directional Roll-up of Nanomembranes Mediated by Wrinkling. *Nano Lett.*
11 (1), 236 (2011).
- 179 Brau, F. et al., Multiple-length-scale elastic instability mimics parametric resonance of
nonlinear oscillators. *Nat. Phys.* **7** (1), 56 (2011).
- 180 Sanders, P. G., Eastman, J. A., and Weertman, J. R., Elastic and tensile behavior of
nanocrystalline copper and palladium. *Acta Mater.* **45** (10), 4019 (1997); Doi, H., Fujiwara,
181 Y., Miyake, K., and Ossawa, Y., A SYSTEMATIC INVESTIGATION OF ELASTIC
MODULI OF WC-CO ALLOYS. *Metallurgical Transactions* **1** (5), 1417 (1970).
- 181 Adrega, T. and Lacour, S. P., Stretchable gold conductors embedded in PDMS and patterned
by photolithography: fabrication and electromechanical characterization. *J. Micromech.*
Microeng. **20** (5), 8 (2010).
- 182 Karnaushenko, D. et al., Printable Giant Magnetoresistive Devices. *Adv. Mater.* **24** (33), 4518
(2012).
- 183 Makarov, D., Karnaushenko, D., and Schmidt, O. G., Printable Magnetoelectronics.
ChemPhysChem **14** (9), 1771 (2013).
- 184 Melzer, M. et al., Wearable Magnetic Field Sensors for Flexible Electronics. *Adv. Mater.*
(2014).
- 185 Bleuler, H. et al., NEW CONCEPTS FOR COST-EFFECTIVE MAGNETIC BEARING
CONTROL. *Automatica* **30** (5), 871 (1994).
- 186 Bahr, F. et al., presented at the The 13th International Symposium on Magnetic Bearings,
Arlington, VA (USA), 2012 (unpublished).
- 187 Rife, J. C. et al., Design and performance of GMR sensors for the detection of magnetic
microbeads in biosensors. *Sens. Actuator A-Phys.* **107** (3), 209 (2003).
- 188 Hall, D. A. et al., GMR biosensor arrays: A system perspective. *Biosens. Bioelectron.* **25** (9),
2051 (2010).
- 189 Weddemann, A. et al., How to design magneto-based total analysis systems for biomedical
applications. *Biosens. Bioelectron.* **26** (4), 1152 (2010).
- 190 Wang, S. X. and Li, G., Advances in giant magnetoresistance biosensors with magnetic
nanoparticle tags: Review and outlook. *IEEE Trans. Magn.* **44** (7), 1687 (2008).
- 191 Hutten, A. et al., New magnetic nanoparticles for biotechnology. *J. Biotechnol.* **112** (1-2), 47
(2004).
- 192 Fornara, A. et al., Tailored Magnetic Nanoparticles for Direct and Sensitive Detection of
Biomolecules in Biological Samples. *Nano Lett.* **8** (10), 3423 (2008).
- 193 Baselt, D. R. et al., A biosensor based on magnetoresistance technology. *Biosens. Bioelectron.*
13 (7-8), 731 (1998).
- 194 Salata, O. V., Applications of nanoparticles in biology and medicine. *J. Nanobiotechnol.* **2** (3),
6 (2004); Monch, I. et al., Ferromagnetic filled carbon nanotubes and nanoparticles: synthesis
and lipid-mediated delivery into human tumor cells. *J. Magn. Magn. Mater.* **290**, 276 (2005).
- 195 Pannetier, M. et al., Femtotesla magnetic field measurement with magnetoresistive sensors.
Science **304** (5677), 1648 (2004).
- 196 Shen, W. F., Liu, X. Y., Mazumdar, D., and Xiao, G., In situ detection of single micron-sized
magnetic beads using magnetic tunnel junction sensors. *Appl. Phys. Lett.* **86** (25), 3 (2005).
- 197 Jiang, Z., Llandro, J., Mitrelias, T., and Bland, J. A. C., An integrated microfluidic cell for
detection, manipulation, and sorting of single micron-sized magnetic beads. *J. Appl. Phys.* **99**
(8), 3 (2006).
- 198 Bremond, N., Santanach-Carreras, E., Chu, L. Y., and Bibette, J., Formation of liquid-core
capsules having a thin hydrogel membrane: liquid pearls. *Soft Matter* **6** (11), 2484 (2010);
Lorber, N., Pavageau, B., and Mignard, E., Droplet-Based Millifluidics as a New Miniaturized
Tool to Investigate Polymerization Reactions. *Macromolecules* **43** (13), 5524 (2010); Baraban,
199 L. et al., Millifluidic droplet analyser for microbiology. *Lab Chip* **11** (23), 4057 (2011).
- 200 Lin, G. G. et al., Magnetoresistive Emulsion Analyzer. *Sci Rep* **3** (2013).
- 200 Krutzik, P. O. and Nolan, G. P., Fluorescent cell barcoding in flow cytometry allows high-
throughput drug screening and signaling profiling. *Nat. Methods* **3** (5), 361 (2006); Kiermer,
V., FACS-on-a-chip. *Nat. Methods* **2** (2), 91 (2005).
- 201 Adams, J. D., Kim, U., and Soh, H. T., Multitarget magnetic activated cell sorter. *Proc. Natl.*
Acad. Sci. U. S. A. **105** (47), 18165 (2008).

- 202 Giepmans, B. N. G., Adams, S. R., Ellisman, M. H., and Tsien, R. Y., Review - The
fluorescent toolbox for assessing protein location and function. *Science* **312** (5771), 217
(2006).
- 203 Lin, G. G. et al., Magnetofluidic platform for multidimensional magnetic and optical
barcoding of droplets *Lab Chip* **15**, 216 (2015).
- 204 Albon, C. et al., Number sensitive detection and direct imaging of dipolar coupled magnetic
nanoparticles by tunnel magnetoresistive sensors. *Appl. Phys. Lett.* **95** (16), 3 (2009); Albon,
C. et al., Tunneling magnetoresistance sensors for high resolution particle detection. *Appl.*
Phys. Lett. **95** (2), 3 (2009); Hall, D. A. et al., GMR biosensor arrays: Correction techniques
for reproducibility and enhanced sensitivity. *Biosens. Bioelectron.* **25** (9), 2177 (2010).
- 205 Schmidt, O. G. and Eberl, K., Nanotechnology - Thin solid films roll up into nanotubes.
Nature **410** (6825), 168 (2001); Mei, Y. F. et al., Versatile Approach for Integrative and
Functionalized Tubes by Strain Engineering of Nanomembranes on Polymers. *Adv. Mater.* **20**
(21), 4085 (2008).
- 206 Harazim, S. M. et al., Lab-in-a-tube: on-chip integration of glass optofluidic ring resonators
for label-free sensing applications. *Lab Chip* **12** (15), 2649 (2012).
- 207 Sakai, T. et al., Anomalous pressure dependence of the giant magnetoresistance for Co/Cu
magnetic multilayers. *J. Phys. Soc. Jpn.* **67** (10), 3349 (1998).
- 208 Someya, T. et al., A large-area, flexible pressure sensor matrix with organic field-effect
transistors for artificial skin applications. *Proc. Natl. Acad. Sci. U. S. A.* **101** (27), 9966
(2004).
- 209 Efimenko, K. et al., Nested self-similar wrinkling patterns in skins. *Nat. Mater.* **4** (4), 293
(2005).
- 210 Labrune, M., Kools, J. C. S., and Thiaville, A., Magnetization rotation in spin-valve
multilayers. *J. Magn. Magn. Mater.* **171** (1-2), 1 (1997).
- 211 Heinrich, M. et al., Dimensional control of brittle nanoplatelets. A statistical analysis of a thin
film cracking approach. *Nano Lett.* **6** (9), 2026 (2006).
- 212 Thouless, M. D., Li, Z., Douville, N. J., and Takayama, S., Periodic cracking of films
supported on compliant substrates. *J. Mech. Phys. Solids* **59** (9), 1927 (2011).
- 213 Frank, S., Handge, U. A., Olliges, S., and Spolenak, R., The relationship between thin film
fragmentation and buckle formation: Synchrotron-based in situ studies and two-dimensional
stress analysis. *Acta Mater.* **57** (5), 1442 (2009).
- 214 Ying, M. et al., Silicon nanomembranes for fingertip electronics. *Nanotechnology* **23** (34)
(2012); Su, Y. W. et al., Mechanics of finger-tip electronics. *J. Appl. Phys.* **114** (16) (2013).
- 215 Fox, J. W. and Goulbourne, N. C., On the dynamic electromechanical loading of dielectric
elastomer membranes. *J. Mech. Phys. Solids* **56** (8), 2669 (2008).
- 216 Hu, J. M., Li, Z., Chen, L. Q., and Nan, C. W., High-density magnetoresistive random access
memory operating at ultralow voltage at room temperature. *Nat. Commun.* **2**, 8 (2011).
- 217 Allwood, D. A. et al., Magnetic domain-wall logic. *Science* **309** (5741), 1688 (2005).
- 218 Donolato, M. et al., Flexible and Stretchable Polymers with Embedded Magnetic
Nanostructures. *Adv. Mater.* **25** (4), 623 (2013); Meyer, J. et al., Giant magnetoresistance
effects in gel-like matrices. *Smart Mater. Struct.* **22** (2), 5 (2013).
- 219 Tseng, P. et al., Flexible and Stretchable Micromagnet Arrays for Tunable Biointerfacing.
Adv. Mater. (2015).
- 220 Monch, I. et al., Flexible Hall Sensorics for Flux Based Control of Magnetic Levitation. *IEEE*
Trans. Magn. (Submitted).
- 221 Yi, J. H. et al., presented at the 34th Conference on Decision and Control, New Orleans, 1995
(unpublished); Chen, X., Lie, K., and Xiao, K., presented at the 11th International Symposium
on Magnetic Bearings (ISMB), Nara, 2008 (unpublished).
- 222 Tsiotras, P. and Arcak, M., Low-bias control of AMB subject to voltage saturation: State-
feedback and observer designs. *IEEE Trans. Control Syst. Technol.* **13** (2), 262 (2005).
- 223 Ernst, D. et al., presented at the 37th International Spring Seminar on Electronics Technology,
Dresden, 2014 (unpublished).
- 224 Karnaushenko, D. et al., High-Performance Magnetic Sensorics for Printable and Flexible
Electronics. *Adv. Mater.* (2015).
- 225 Moench, I., Makarov, D., Melzer, M., and Schmidt, O. G., Germany (2012); Makarov, D. et
al., Germany (2012).

Selbständigkeitserklärung

Ich erkläre, dass ich die vorliegende Arbeit selbstständig und nur unter Verwendung der angegebenen Literatur und Hilfsmittel angefertigt habe. Ich erkläre, nicht bereits früher oder gleichzeitig bei anderen Hochschulen oder an dieser Universität ein Promotionsverfahren beantragt zu haben. Falls diese Erklärung nicht zutrifft, füge ich eine Stellungnahme diesem Antrag bei. Ich erkläre, obige Angaben wahrheitsgemäß gemacht zu haben und erkenne die Promotionsordnung der Fakultät für Naturwissenschaften der Technischen Universität Chemnitz vom 31. Januar 2011 an.

Datum der Einreichung

Unterschrift des Bewerbers

Acknowledgements

First, I would like to thank Prof. Dr. Oliver G. Schmidt for giving me the great chance to do my PhD on this intriguing topic and for the guidance and freedom to realize my own ideas and approaches to flexible and stretchable magnetoelectronics.

Secondly, my gratitude goes to Dr. Denys Makarov, who did a great job in supervising me during most of my PhD time and managed to lead the topic to a well-recognized story, even far beyond the institute. Thanks a lot for all the trust and friendship and for always finding the time to deal with big and small issues.

Also many thanks to Prof. Dr. Yongfeng Mei, who was very supportive by leading me through the first months of my PhD time, and to Rainer Kaltofen, who introduced me, as a newcomer in the field, very efficiently into the mysteries of magnetoelectronics and many details of magnetic thin film growths.

Of course the valuable contributions from many members of the MAGNA research group had a very positive impact on my research. Special thanks go to Daniil Karnaushenko, who strongly supported my work in so many aspects, in particular electronics and chemistry as well as artwork and photography together with his brother Dmitriy. I also want to acknowledge the support and optimization of GMR sensor preparation by Gungun Lin and the help of Dr. Larysa Baraban and Tobias Kosub on fluidics and more fundamental aspects, respectively.

On the technical side, I would like to thank Irina Fiering and Cornelia Krien for their reliable thin film depositions on demand and sometimes also on short notice. The work of Dr. Ingolf Mönch, Dr. Stefan Harazim, Dr. Daniel Grimm and Martin Bauer in terms of lithography and clean room maintenance is greatly acknowledged. I further want to thank Dr. Stefan Baunack and Barbara Eichler for their impressive ability to handle and get the best out of unconventional samples in their SEM/FIB and AFM setups, respectively. There was also much of support from Dr. Ralph Träger, Dr. Ralf Voigtlaender, Verena Schöps-Dörfel, Torsten Seidemann and Alexander Horst from the research technology department in design, assembly and control software development of the specific *in situ* stretching stage for the GMR characterization setup.

Special thanks go to Ulrike Steere, Anja Schanze and Sandra Hölzer for their administrative work as well as to Dr. Uwe Siegel, Dr. Carola Langer, Wilfried Pfeiffer, Dr. Stefanie Hartmann and Stefan Schwurack for their support in technology transfer and public relations aspects.

Many colleagues and collaborators from external institutions also gave valuable input and contributions to the work presented here. These are mainly: Falk Bahr, Daniel Ernst, Prof. Dr. Wilfried Hofmann, Prof. Dr. Thomas Zerna and Dr. Martin Oppermann (TU Dresden); Dr. Alfredo Calvimontes, Dr. Konrad Schneider and Holger Scheibner (IPF Dresden); Prof. Dr. Manfred Albrecht, Dr. Christian Schubert, Patrick Matthes and Colin Georgi (TU Chemnitz); Prof. Dr. Stefan Schulz, Dr. Olaf Ueberschär, Dr. Ramona Ecke and Kerstin Kreyßig (ENAS Chemnitz); Mathias Müller (HS Mittweida); Dr. Martin Kaltenbrunner and Dr. Ingrid Graz (JKU Linz), Prof. Dr. Takao Someya and Prof. Dr. Tsuyoshi Sekitani (Univ. Tokyo). Many thanks to all these people.

Last but not least I want to give my deep gratitude to my entire family, especially to my beloved wife Bianca and my lovely newborn son Finley, for so much patience during the last years and months and for making my days between the paperwork.

Curriculum Vitae

PERSONAL DETAILS

Name: Michael Melzer
Date of birth: May 08th 1983
Place of birth: Berlin, Germany

SCIENTIFIC EDUCATION

**Apr 2003 -
Sep 2006** Part-time scientific assistant at the Max-Planck-Institute for Colloids and Interfaces in Potsdam-Golm, supervised by Dr. Hans Riegler.

Topic: Fractal analysis of alkane-domain growth on the SiO₂/air interface

**Okt 2003 -
Sep 2009** Student of Physics at the University of Potsdam focusing on “Soft Matter Physics”.

**Oct 2006 -
Apr 2007** ERASMUS-Student at the Trinity College Dublin, Ireland, School of Physics.

**May 2008 -
Apr 2009** Diploma thesis at the chair of Applied Condensed Matter Physics headed by Prof. Dr. Reimund Gerhard, supervised by Dr. Guggi Kofod.

Thesis title: The influence of Strain on the Conductivity of Spray-Coated Compliant Electrodes

**Jan 2010 -
present** PhD student at IFW Dresden, Institute for Integrative Nanosciences headed by Prof. Oliver G. Schmidt, supervised by Dr. Denys Makarov.

Scientific publications, contributions, patents, grants & prizes

Scientific journal publications:

1. **M. Melzer**, D. Makarov, A. Calvimontes, D. Karnaushenko, S. Baunack, R. Kaltofen, Y.F. Mei, O.G. Schmidt: Stretchable Magnetoelectronics. *Nano Letters* **11**, 2522 (2011).
2. **M. Melzer**, D. Karnaushenko, D. Makarov, L. Baraban, A. Calvimontes, J.I. Mönch, R. Kaltofen, Y.F. Mei, O.G. Schmidt: Elastic magnetic sensor with isotropic sensitivity for in-flow detection of magnetic objects. *RSC Advances* **2**, 2284 (2012).
3. **M. Melzer**, G. Lin, D. Makarov and O.G. Schmidt: Stretchable spin valves on elastomer membranes by predetermined periodic fracture and random wrinkling. *Advanced Materials* **24**, 6468 (2012).
4. D.N. McCarthy, H. Stoyanov, D. Rychkov, H. Ragusch, **M. Melzer**, G. Kofod: Increased permittivity nanocomposite dielectrics by controlled interfacial interactions. *Composites Science and Technology* **72**, 731 (2012).
5. **M. Melzer**, A. Kopylov, D. Makarov, O.G. Schmidt: Stretchability and self-healing of wrinkled GMR multilayers on elastomeric membranes. *SPIN* **3**, 1340005 (2013).
6. R. Streubel, D. Makarov, J. Lee, C. Müller, **M. Melzer**, R. Schäfer, C.C. Bof Bufon, S.-K. Kim, O.G. Schmidt: Rolled-up permalloy nanomembranes with multiple windings. *SPIN* **3**, 1340001 (2013).
7. G. Lin, D. Makarov, **M. Melzer**, W. Si, C. Yan, O.G. Schmidt: A highly flexible and compact magnetoresistive analytic device. *Lab on a Chip* **14**, 4050 (2014).
8. **M. Melzer**, D. Karnaushenko, G. Lin, S. Baunack, D. Makarov, O.G. Schmidt: Direct Transfer of Magnetic Sensor Devices to Elastomeric Supports for Stretchable Electronics. *Advanced Materials* **27**, 1333 (2015).
9. **M. Melzer**, J.I. Mönch, D. Makarov, Y. Zabala, G.S. Cañón Bermúdez, D. Karnaushenko, S. Baunack, F. Bahr, C. Yan, M. Kaltenbrunner, O.G. Schmidt: Wearable magnetic field sensors for flexible electronics. *Advanced Materials* **27**, 1274 (2015).
10. **M. Melzer**, M. Kaltenbrunner, D. Makarov, D.D. Karnaushenko, D. Karnaushenko, T. Sekitani, T. Someya, O.G. Schmidt: Imperceptible Magnetoelectronics. *Nature Communications* **6**, 6080 (2015).
11. N. Pérez, **M. Melzer**, D. Makarov, O. Ueberschär, R. Ecke, S.E. Schulz, O.G. Schmidt: High-performance giant magnetoresistive sensorics on flexible Si membranes. *Applied Physics Letters* **106**, 153501 (2015).
12. D. Karnaushenko, B. Ibarlucea, S. Lee, G. Lin, L. Baraban, S. Pregl, M. Melzer, D. Makarov, W.M. Weber, T. Mikolajick, O.G. Schmidt, G. Cuniberti: Light Weight and Flexible High-Performance Diagnostic Platform. *Advanced Healthcare Materials* DOI: 10.1002/adhm.201500128 (2015).
13. J.I. Mönch, F. Bahr, **M. Melzer**, D. Karnaushenko, W. Hofmann, O.G. Schmidt: Flexible Hall Sensorics for Flux Based Control of Magnetic Levitation. *IEEE Transactions on Magnetics* (accepted).

Conference proceedings

1. M. Kolloosche, **M. Melzer**, A. Becker, H. Stoyanov, D.N. McCarthy, H. Ragusch, G. Kofod: The influence of mechanical properties in the electrical breakdown in poly-styrene-ethylene-butadiene-styrene thermoplastic elastomer. *Proceedings of the SPIE 7287, Electroactive Polymer Actuators and Devices (EAPAD)*, March 8th 2009, San Diego (CA), USA.
2. F. Bahr, **M. Melzer**, D. Karnaushenko, D. Makarov, D.D. Karnaushenko, J.I. Mönch, D. Malane, O.G. Schmidt, W. Hofmann: Flux Based Control of AMBs Using Integrated Ultra-Thin Flexible Bismuth Hall Sensors. *Proceedings of the 13th International Symposium on Magnetic Bearings (ISMB)*, August 6-9 2012, Arlington (VA), USA.
3. F. Bahr, **M. Melzer**, D. Karnaushenko, D. Makarov, G.S. Cañón Bermúdez, O.G. Schmidt, W. Hofmann: Erfassung der Luftspaltinduktion aktiver Magnetlager auf Basis ultradünner,

flexibler Hall-Sensoren, *Tagungsband des 9. Workshop für Magnetlagertechnik Zittau-Chemnitz*, September 2-3 2013, Chemnitz.

4. F. Bahr, **M. Melzer**, D. Karnaushenko, D. Makarov, G.S. Cañón Bermúdez, O.G. Schmidt, W. Hofmann: Permanent Magnet Bias AMB Using Integrated Hall Sensor Based Air Gap Flux Density Feedback. *Proceedings of the 1st Brazilian Workshop on Magnetic Bearings*, October 25-26 2013, Rio de Janeiro, Brazil.
5. D. Ernst, **M. Melzer**, D. Makarov, F. Bahr, W. Hofmann, O.G. Schmidt, T. Zerna: Packaging technologies for (Ultra-) thin sensor applications in active magnetic bearings. *Proceedings of the 37th International Spring Seminar on Electronics Technology (ISSE)*, May 7-11 2014, Dresden.

Invited talks

1. **M. Melzer**, O.G. Schmidt: Stretchable magnetoelectronics. *Seminar of the nanomembrane Group at Fudan University*, April 22nd 2011, Shanghai, China.
2. **M. Melzer**: Stretchable magnetoelectronics. 526. *Heraeus Seminar "Functional Magnetic Nanomembranes"*, March 4-6 2013, Bad Honnef.
3. **M. Melzer**: Stretchable magnetoelectronics. *Edgar Lüscher Seminar*, February 1-7 2014, Klosters, Switzerland.

Contributed conference talks

1. **M. Melzer**, R. Kaltofen, D. Makarov, Y.F. Mei, O.G. Schmidt: Towards stretchable magnetoelectronics. *75. Jahrestagung der DPG und DPG Frühjahrstagung*, March 13-18 2011, Dresden.
2. **M. Melzer**, R. Kaltofen, D. Makarov, Y.F. Mei, O.G. Schmidt: Towards stretchable magnetoelectronics. *INTERMAG 2011 - IEEE International Magnetism Conference*, April 25-29 2011, Taipei, Taiwan (ROC).
3. **M. Melzer**, D. Karnaushenko, G. Lin, D. Makarov, I.J. Mönch, O.G. Schmidt: Stretchable magnetoelectronics. *76. Jahrestagung der DPG und DPG Frühjahrstagung*, March 25-30 2012, Berlin.
4. **M. Melzer**, D. Karnaushenko, D. Makarov, I.J. Mönch, O.G. Schmidt: Stretchable magnetoelectronics. *2012 MRS Spring Meeting & Exhibit*, April 9-13 2012, San Francisco (CA), USA.
5. **M. Melzer**, D. Makarov, O.G. Schmidt: Stretchable magnetoelectronics for smart skin applications. *77. Jahrestagung der DPG und DPG Frühjahrstagung*, March 10-15 2013, Regensburg.
6. **M. Melzer**, D. Makarov, O.G. Schmidt: Stretchable magnetoelectronics for smart skin applications. *2013 MRS Spring Meeting & Exhibit*, April 1-5 2013, San Francisco (CA), USA.
7. **M. Melzer**, D. Makarov, D. Karnaushenko, I.J. Mönch, G. Lin, N. Perez Rodriguez, O.G. Schmidt: Shapeable Magnetic Sensorics. *59th Annual Magnetism and Magnetic Materials (MMM) Conference*, November 3-7 2014, Honolulu (HI), USA.
8. **M. Melzer**, M. Kaltenbrunner, D. Makarov, T. Sekitani, T. Someya, O.G. Schmidt: Ultra Light-Weight and Highly Stretchable Magnetoelectronics for Imperceptible on-Skin Sensorics. *59th Annual Magnetism and Magnetic Materials (MMM) Conference*, November 3-7 2014, Honolulu (HI), USA.
9. **M. Melzer**, M. Kaltenbrunner, D. Makarov, D. Karnaushenko, D. Karnaushenko, T. Sekitani, T. Someya, O.G. Schmidt: Imperceptible Magnetoelectronics. *581. Heraeus Seminar "Flexible, Stretchable and Printable High Performance Electronics"*, January 12-14 2015, Bad Honnef.
10. **M. Melzer**, M. Kaltenbrunner, D. Makarov, D. Karnaushenko, D. Karnaushenko, T. Sekitani, T. Someya, O.G. Schmidt: Imperceptible Magnetoelectronics. *2015 MRS Spring Meeting & Exhibit*, April 6-10 2015, San Francisco (CA), USA.

Technology pitches

1. **M. Melzer**, D. Makarov, D. Karnaushenko, N. Pérez, I.J. Mönch, F. Bahr, O.G. Schmidt: Ultradünne und flexible Magnetfeldsensoren. *HANNOVER MESSE 2014*, April 7-11 2014, Hannover.

2. **M. Melzer**, D. Makarov, D. Karnaushenko, Y. Zabala, I.J. Mönch, F. Bahr, W. Hofmann, O.G. Schmidt: Ultradünne und flexible Magnetfeldsensoren. *SENSOR + TEST 2014*, June 3-5 2014, Nuremberg.
3. **M. Melzer**, D. Makarov, I.J. Mönch, F. Bahr, W. Hofmann, O.G. Schmidt: Flexible and ultrathin magnetic field sensors for electrical machines and drives. *Innovation Days 2014*, December 1-2 2014, Munich.

Poster contributions

1. A. Kopylov, M. Pesic, **M. Melzer**, D. Karnaushenko, S. Baunack, D. Makarov, O.G. Schmidt: Stretchable magneto-sensorics. 526. *Heraeus Seminar "Functional Magnetic Nanomembranes"*, March 4-6 2013, Bad Honnef.
2. **M. Melzer**, D. Karnaushenko, G. Lin, D. Makarov, O.G. Schmidt: Stretchable Magnetoelectronics. *Erlangen Symposium on Flexible Electronics*, June 19-21 2013, Erlangen.
3. **M. Melzer**, D. Makarov, M. Kaltenbrunner, D.D. Karnaushenko, D. Karnaushenko, T. Sekitani, T. Someya, O.G. Schmidt: Imperceptible Magnetoelectronics. *INTERMAG Europe 2014 - IEEE International Magnetics Conference*, May 4-8 2014, Dresden.
4. D. Ernst, **M. Melzer**, D. Makarov, F. Bahr, W. Hofmann, O.G. Schmidt, T. Zerna: Realization of (Ultra-)Thin Sensors on Flexible Substrates. 581. *Heraeus Seminar "Flexible, Stretchable and Printable High Performance Electronics"*, January 12-14 2015, Bad Honnef.
5. **M. Melzer**, N. Pérez, D. Makarov, O.G. Schmidt: Strain effects in GMR sensors on bendable thin Si substrates. 581. *Heraeus Seminar "Flexible, Stretchable and Printable High Performance Electronics"*, January 12-14 2015, Bad Honnef.

Patent applications

1. D. Makarov, F. Bahr, T. Zerna, W. Hofmann, M. Oppermann, J.I. Mönch, **M. Melzer**, O.G. Schmidt: Verwendung von flexiblen magnetischen Dünnschichtsensorelementen. *DE 10 2011 087 342.2* (2011).
2. J.I. Mönch, D. Makarov, **M. Melzer**, O.G. Schmidt: Dünnschichtbauelement und Verfahren zu seiner Herstellung. *DE 10 2011 083 623.3* (2011).
3. **M. Melzer**, D. Karnaushenko, L. Baraban, D. Makarov, O.G. Schmidt: Verwendung eines elastischen magnetischen Sensorelementes, Verfahren seiner Herstellung und elastisches magnetisches Sensorelement. *DE 10 2011 088 140.9* (2011).

Prizes & grants

1. Dresdner Barkhausen-Poster-Preis 2010 für Studenten und Nachwuchswissenschaftler.
2. Artwork „Explore the Grand Wrinkle Canyon“ selected for Look Again in *MRS Bulletin* **39**, 920 (2014).
3. Inside front cover page at *Advanced Materials* **27**, 8 (2015).
4. DAAD Conference travel grant for the 2015 MRS Spring Meeting and Exhibit in San Francisco.

Explore the Grand Wrinkle Canyon

